

1997

Advanced eddy-current methods for quantitative NDE

Cheng-Chi Tai
Iowa State University

Follow this and additional works at: <https://lib.dr.iastate.edu/rtd>

 Part of the [Electrical and Electronics Commons](#), and the [Metallurgy Commons](#)

Recommended Citation

Tai, Cheng-Chi, "Advanced eddy-current methods for quantitative NDE " (1997). *Retrospective Theses and Dissertations*. 11749.
<https://lib.dr.iastate.edu/rtd/11749>

This Dissertation is brought to you for free and open access by the Iowa State University Capstones, Theses and Dissertations at Iowa State University Digital Repository. It has been accepted for inclusion in Retrospective Theses and Dissertations by an authorized administrator of Iowa State University Digital Repository. For more information, please contact digirep@iastate.edu.

INFORMATION TO USERS

This manuscript has been reproduced from the microfilm master. UMI films the text directly from the original or copy submitted. Thus, some thesis and dissertation copies are in typewriter face, while others may be from any type of computer printer.

The quality of this reproduction is dependent upon the quality of the copy submitted. Broken or indistinct print, colored or poor quality illustrations and photographs, print bleedthrough, substandard margins, and improper alignment can adversely affect reproduction.

In the unlikely event that the author did not send UMI a complete manuscript and there are missing pages, these will be noted. Also, if unauthorized copyright material had to be removed, a note will indicate the deletion.

Oversize materials (e.g., maps, drawings, charts) are reproduced by sectioning the original, beginning at the upper left-hand corner and continuing from left to right in equal sections with small overlaps. Each original is also photographed in one exposure and is included in reduced form at the back of the book.

Photographs included in the original manuscript have been reproduced xerographically in this copy. Higher quality 6" x 9" black and white photographic prints are available for any photographs or illustrations appearing in this copy for an additional charge. Contact UMI directly to order.

UMI

A Bell & Howell Information Company
300 North Zeeb Road, Ann Arbor MI 48106-1346 USA
313/761-4700 800/521-0600

Advanced eddy-current methods for quantitative NDE

by

Cheng-Chi Tai

A dissertation submitted to the graduate faculty
in partial fulfillment of the requirements for the degree of
DOCTOR OF PHILOSOPHY

Major: Electrical Engineering (Communications and Signal Processing)

Major Professor: Hsiu-Chi Han

Iowa State University

Ames, Iowa

1997

UMI Number: 9725462

UMI Microform 9725462
Copyright 1997, by UMI Company. All rights reserved.

**This microform edition is protected against unauthorized
copying under Title 17, United States Code.**

UMI
300 North Zeeb Road
Ann Arbor, MI 48103

Graduate College
Iowa State University

This is to certify that the doctoral dissertation of

Cheng-Chi Tai

has met the dissertation requirements of Iowa State University

Signature was redacted for privacy.

Major Professor

Signature was redacted for privacy.

For the Major Program

Signature was redacted for privacy.

For the Graduate College

TABLE OF CONTENTS

CHAPTER 1. GENERAL INTRODUCTION	1
1.1 Fundamental Eddy Current Concepts	2
1.2 Eddy Current Inspection Techniques	4
1.3 Forward Problem and Inverse Problem	7
1.4 Research Methods	9
1.5 Dissertation Organization	13
References	15
CHAPTER 2. THICKNESS AND CONDUCTIVITY OF METALLIC LAYERS FROM PULSED EDDY-CURRENT MEASUREMENTS	17
Abstract	17
I Introduction	18
II Theory	21
III Experiment	25
IV Inversion Method	30
V Results	33
VI Discussion	34
Acknowledgments	35
References	35
CHAPTER 3. EXTREME SENSITIVITY OF EDDY-CURRENTS TO THE SURFACE CONDITIONS OF NICKEL	52
I Introduction	52
II Experimental Set-up and Measurements	54
III Results	54
IV Fit to Model Calculations	56
V Implications for NDE and Conclusions	57
Acknowledgments	59
References	59
CHAPTER 4. CHARACTERIZATION OF COATINGS ON MAGNETIC METALS USING SWEEP-FREQUENCY EDDY CURRENT AND TRANSIENT EDDY CURRENT METHODS	66
I Introduction	66
II Theory	68
III Experiment	71
IV Results	73
V Summary	75
Acknowledgments	75

References	76
CHAPTER 5. PHOTOINDUCTIVE IMAGING FOR BOLT HOLE CORNER CRACK INSPECTION	90
Abstract	90
I Introduction	91
II The Photoinductive Effect	93
III Photoinductive Imaging System	98
IV Results and Discussion	99
V Summary and Conclusions	105
Acknowledgments	107
References	107
CHAPTER 6. GENERAL CONCLUSIONS	128
APPENDIX 1: SWEPT-FREQUENCY EDDY CURRENT SIGNAL AND PULSED EDDY CURRENT SIGNAL TRANSFORMATION	134
APPENDIX 2: CORRECTIONS FOR NON-IDEAL COIL BEHAVIOR	138
APPENDIX 3: SOFTWARE DESIGN AND IMPLEMENTATION	148
ACKNOWLEDGMENTS	155

CHAPTER 1.

GENERAL INTRODUCTION

The use of eddy currents for quantitative nondestructive evaluation (QNDE) has a long history. In the Center for Nondestructive Evaluation (CNDE) at Iowa State University, much effort has gone into the study of this subject. The work undertaken in this dissertation continues previous efforts of members of the eddy current group in CNDE and attempts to advance to new, uncharted areas. In this introduction, we first briefly introduce the fundamental concepts of eddy current techniques. Then we describe the main ideas on how we can apply these techniques to detect flaws in metals, to characterize magnetic metals, or to measure the thickness, conductivity, and permeability of coatings on metals. Finally, we describe the organization of this dissertation.

The ability to quantitatively determine the location and shape of any flaw or internal structure within materials is important for both process control and in-service inspection of parts. Eddy currents and electromagnetic test techniques offer low-cost methods for inspection of metallic materials. In such industries as nuclear, aerospace and marine, eddy current techniques have been used to find defects in metals for a long time. In high pressure, high temperature and high speed engineering systems, the ability to avoid premature failures can mean enormous savings in both cost and human life. To meet the demanding requirements for nondestructive evaluation, we must expend much effort to develop reliable, quick, and automatic NDE systems. In the following, we describe the work that has been completed or is being developed in the eddy current group and its relation to this dissertation. We start by introducing the basic idea of eddy currents.

1.1 Fundamental Eddy Current Concepts

The basic idea of eddy currents is to use a constant ac current source to excite a probe coil. The ac current in the coil produces an alternating magnetic field in accordance with the Maxwell-Ampere law. When the probe is placed in close proximity to metals, it induces within the test material a flow of electrical currents known as *eddy currents* ($\vec{J} = \sigma \vec{E}$) [Fig. 1.1]. These currents produce a magnetic field which in turn affects the original field. If the material is nonconducting and nonmagnetic ($\sigma = 0, \mu_r \leq 1$), no eddy currents are induced and eddy current NDE can not be applied to such materials. If the material is conducting and nonmagnetic ($\sigma > 0, \mu_r \leq 1$) (e.g., copper, zinc, aluminum, titanium or stainless steel), the induced eddy currents provide a magnetic field which opposes a change in the net magnetic flux density. The coil impedance is the coil voltage divided by the constant drive current. Since the fields are affected by the presence of the work-piece, coil impedance is also affected. If the material is conducting and ferromagnetic ($\sigma > 0, \mu_r > 1.001$) (e.g., nickel, iron, cobalt, steel or ferrites), the exciting coil reactance changes in a different way than for nonmagnetic test materials. The flux lines within the magnetic material find portions of their path in such material with far less reluctance than air. This means that the path of flux lines are shortened, and then the magnetic flux density in the coil is increased. The coil inductance and inductive reactance increase dramatically when a highly permeable magnetic material is tested. However, if the frequency of ac current is high enough (up to one megahertz), the influence of eddy currents becomes predominant. The net effect is to decrease the inductance with increasing frequency [Fig. 1.2].

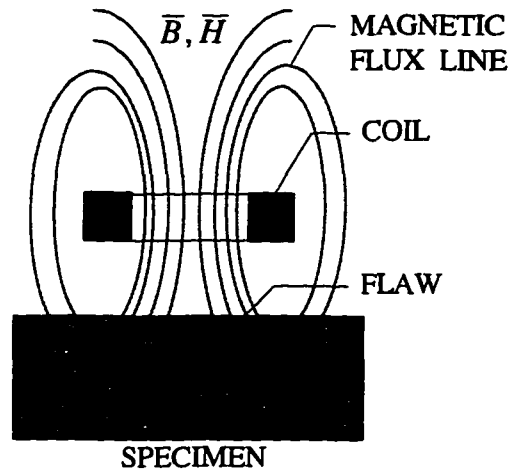


Figure 1.1 Magnetic field coupling of eddy current probe coil and metals under test.

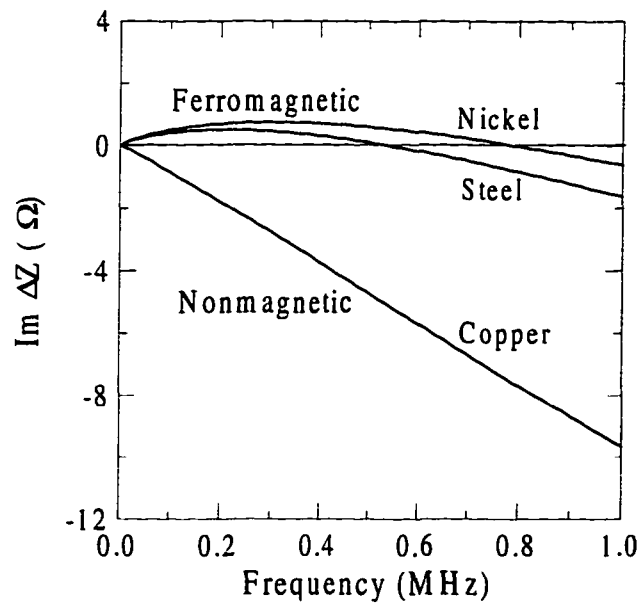


Figure 1.2 Impedance difference for a coil above metals and a coil in air. Eddy currents have a more complicated interaction with the ferromagnetic materials. The interaction depends on the frequency.

Eddy current NDE uses frequencies ranging from hundreds of hertz to megahertz ($10^2 - 10^7$). In this low frequency range, the phenomena are governed by the *quasi-static* form of Maxwell's equations where the displacement current term (\bar{D}') is assumed to be negligible. Consequently, the fields are governed by diffusion type equations rather than the wave equations of electromagnetic theory. In fact, an eddy current coil does not launch a wave. The fields decay exponentially inside metals. This decay is governed by a geometrical quantity called the *skin depth*, i.e.,

$$\delta = \frac{1}{\sqrt{\pi f \mu \sigma}}. \quad (1.1)$$

At one skin depth, the field intensity is $1/e$ (~37%) of its surface value. The skin effect phenomenon exists in all eddy current testing situations.

1.2 Eddy Current Inspection Techniques

Three advanced eddy current techniques have been under development in CNDE. They are swept-frequency eddy current, pulsed eddy currents and photoinductive eddy current imaging methods. Since the diffusion of eddy currents into metals is governed by the skin effect, the main idea of the swept-frequency eddy current (SFEC) method is to use a number of different frequencies to excite the coil. As shown in equation (1.1), the skin depth changes with frequency, conductivity and permeability of the materials under inspection. Hundreds of different frequencies in the eddy current frequency range are used to excite the coil. Lower

frequencies have larger skin depth. They penetrate more deeply into the metals. Higher frequencies have smaller skin depth. They reflect the near surface situation. Consequently, swept-frequency eddy current technique can be used to determine depth information in metals. Previous research in CNDE showed that this technique can be successfully used to determine the thickness and conductivity of metallic coatings. As mentioned in the previous section, since eddy currents interact with ferromagnetic materials in a way that depends on the frequency, using this technique to characterize magnetic metals is a promising application. One example is using swept-frequency eddy currents to determine the initial permeability (metal's permeability when the intensity of the applied field is weak) of ferromagnetic materials.

The pulsed eddy current (PEC) technique is a time-domain method that gives similar information as the swept-frequency eddy current method. A step-function voltage is used to excite the coil. When transferred to the frequency domain, the step-function voltage covers a broad spectrum. It contains low frequencies as well as high frequencies [Fig. 1.3]. The main disadvantage of the swept-frequency eddy current method is the relatively long measurement time. The implementation of a frequency-domain eddy current method requires measurements of the absolute impedance of the coil using a computer-controlled HP 4194A impedance analyzer. Each measurement takes approximately 5–10 minutes. The same measurement by pulsed eddy current method can be made much quicker. In principle, since we can finish one measurement by applying a step-function voltage (square wave with a 1 ms period), pulsed eddy current method can be thousands of times quicker than the swept-frequency eddy current method.

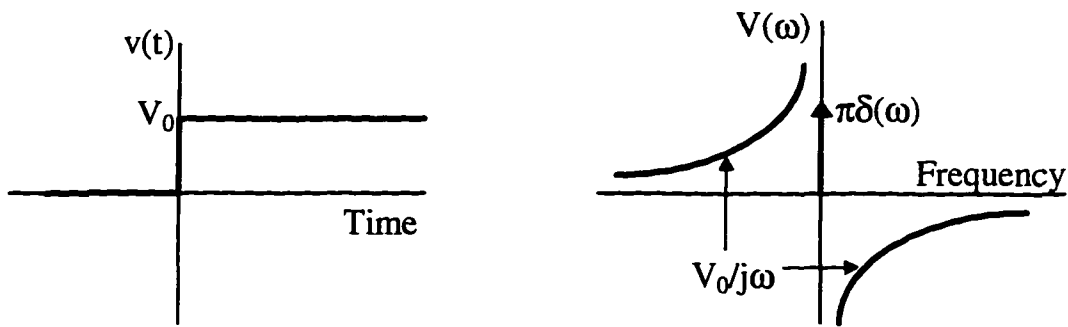


Figure 1.3 Step-function voltage and its frequency domain spectrum.

Photoinductive (PI) eddy current imaging is a newly devised technique that is similar to photothermal imaging but based on eddy current detection of thermal waves. Laser-induced thermal waves produce a localized modulation of electrical conductivity in the specimen, which can be detected through its effect on the impedance of a nearby eddy current coil. Moulder and others [1,2] showed that this new technique can be used to calibrate probes. This calibration method is electro-optical in character; calibration can be accomplished quickly and reliably under computer control. The method offers a means to determine the electric field intensity of eddy-current probes, a quantity that is directly related to their performance for flaw detection and characterization. As indicated in Auld's reciprocity relation [3,4], the impedance change is determined primarily by the values of \bar{E} and \bar{H} at the position of the laser spot. Therefore, the photoinductive technique permits mapping \bar{E} and \bar{H} with spatial resolution that is governed only by the size of the thermal spot (up to several microns), one of the chief advantages of the PI technique over other methods of mapping magnetic fields. This photoinductive phenomenon can also be used to image surface or near-surface cracks, voids, or inclusions [5,6]. Of particular interest is the detection of a

corner crack on the surface surrounding a bolt hole. We have developed new methods for characterizing the shape of corner crack using high-resolution photoinductive eddy current imaging technique.

1.3 Forward Problem and Inverse Problem

1.3.1 Forward Problem

The forward problem in eddy current NDE is the computation of the fields and coil impedance from the given geometry and physical characteristics of the coil, the work piece, the flaw, and the coating thickness or the internal structure. We use the analytical solution for the impedance of an air-core coil over a layered metal derived by Cheng [7] and by Dodd and Deeds [8]. The same authors [9] also have an analytical solution for the impedance of an air-core coil over a multilayered metal. Auld [3, 4] developed an exact reciprocity-based formula that can determine change in the impedance of an air-core probe for the generic problem shown schematically in Fig. 1.4. The main disadvantage of Auld's formula is that it requires the determination of the exact electric field in the region of the flaw. The electric field in the presence of a flaw depends on the shape and size of the flaw and does not have an exact analytical solution. To overcome this disadvantage, Rose *et al.* [10 – 12] used perturbation theory to approximate the solutions. Nakagawa *et al.* [5,6] developed a computer model that is capable of simulating eddy current NDE in generic inspection geometry. The model has been generalized to handle more general specimen geometry, including curved surfaces and corners. The inspection of chamfered bolt holes, rods, and heat exchanger tubing are currently under investigation as immediate applications.

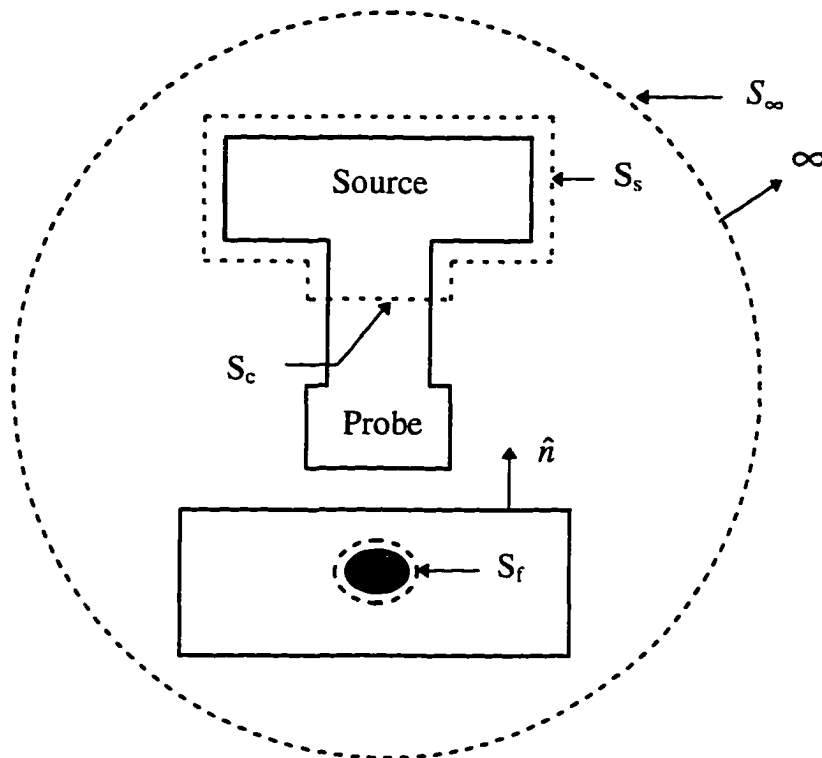


Figure 1.4 Schematic diagram of eddy-current apparatus showing various surfaces

1.3.2 Inverse Problem

The inverse problem is the geometric and physical characterization of the flaw, the coating thickness, or the internal structure from the given impedance data and the characteristics of the work piece and coil. One example of the inversion methods that were developed by previous workers [13] in CNDE is to determine the thickness and conductivity of metal coatings from swept-frequency eddy current signals. Their approach was based on the comparison of a measurement to the analytical solution for the impedance of an air-core coil over a layered metal derived by Cheng [7] and by Dodd and Deeds [8]. The least-square norm was their measure of closeness. This inversion procedure took approximately 20

minutes to perform on a DEC 5000 series workstation. Sethuraman and Rose [14] developed a rapid (requires several seconds on the same processor) solution that was based on the look-up table approach in which three characteristic features of the frequency domain response were identified then related to the thickness and conductivity of the metal coating under inspection. We developed a look-up table approach for determining the thickness and conductivity of surface layers from the features of the pulsed eddy current signal.

1.4 Research Methods

1.4.1 Measurement and Theoretical Modeling

We first consider work pieces modeled by the simplest geometrical shape: a half space or a single layer in air. For thick metals (much greater than the skin depth, for example, 1 cm thick), the half-space model is used. For thin and flat metals (thinner than 2 – 3 mm), a single layer model is used. The flaw signal can be masked by variables such as: lift-off, electrical conductivity and magnetic permeability, coil size, frequency, dimensions of the specimen, material property, and environmental conditions (temperature). Accurate interpretation of the signal requires the testing to be performed under controlled conditions. Simple models were used when we determined the effects of various factors. For example, we used a single layer model to represent a nickel foil (25 μm thick) when we measured the initial permeability of this metal. A zero lift-off probe was used when we wanted to isolate the effect of lift-off or to create a stronger signal.

The general problem of calculating the impedance of a circular coil with a rectangular cross-section above a multilayered, semi-infinite conductor has been solved analytically by

Cheng *et al.* [9] using a vector potential approach. This solution was used to calculate the coil impedance for a coil above two-layer metals as well as multilayer metals. In order to improve the computational efficiency, some alternative forms were derived by following the approach of Dodd and Deeds [8]. For example, we derived an extended, closed form solution for calculating the coil impedance, Z_L , for a coil above two-layer magnetic metals (Eq. 1.2 – Eq. 1.7). Dodd and Deeds' [8] widely-used solution is suitable for a coil next to a single-layered semi-infinite half-space of nonmagnetic metal, but not for magnetic metals. We derived a new formula including the magnetic permeabilities of the layer and substrate. This generated an extension of Dodd and Deeds' two-layer solution, or it can be viewed as a simplified form of Cheng, Dodd and Deeds' multilayer solution. We denoted the conductivity and permeability of the layer as σ_1 and μ_1 , and that of the substrate as σ_2 and μ_2 . The thickness of the layer is denoted by c . The base of the coil is at a height l_1 above the surface. The important parameters that pertain to the coil are the number of turns, N , the inner and outer radii, r_1 and r_2 , and the coil length, $l_2 - l_1$. The coil impedance Z_L for a coil above a single-layered semi-infinite half-space magnetic metal is

$$Z_L = K j\omega \int_0^\infty \frac{P^2(r_1, r_2)}{\alpha^5} \left\{ 2(l_2 - l_1) + \frac{1}{\alpha} \left[2e^{-\alpha(l_2 - l_1)} - 2 + A(\alpha)\phi(\alpha) \right] \right\} d\alpha, \quad (1.2)$$

where

$$K \equiv \frac{\pi \mu_0 N^2}{(l_2 - l_1)^2 (r_2 - r_1)^2}, \quad (1.3)$$

$$A(\alpha) \equiv \left(e^{-\alpha l_1} - e^{-\alpha l_2} \right)^2, \quad (1.4)$$

$$\phi(\alpha) \equiv \frac{(\alpha\mu_1 + \alpha_1\mu_0)(\alpha_1\mu_2 - \alpha_2\mu_1) + (\alpha\mu_1 - \alpha_1\mu_0)(\alpha_1\mu_2 + \alpha_2\mu_1)e^{2\alpha_1 c}}{(\alpha\mu_1 - \alpha_1\mu_0)(\alpha_1\mu_2 - \alpha_2\mu_1) + (\alpha\mu_1 + \alpha_1\mu_0)(\alpha_1\mu_2 + \alpha_2\mu_1)e^{2\alpha_1 c}}, \quad (1.5)$$

$$\alpha_i \equiv \sqrt{\alpha^2 + j\omega\mu_i\sigma_i}, \quad (1.6)$$

and

$$P(r_2, r_1) \equiv \int_{\alpha_{r_1}}^{\alpha_{r_2}} x J_1(x) dx. \quad (1.7)$$

In the above expressions, J_1 is a Bessel function of first kind and first order. The integration is over the spatial frequency α , which can be interpreted as the free-space wave-number. We will use this formula intensively in the research on magnetic metals characterization.

1.4.2 Difference in Signals

The impedance difference from swept-frequency eddy current measurements or the current change from pulsed eddy current measurements are the quantities used to evaluate coating thickness, hidden corrosion depth, or to characterize magnetic metals. As the coil is moved around parallel to the surface of the work-piece, the presence of a flaw is seen as a

change in impedance from the flaw-free material. The difference in signals between flawed and unflawed materials is used in characterizing the flaw. We measured the difference in impedance because the flaw signal is usually much smaller than the background signal. By using the signals' difference, we can eliminate the background signal and study the effects of the flaw directly.

1.4.3 Comparison of Experimental Results and Theoretical Predictions

All measured data will be compared to theoretical estimation. Our research showed that the uncertainty between measured data and theoretical prediction is usually within $\pm 5\%$. The good agreement provides a strong base for further study. Previous researchers developed inversion methods that were based on comparing the impedance analyzer measured results with Dodd and Deeds' theoretical prediction. We developed a rapid inversion method to determine the thickness and conductivity of metallic coatings based on the theoretical estimation of the features of the pulsed eddy-current signals. By comparison, we can also easily determine the limits of the theory. As indicated in Dodd and Deeds' paper [8], the most serious source of error in the calculation technique is the high-frequency effects. As the frequency increases, the current density will no longer be distributed uniformly over the cross section of the wire, but become concentrated near the surface. The resistance of the coil increases, and the inductance decreases. Using the swept-frequency eddy current method and comparing the measured results with a theoretical calculation, the high-frequency effects are obvious.

1.5 Dissertation Organization

This dissertation is divided into six chapters. The first chapter is this general introduction. Chapters II to V are papers which have been or will be submitted to various journals for publication. In all the papers, except Chapter III, I am the first author. My contributions to the paper in Chapter III included sample preparation, data collection, data analysis, preparation of figures, and contributions to technical discussions. Some other papers [15,16] that are not included in this dissertation are listed in the references. I have made major contributions to these papers. They are good supplements to this dissertation.

In Chapter II we used the pulsed eddy current technique to determine the thickness and conductivity of metallic coatings. A feature-based rapid inversion method was developed and used to infer the thickness and conductivity of the layers. My other contributions that are not included in this study involved developing analytical calculations using solutions of Cheng et al. [9]. Based on pulsed eddy current technology, we have developed a scanned pulsed eddy current instrument that has been licensed to industry for commercial development. This is one of the first instruments developed at the Center for NDE that has been commercially licensed. I participated in the team work throughout the entire development. I helped to develop the theoretical calculations, which agree with practical measurements, and proved that the system can function well. It has been shown that the system can be used to characterize coatings on metal surfaces, as well as hidden corrosion inside layered metals.

In Chapter III we studied the fundamentals of eddy current interactions with magnetic metals using a swept-frequency eddy current method. Before I came to work in the Center for NDE, the swept-frequency eddy-current method had been developed by Moulder and

Rose[13] to characterize coatings on metals. The main problem they faced is that the calculated eddy current signal could only be used to quantitatively characterize non-magnetic metals rather than the magnetic metals. After working on the pulsed eddy current system, I tried using this system to measure some magnetic metals such as nickel, iron, and steels. Surprisingly, I got excellent agreement between theoretical calculations and practical measurements. Working out why this was so has led us to a new understanding of the behavior of how eddy currents interact with magnetic metals. In this study, we found that the eddy current response of well-annealed, demagnetized, commercially-pure nickel is dominated by a thin region at the sample's surface that has a very significantly reduced permeability — i.e., a surface dead-layer. This dead layer may be due to the presence of surface damage (mechanical or chemical). We calculated the impedance of the coil based on the hypothesized single layer structure and found excellent quantitative agreement between the model and experiment. These results may have important consequences for many aspects of the interaction of low frequency electromagnetic fields with magnetically soft metals. As one example, the model predicts that sub-micrometer thick magnetic coatings on nonmagnetic metals could be measured using eddy current techniques. We feel that this study will lead eventually to a solution for the problem of characterizing case-hardened metals.

In Chapter IV, we developed a measurement technique using either swept-frequency eddy current or pulsed eddy current methods for determining the thickness, conductivity, and permeability of metallic coatings on metal substrates for the case when either coating, metal, or both are ferromagnetic. We demonstrated this technique for copper layers over nickel substrates, nickel layers over copper substrates, and zinc layers over steel substrates. The

latter measurements imply that the new method can be used to characterize the galvanization of steel, an important technological process.

In Chapter V, we applied the newly developed photoinductive imaging technique to characterize corner cracks on the surface surrounding a bolt hole. This high-resolution eddy current imaging method is governed mainly by the size of the thermal spot. We demonstrated that this method can be used to characterize the shape, the depth, and the length of corner cracks. Finally, these studies are summarized in Chapter VI.

References

- [1] J. C. Moulder and N. Nakagawa, "Characterizing the Performance of Eddy Current Probes Using Photoinductive Field-Mapping", in *Res. Nondestr. Eval*, 4:221–236, Springer-Verlag New York Inc. (1992).
- [2] N. Nakagawa and J. C. Moulder, "Eddy Current Probe Calibration via the Photoinductive Effect", in *Review of Progress in Quantitative NDE*, Vol. 13A, edited by D. O. Thompson and D. E. Chimenti, p. 295, Plenum, New York (1994).
- [3] B. A. Auld, "Eddy-Current Characterization of Materials and Structures", ASTM STP 722, edited by G. Birnbaum and G. Free, P. 332, American Society for Testing and Materials, Philadelphia (1981).
- [4] B. A. Auld, S. R. Jefferies, and J. C. Moulder. "Eddy-Current Signal Analysis and Inversion for Semielliptical Surface Cracks", *J. Nondestr. Eval*. 7:79 (1988).
- [5] N. Nakagawa, S. Mitra and J. C. Moulder, "Eddy Current Corner Crack Inspection", in *Review of Progress in Quantitative NDE*, Vol. 11A, edited by D. O. Thompson and D. E. Chimenti, p. 233, Plenum, New York (1992).
- [6] N. Nakagawa and J. C. Moulder, "A Model of Bolt Hole Inspection via Eddy Current", in *Review of Progress in Quantitative NDE*, Vol. 12A, edited by D. O. Thompson and D. E. Chimenti, p. 259, Plenum, New York (1993).
- [7] David H. S. Cheng, "The Reflected Impedance of a Circular Coil in the Proximity of a Semi-Infinite Medium", *IEEE Trans. Instrumentation and Meas.* IM-14, p. 107 (1965).

- [8] C.V. Dodd and W. E. Deeds, "Analytical Solutions to Eddy-Current Probe-Coil Problems", *J. Appl. Phys.* 39, p. 2829 (1968).
- [9] C. C. Cheng, C. V. Dodd, and W. E. Deeds, "General Analysis of Probe Coils Near Stratified Conductors", *Int. J. Nondestr. Test.* 3, 109 (1971).
- [10] S. M. Nair and J. H. Rose, "Reconstruction of Three-Dimensional Conductivity Variations from Eddy Current (Electromagnetic Induction) Data", *Inverse Problems* 6, p. 1007 (1990).
- [11] S. M. Nair and J. H. Rose "Low Frequency Asymptotics For Eddy Currents in a Conductivity Halfspace in the Absence and Presence of Inhomogeneties", *J. Appl. Phys.* 70 (1991).
- [12] R. Satveli, J. C. Moulder, B. Wang and J. H. Rose, "Impedance of a Coil Near an Imperfectly Layered Metal Structure: The Layer Approximation", *J. Appl. Phys.* 79(5), p. 1 (1996).
- [13] J. C. Moulder, E. Uzal, and J. H. Rose, "Thickness and Conductivity of Metallic Layers from Eddy Current Measurements", *Rev. Sci. Instrum.* 63, p. 3455 (1992).
- [14] A. Sethuraman, J. H. Rose, "Rapid Inversion of Eddy Current Data for Conductivity and Thickness of Metal Coatings", *J. Nondestr. Eval.* 14, p. 39 (1995).
- [15] J. H. Rose, C.-C. Tai and J. C. Moulder, "Scaling Relation for the Inductance of a Coil on a Ferromagnetic Half-Space", will be submitted to *J. Appl. Phys.* (1997).
- [16] J. C. Moulder, C.-C. Tai, B. Larson, and J. H. Rose, "Inductance of a Coil on a Thick Ferromagnetic Metal Plate", will be submitted to *IEEE Trans. on Magnetics* (1997).

CHAPTER 2.

THICKNESS AND CONDUCTIVITY OF METALLIC LAYERS FROM PULSED
EDDY-CURRENT MEASUREMENTS

A manuscript submitted to the *Review of Scientific Instruments*
© 1996 American Institute of Physics.

Cheng-Chi Tai, James H. Rose, and John C. Moulder

Center for Nondestructive Evaluation

Abstract

We describe a time-domain (pulsed) eddy-current technique for determining the thickness and conductivity of conductive coatings on metal plates. The pulsed eddy-current instrument records the transient current induced in an absolute, air-cored coil placed next to a layered sample and excited with a step-function change in voltage. Signals are digitized with 16-bit resolution at a sampling rate of 1 megasamples per second, and the excitation is repeated at a rate of 1 kHz. The instrument displays the difference in the transient current measured on the substrate and on the substrate plus coating. We measured pulsed eddy-current signals for a series of metal foils of varying thickness placed over 1-*cm* thick metal plates. Seven combinations of foil and substrate metals were studied: including pure aluminum, copper, and titanium foils over substrates of aluminum, titanium alloy, and

stainless steel. We report results for three types of samples: aluminum foils on Ti-6Al-4V substrate, titanium foils on 7075 aluminum alloys, and aluminum foils on AISI 304 stainless steel. Foil thickness ranged from 0.04–1.0 mm. We found that three features of the signal—the peak height, the time of occurrence of the first peak, and a characteristic zero-crossing time—depend sensitively upon the thickness of the layers and the relative electrical conductivity of coating and substrate. Theoretical calculations were compared to the measurements. Absolute agreement between calculated and measured signals was, in most cases, within 3%. No calibration with respect to artifact standards was used. Finally, a feature-based rapid inversion method was developed and used to infer the thickness and conductivity of the layers. The accuracy of the inversion depends upon the thickness of the layer and the contrast in conductivity between layer and substrate. For the materials studied the thickness could be determined within 13%, while the error in determining conductivity was 20%–30%. The time-domain method is much simpler and hundreds of times faster than the frequency-domain method previously reported by Moulder *et al.* [Rev. Sci. Instrum. **63**, 3455 (1992)]. © 1996 American Institute of Physics. [S0034-6748(96)0371-2]

I. Introduction

Coatings and surface treatments find a wide range of technological application; they can provide wear resistance, oxidation and corrosion protection, electrical contact or isolation and thermal insulation. Consequently, the ability to determine the thickness of metal coatings is important for both process control and in-service inspection of parts. Presently ultrasonic, thermal, and eddy-current inspection methods are used, depending on the circumstances. A

number of commercial instruments for determining the thickness of nonconducting coatings on metal substrates are based on the fact that the impedance change of the coil decreases exponentially with the distance of the coil from the metal (the lift-off effect). However, these instruments are not suitable for determining the thickness of metal layers on conductive substrates.

Recently Moulder, Uzal, and Rose ¹ developed a swept-frequency eddy-current technique for determining the thickness and conductivity of a conductive layer over a metal substrate of known conductivity. Their approach was based on an absolute comparison of measurement to an exact solution for the impedance of an air-cored coil over a layered metal by Cheng ² and by Dodd and Deeds ³. No calibration specimens were either required or used. The approach of Moulder *et al.* provided good estimates for both the thickness and conductivity. However, their implementation of the method required absolute measurements of the coil's impedance using a computer-controlled HP 4194A impedance analyzer, and each measurement took approximately 150 s.

Previous authors have reported time-domain approaches to the determination of coating thickness. Waidelich ⁴⁻⁶ measured the thickness of metal coatings using a pulsed eddy-current technique. He used a thyratron to pulse the magnetic probe and a balancing circuit to eliminate the echo from the air-metal boundary so that the echo from the metal-to-metal interface could be detected. Sather ⁷ described a pulsed eddy-current system to measure the wall thickness of thin-wall tubing. He investigated the relationship between pulse length and the depth of electromagnetic plane-wave penetration. Waidelich ⁸ described the use of longer pulses to penetrate thick steel sheets. The methods of Waidelich and Sather are empirical and

rely upon knowing the conductivity of the coating and substrate and using calibration specimens for quantitative measurements.

In this article we describe a new approach to pulsed eddy-current methods for determining the conductivity and thickness of conductive coatings that, while retaining the positive features of the frequency-domain approach of Moulder *et al.*, is significantly faster and uses less expensive equipment. Our approach is based on a new pulsed eddy-current (PEC) instrument, which was recently developed in our laboratories.⁹ It measures the transient voltage-current response function for step-function excitation of a coil. This personal-computer-based instrument is capable of rapid, linear quantitative measurements as evidenced by the excellent agreement between theory and experiment that will be shown in this article.

The step-function voltage excitation implies a spectrum that is inversely proportional to the frequency and thus strongly emphasizes the low-frequency components of the signal. One consequence is that the PEC instrument can support better discrimination at low frequencies than frequency-domain instrumentation in some practical conditions. This fact is one of the original motives for the development of the PEC system.

The organization of this paper is as follows. In Sec. II, we review and develop the theory needed to describe the voltage-current response function for the PEC instrument. In Sec. III, we describe the experimental setup and measurements. A method for determining the thickness and conductivity based on a look-up table is described in Sec. IV. Results are described and theory and experiment are compared in Sec. V. Finally, the article is concluded with a discussion of the results.

II. Theory

Consider an air-cored coil of wire placed next to a metal half-space coated with a metal layer and excited by a step function voltage. The current in the coil is computed minus the current when the coil is excited next to a reference half-space of the base metal. The hypothetical measurement is shown schematically in Fig. 1(a), while the dimensions of the circular coil, which has a rectangular cross section, are shown in Fig. 1(b). The base of the coil is at a height l_1 above the surface. The coil parameters of importance are number of turns N , inner and outer radii r_1 and r_2 , and coil length $l_2 - l_1$. The conductivity of the layer is denoted by σ_1 and that of the substrate is denoted by σ_2 . Only nonmagnetic materials are considered, hence we use the permeability of free space μ_0 . The thickness of the layer is denoted by c .

The calculation is sensitive to the thickness and conductivity of the metal layer. We use this sensitivity to determine these parameters from the measurements. The calculation is also sensitive to the lift-off (the distance from the bottom of the coil to the metal surface) and it is supposed that the lift-off is carefully controlled in the measurements.

The calculation proceeds roughly as follows. We start in the frequency domain. First, we calculate Z_L , the impedance of a right- cylindrical, air-cored eddy-current coil placed next a layered half-space. We also calculate Z_{HSP} , the impedance of the coil placed next to a layer-free reference half-space. We obtain the admittance difference ΔY by subtracting the inverse of Z_{HSP} from the inverse of Z_L . The current difference in the frequency domain, $\Delta I(\omega)$, is obtained by multiplying ΔY by the input voltage $V(\omega)$. Next, we take the inverse Fourier

transform of $\Delta I(\omega)$ to get the transient current response. The result, $\Delta i(t)$, can then be compared with measurements.

The calculation of the impedance of a right-cylindrical, air-cored eddy-current coil placed over a layered half-space was reviewed in Ref. 1. The impedance of the coil over a layered half-space is

$$Z_L = K j\omega \int_0^\infty \frac{P^2(r_1, r_2)}{\alpha^5} \left\{ 2(l_2 - l_1) + \frac{1}{\alpha} \left[2e^{-\alpha(l_2 - l_1)} - 2 + A(\alpha)\phi(\alpha) \right] \right\} d\alpha, \quad (1)$$

where

$$K \equiv \frac{\pi\mu_0 N^2}{(l_2 - l_1)^2 (r_2 - r_1)^2}, \quad (2)$$

$$P(r_1, r_2) \equiv \int_{\alpha r_1}^{\alpha r_2} x J_1(x) dx, \quad (3)$$

$$A(\alpha) \equiv \left(e^{-\alpha l_1} - e^{-\alpha l_2} \right)^2, \quad (4)$$

$$\phi(\alpha) \equiv \left[\frac{(\alpha + \alpha_1)(\alpha_1 - \alpha_2) + (\alpha - \alpha_1)(\alpha_1 + \alpha_2)e^{2\alpha_1 c}}{(\alpha - \alpha_1)(\alpha_1 + \alpha_2) + (\alpha + \alpha_1)(\alpha_1 + \alpha_2)e^{2\alpha_1 c}} \right], \quad (5)$$

$$\alpha_{1,2} = \sqrt{\alpha^2 + j\omega\mu_0\sigma_{1,2}}. \quad (6)$$

The impedance of the coil over the layer-free reference half-space is given by

$$Z_{HSP} = Kj\omega \int_0^{\infty} \frac{P^2(r_1, r_2)}{\alpha^5} \left\{ 2(l_2 - l_1) + \frac{1}{\alpha} \left[2e^{-\alpha(l_2 - l_1)} - 2 + A(\alpha) \frac{\alpha - \alpha_2}{\alpha + \alpha_2} \right] \right\} d\alpha. \quad (7)$$

Here, the integration is over the spatial frequency α , which can be interpreted as the free-space wave number. The transient current, $\Delta i(t)$, due to a step-function applied voltage is obtained from the inverse Fourier transform of $\Delta I(\omega)$

$$\Delta i(t) = IFT(\Delta I(\omega)), \quad (8)$$

where

$$\Delta I(\omega) = \Delta Y(\omega) \cdot V(\omega). \quad (9)$$

Here, $\Delta Y = 1/Z_L - 1/Z_{HSP}$ is the admittance difference. Furthermore, $V(\omega)$ is the Fourier transform of the step-function applied voltage $v(t)$, which is defined by

$$v(t) = \begin{cases} 1 & t > 0 \\ 0 & t < 0 \end{cases}. \quad (10)$$

After some simple algebra, we find

$$\Delta I(\omega) = \left(\frac{1}{Z_L(\omega)} - \frac{1}{Z_{HSP}(\omega)} \right) \cdot \left(\pi \delta(\omega) + P \left(\frac{1}{i\omega} \right) \right), \quad (11)$$

here P denotes the principal value.

The transient response is found by taking the inverse Fourier transform of $\Delta I(\omega)$. One obtains

$$\Delta i(t) = \frac{1}{2\pi} \int_{-\infty}^{\infty} \frac{\Delta Y(\omega)}{i\omega} \exp(i\omega t) d\omega. \quad (12)$$

We note that the delta-function term in Eq. (11) does not contribute to the inverse Fourier transform since both Z_L and Z_{HSP} tend to the same constant value as the frequency approaches zero. We can further simplify the above formula so that

$$\Delta i(t) = \frac{1}{\pi} \int_0^{\infty} \frac{\operatorname{Re}(\Delta Y(\omega)) \sin(\omega t) + \operatorname{Im}(\Delta Y(\omega)) \cos(\omega t)}{\omega} d\omega, \quad (13)$$

since $\Delta Y(t)$ is real.

III. Experiment

The measurement method and instrumentation are described in this section. We also show some typical experimental results and compare them with theory. Next, possible sources of error and their effect are mentioned. Finally, we describe the physics that leads to the key features of the experimental signals.

The experimental instrumentation used to obtain transient eddy-current signals is shown in Fig. 2. It consists of a custom electronic printed circuit board which provides for excitation of the coil with a square wave and detection circuits to obtain a signal representing the current through the coil. The amplified current signal is digitized with a 16-bit, 1 MHz analog to digital converter. Both the custom electronics and the commercial A/D card are installed in a 486-type portable personal computer. The computer controls the data acquisition and display through a WindowsTM based program. Excitation for the coil was provided by a 5 V TTL circuit producing a 1 kHz square wave synchronized to a clock on the A/D converter. We recorded the transient current in the coil during the first half-cycle of the square wave, and received a record of 500 points. The software permits averaging of repetitive signals, and we usually averaged 100 signals in the data shown here. Measurements were made by first recording a reference signal on the substrate alone and then subtracting this signal from subsequent signals. Thus, the signal displayed by the instrument represents the change in current $\Delta i(t)$ in the coil between reference and measurement conditions.

The coil we used for most of the measurements is a specially wound air-cored coil, whose physical dimensions are given in Table I and illustrated schematically in Fig. 1(b). It consists of 638 turns of AWG 40 wire in a right circular cylinder of rectangular cross-section.

The coil is mounted in a Delrin™ probe housing, which was clamped in a special probe fixture that permitted us to place the probe in contact with the surface of the specimen in a reproducible fashion, assuring a nearly constant lift-off, l_1 .

Measurements were taken for a variety of samples, including layers of pure aluminum, copper and titanium over 7075 aluminum, 304 stainless steel, and Ti-6Al-4V substrates. Moulder *et al.*¹ have shown that, since eddy-currents flow parallel to the surface, there are no detectable effects owing to the lack of bonding between the two materials. Measurements of $\Delta Z(\omega)$ (or $\Delta i(t)$ in this case) for bonded and unbonded specimens revealed no significant difference. A total of seven combinations of foil and substrate metals were studied. Ten samples of pure (99.999%) aluminum layered on a titanium alloy were prepared by stacking 0.1 mm foils of aluminum to different thicknesses ranging from 0.1–1 mm. Copper foils of thicknesses ranging from 0.05 to 0.5 mm were prepared in a similar fashion using copper 101. Five titanium foils were used to obtain thicknesses ranging from 0.041 to 0.205 mm. For most of the measurements we report here, the foils were placed in contact with a given substrate and the probe then placed upon the foil. A spring-loaded probe fixture ensured the foils and substrate were in good contact. Table II contains the electrical conductivity of layers and substrates we used. Thickness of the specimens we used are reported later in Table III.

Selected measurements are compared with theory in Fig. 3. Figure 3(a) is an example of a higher conductivity coating on a lower conductivity material (Al on Ti-6Al-4V). The second set, Fig. 3(b) is the inverse of the first set (Ti on 7075Al). Figure 4 shows experimental measurements of the peak height $\Delta i(t)$ for the ten aluminum foil specimens on Ti-6Al-4V compared to theoretical predictions.

A careful examination of the results reveals that the Δi versus t curves exhibit three key features: the peak height, the peak arrival time and the zero-crossing time. The peak height varies most strongly with layer thickness. Consequently we expect that the peak height of $\Delta i(t)$ will be strongly correlated with layer thickness. The peak height of $\Delta i(t)$ can serve as a sensitive measure of layer thickness if the layer is uniform and its conductivity is known. As is evident from the comparison of the two cases shown in Fig. 3, the signal is sensitive to both the thickness of the coating and the conductivity of the underlying material. Although the peak arrival time and zero-crossing time do not change so obviously with thickness, they can also be used as important parameters for inferring the thickness and conductivity simultaneously. We have developed a rapid inversion method to determine the thickness and conductivity of conductive coatings based on these three parameters.

For most of the cases we have studied, experiment and theory agree very well. For the cases reported here, the experimental and theoretical maxima in $\Delta i(t)$ agree within 3%, with no adjustable parameters. Among all the cases studied, the lowest level of agreement between theory and experiment was for low conductivity layers on low conductivity metals (*e.g.*, Ti on stainless steel); there the agreement was still within 6%. Nevertheless, experience shows that the measurement results are affected by coil heating. Because of this effect, the observed signal can drift if the sample is not allowed to reach thermal equilibrium. Different parameters are affected differently. The peak height is the least sensitive to the heating effect of the coil, while the zero-crossing time is affected most. Our inversion method will reflect this difference by assigning different uncertainties to the key features in the inversion procedure.

In developing a method to measure the thickness and conductivity of layered solids, it is helpful to understand the phenomena occurring. We next describe the physics that results in the signal's key features. First, we analyze the signal's characteristic shape. Consider the signal $\Delta i(t)$ that results from measuring the current when the coil is next to a piece of metal minus the current when the coil is in free-space. The step-function voltage applied to the coil induces a transient current in the metal (the eddy-current) that flows in the direction opposite to the current in the coil. At early times, the eddy-current is weak, since the applied magnetic field has not yet penetrated far into the metal. As time goes on, the magnetic field penetrates more completely and the strength of the eddy-current reaches a maximum. At late times, the eddy-current decays to zero due to the electrical resistance of the sample. The measured signal is therefore the change in the coil's current due to the eddy-current in the metal. By Faraday's law, the change in the coil's emf (and thereby the current) depends on $-\partial \Phi / \partial t$, where Φ is the eddy-current-induced magnetic flux threading the coil. At early times, the eddy-current-induced emf at the coil is negative since the flux is increasing. At late times, the coil's eddy-current-induced emf is positive since the flux due to the eddy-current is decreasing. These considerations explain the characteristic shape of pulsed eddy-current signals shown in Fig. 3(a). The signal starts at zero, decreases to a minimum, then increases, becomes positive and then decays to zero at late time.

The signal is the coil's current measured next to the layered sample minus the current measured next to the reference sample. For both sample and reference, the current that would otherwise flow in the coil is reduced by the eddy-current. Suppose that the metal layer has a higher conductivity than the base metal. The layer screens more strongly and consequently

reduces the current more than the base metal. Hence, as shown in Fig. 3(a), the change in the coil's current is negative at early times. On the other hand, if the layer's conductivity is less than the base metal, the signal is positive at early times, in agreement with Fig. 3(b).

The thickness of the layer is an important variable that we wish to measure. Suppose that the layer thickness is less than the skin depth of the highest frequency in the pulse. The additional screening induced by the layer will increase with the layer's thickness.

Consequently, the peak height is relatively small for thin layers and initially increases rapidly with thickness as shown in Fig. (4). However, for thick layers the signal strength rolls-off and the peak height becomes insensitive to the thickness. This arises when the thickness exceeds the skin depth and the eddy-currents are no longer strongly influenced by the interface. The time of the zero-crossing also depends on the thickness of the layer, because the excess eddy-currents due to the layer rise in a characteristic time that is roughly equal to the thickness of the layer divided by the group velocity of the eddy-currents

[$v_g \equiv (\partial\alpha / \partial\omega)^{-1}$]. Since the propagation of eddy currents is a diffusive (and thus, dispersive) process, we evaluated the group velocity at the center frequency. Consequently, the zero-crossing time increases rapidly with layer thickness.

The conductivity of the layer is the second important variable that we wish to measure. The screening is greater for higher conductivity metals. Thus, we expect the signal to increase with increased contrast between the layer and the base metal. As the conductivity of the layer is varied, we find from the calculations that the signal height changes nearly linearly with the conductivity difference. On the other hand, the calculations show that the zero-crossing is only weakly dependent on the conductivity. This weak dependence appears to arise from two

compensating effects. The group velocity (at a fixed frequency) decreases with increased conductivity. However, the maximum penetration depth also decreases with increased conductivity. Since the zero-crossing time is, in part, a ratio of these quantities it depends weakly on the conductivity. In fact, measurements and calculations show that the zero-crossing time increases only slightly with increased conductivity.

This physical reasoning gives some insight into the inverse problem of determining the layer's conductivity and thickness. First, the zero-crossing depends relatively strongly on the layer thickness but relatively weakly on its conductivity. Hence, we expect the zero-crossing will be important in determining the layer's thickness. On the other hand, the peak height depends strongly on both the thickness and conductivity, and provides an estimate for the conductivity once an estimate for the thickness is available.

IV. Inversion method

In this section we describe a method for estimating the thickness and conductivity of a surface layer from PEC measurements. The complexity of the problem arises from the need to estimate the conductivity and thickness of the layer simultaneously. If either were known, it would be relatively trivial to estimate the other. We would simply determine the unknown parameter from the peak height, which is the feature of the data that varies most strongly with thickness and conductivity.

Moulder *et al.*¹ examined the inversion problem using frequency domain data. They fitted the real part of the measured impedance to theory using a least-squares norm. Good results were obtained. However, this method required approximately 20 CPU min on a DEC

5000 workstation for the analysis of each set of measurements. Sethuraman and Rose¹⁰ developed a more rapid (several seconds on the same processor) solution that was based on isolating three characteristic features of the frequency domain response and then relating the thickness and conductivity to these features. Baltzersen¹¹ independently developed a lookup approach to the more limited problem of determining the thickness of unsupported metal plates.

We developed a lookup table approach for determining the thickness and conductivity of surface layers from pulsed eddy-current data. There are three unknown parameters in the problem: the conductivity of the substrate metal, the conductivity of the layer, and the thickness of the layer. We will assume that the conductivity of the substrate is known *a priori*. We isolated the following features of the pulsed eddy-current response: (1) peak height (PH), (2) peak arrival time (PT), and (3) zero-crossing time (ZT). Of these parameters, the peak height appears to vary most strongly with thickness (see Figs. 3 and 4). The peak arrival time varies next most strongly with thickness. The zero-crossing time, owing to the effect of thermal-drift in the signal, is the most unreliable estimator. We built a lookup table based on these features (PH, PT, and ZT) to estimate the layer's thickness and conductivity. The lookup table makes the inversion time small in comparison with the measurement time.

The lookup table was constructed by computing $\Delta i(t)$, extracting the crucial three features and tabulating them along with the thickness and conductivity. The table ranges over thickness from 0.02–1.4 mm and conductivity from 0.5–71 MS/m. The conductivity of the substrate and the dimensions of the probe coil are assumed to be known; if these change the table must be recomputed.

The determination of thickness and conductivity can be described schematically as follows:

1. construct a lookup table by computing $\Delta i(t)$ for a range of layer thickness and conductivity for a specified substrate and probe coil;
2. measure the peak height, the peak arrival time and the zero-crossing time and estimate the uncertainty in each quantity;
3. compare the calculated and measured features by looking through the table. Identify each estimated layer conductivity and thickness that is consistent with the measurements and the estimated uncertainty;
4. report the arithmetic average of the estimated thickness and conductivity values so identified.

The scheme outlined above modifies the method of Sethuraman and Rose as follows.

There is a certain inevitable imprecision in the measurements that leads to an uncertainty in the predicted values of the thickness and conductivity. After an empirical study of the experimental measurements, we concluded that the key features of the signal could be reliably measured with the following precision $PH = \pm 2\%$, $PT = \pm 10\%$, and $ZT = \pm 10\%$. In our approach, we find all possible values of the thickness and conductivity that are consistent with the measured key features and the quoted precision of the data. Finally, we report the arithmetic average of all values of the thickness and conductivity that fall within the bounds of experimental uncertainty.

V. Results

We report on the accuracy of the lookup table method for estimating layer thickness and conductivity from experimental data in this section. The following types of samples were considered: copper foils on a stainless steel substrate, titanium foils on an aluminum alloy, and aluminum foils on a titanium alloy. Each measurement was repeated five times. Table III summarizes the results for all samples; the ranges of the inferred thickness and conductivity indicate the minimum and maximum values found. Figures 5(a) and 5(b) illustrate estimates for the thickness and conductivity of copper layers on stainless steel. Figures 6(a) and 6(b) show the same estimates for titanium layers on 7075 aluminum. Figures 7(a) and 7(b) show the results for aluminum foils on Ti-6Al-4V. The vertical bars in each figure indicate the range of values inferred.

The figures and Table III show that the thickness and conductivity can be inferred simultaneously with reasonable accuracy from pulsed eddy-current data. The error in determining thickness was usually less than the error in determining conductivity. For example, the average error in multiple independent determinations of the thickness of a Ti layer on an aluminum alloy substrate ranged from 0.5% to 4.3% over the five cases studied, but the average error in determining the conductivity of the Ti layers ranged from 2% to 30%. These results were the worst of the three cases reported. The best results were obtained for Cu on stainless steel. There, the average error among independent determinations of thickness ranged from 0%–13%, while the average error in conductivity ranged from 0.7% to 3%. Average errors in measuring aluminum layers on titanium alloy were 0%–11% for thickness and 5%–20% for conductivity.

As we indicated previously, it is relatively easy to infer the layer's conductivity if its thickness is known and *vice versa*. As shown in Fig. 7(b), the estimate for the layer's conductivity is close to the actual value but is somewhat overestimated. This overestimate is almost completely removed if the thickness of the layer is given *a priori* as shown in Fig. 8(b). The already good estimate for the thickness [Fig. 7(a)] is also improved if the conductivity is known *a priori* as shown in Fig. 8(a).

VI. Discussion

We have demonstrated a rapid and low-cost method that is suitable for determining the thickness and conductivity of layers of nonmagnetic metals on nonmagnetic, conductive substrates. In contrast with some earlier work,⁴⁻⁸ we were able to quantitatively model the pulsed eddy-current response and thus to predict the thickness and conductivity of the layer without artifact calibration standards. Consequently, the method can be applied to a wide range of layered metals without the need for a large and relatively expensive library of reference specimens. Compared with the previously developed swept-frequency technique,¹ the present approach is simpler and faster; the equipment is less expensive and can easily be made portable. Since the measurements are hundreds of times faster, the sensitivity to probe wobble is much less critical.

We concentrated on two types of samples for the purposes of exposition: relatively high conductivity layers on low conductivity base metals and *vice versa*. Other types of samples were studied including low conductivity layers on a low conductivity substrate such as

titanium on stainless steel. Because of the low conductivity of both materials, the signal was smaller, the problem of drift more serious, and the effect of noise relatively more important.

The utility of our inversion method depends in part on the relative size of the coil and the thickness of the layer. For example, the decay of the eddy-currents depends not only on the conductivity of the metal but also the size of the coil. As a rule of thumb, the eddy-currents becomes small for distances into the metal that are comparable to or greater the radius of the coil. Thickness was accurately inferred for layers ranging in thickness from 0.05 to 1.0 *mm*. A larger coil would be needed to size accurately layers thicker than 1.0 *mm*. We have used the same probe to measure very thin layers; e.g. a 12.5 μm aluminum layer on stainless steel. For these thinner samples it was possible using the probe coil in our experimental setup to determine either the thickness or the conductivity, but not both simultaneously. A smaller probe would be needed to extract both parameters simultaneously.

Acknowledgments

This work was supported in part by the NSF Industry/University Center for NDE at Iowa State University. One of us (J.H.R.) was supported by the AFOSR under grant No. F49620-93-1-0438DEF. The authors gratefully acknowledge the work of Mark Kubovich and William Ward III, for their design of the pulsed eddy-current apparatus.

References

- [1] J. C. Moulder, E. Uzal, and J. H. Rose, *Rev. Sci. Instrum.* **63**, 3455 (1992).
- [2] D. H. S. Cheng, *IEEE Trans. Instrum. Meas.* **IM-14**, 107 (1965).

- [3] C.V. Dodd and W. E. Deeds, *J. Appl. Phys.* **39**, 2829 (1968).
- [4] D. L. Waidelich, *Proc. Nat. Electron. Conf.*, **10**, 500 (1955).
- [5] D. L. Waidelich, *Electronics*, **28**, 146 (1955).
- [6] D. L. Waidelich, in *Research Techniques in Nondestructive Testing*, edited by R.S. Sharpe (Academic, London, 1970), p. 383.
- [7] A. Sather, in *Eddy-Current Characterization of Materials and Structures*, edited by G. Birnbaum, and G. Free, (American Society for Testing and Materials, Columbus, 1981), ASTM STP **722**, p. 374.
- [8] D. L. Waidelich, in *Eddy-Current Characterization of Materials and Structures*, edited by G. Birnbaum, and G. Free, (American Society for Testing and Materials, Columbus, 1981), ASTM STP **722**, p. 367.
- [9] J. C. Moulder, M. W. Kubovich, E. Uzal, and J. H. Rose, in *Review of Progress in QNDE*, edited by D. O. Thompson and D. E. Chimenti (Plenum, New York, 1995), Vol. 14B, p. 2065.
- [10] A. Sethuraman, J. H. Rose, *J. Nondestr. Eval.* **14**, 39 (1995).
- [11] O. Baltzersen, *Mater. Eval.* **51**, 72 (1993).

Table I. Coil and measurement parameters for the probe.

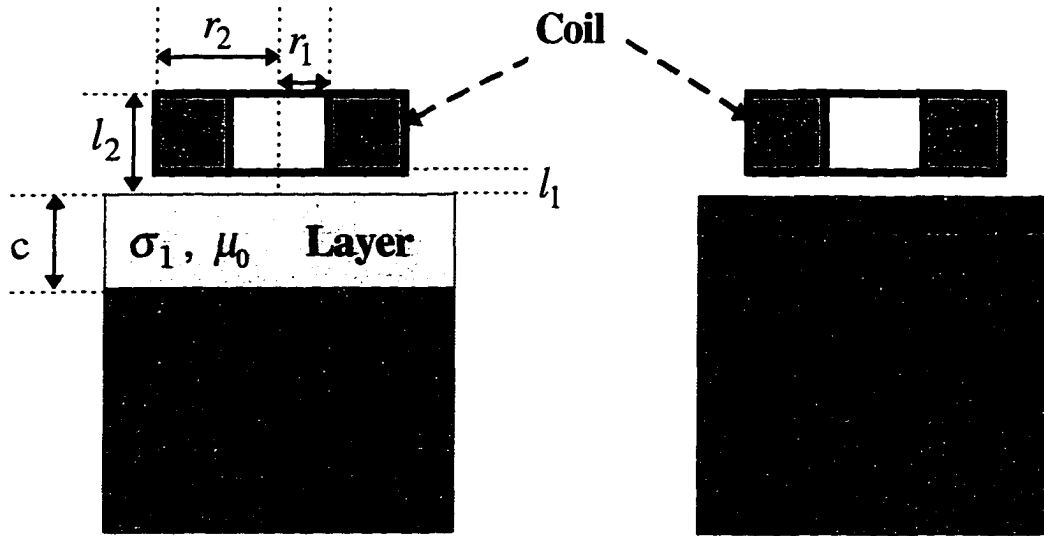
Parameter	Value
Number of turns, N	638
Inner radius, r_1	2.75 mm
Outer radius, r_2	5.64 mm
Height, L	2.65 mm
Lift-off, l_l	0.33 mm
Resistance of coil, R	49 Ω

Table II. Conductivity of the metals used in the experiments.

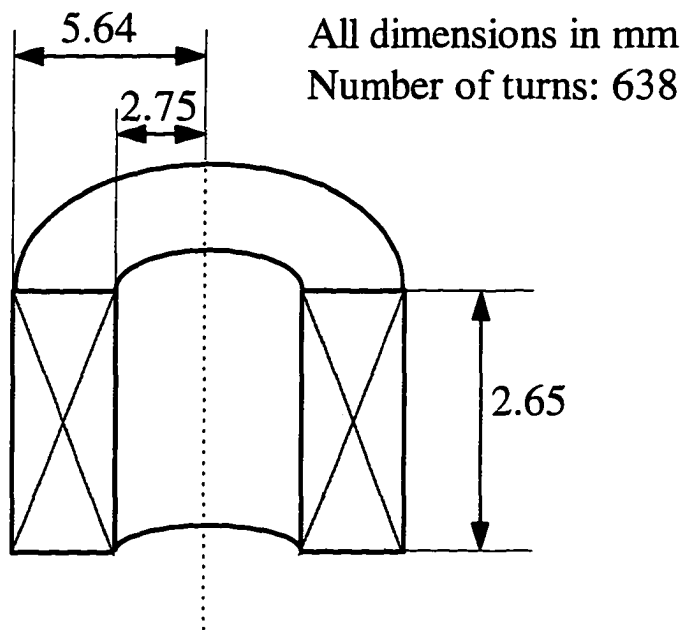
Layer		Substrate	
Material	Conductivity (S/m)	Material	Conductivity (S/m)
Cu	5.80×10^7	SS 304	1.33×10^6
Al	3.77×10^7	Ti-6Al-4V	0.61×10^6
Ti	2.03×10^6	Al 7075	2.32×10^7

Table III. Estimated thickness and conductivity with both parameters determined simultaneously. (The actual value of the conductivity as shown in Table II.)

Layer	Substrate	Thickness (μm)		Conductivity (MS/m)
		Actual	Inferred	
Cu	SS 304	50 ± 1	50–53	57.6–58.3
		100 ± 1	107–111	56.0–56.8
		150 ± 2	146–201	50.9–59.3
		201 ± 1	203–206	58.6–59.3
		251 ± 2	248–294	58.6–56.8
		300 ± 2	329–332	58.8–59.0
		349 ± 4	357–358	57.4–61.0
		402 ± 1	393–429	57.4–61.0
		456 ± 2	444–481	58.1–59.8
		503 ± 1	507–520	58.9–59.5
Ti	Al 7075	41 ± 1	40–44	1.4–1.8
		81 ± 1	80–84	1.2–2.4
		124 ± 1	124–133	2.0–2.9
		163 ± 1	169–171	2.4–2.7
		204 ± 1	200–209	2.2–3.3
Al	Ti-6Al-4V	100 ± 2	92–93	42.4–43.4
		201 ± 1	170–173	44.5–45.0
		305 ± 2	293–310	39.8–40.0
		404 ± 2	240–393	39.6–43.4
		502 ± 8	495–506	39.5–39.6
		605 ± 4	554–549	41.0–41.1
		703 ± 8	573–696	39.7–43.8
		807 ± 5	662–814	38.8–43.0
		904 ± 3	804–899	38.5–41.2
		1005 ± 5	939–969	39.5–40.0



(a)



(b)

Figure 1. (a) Schematic representation of the experiment. (b) Geometry and dimensions of the air-core coil used in the experiments.

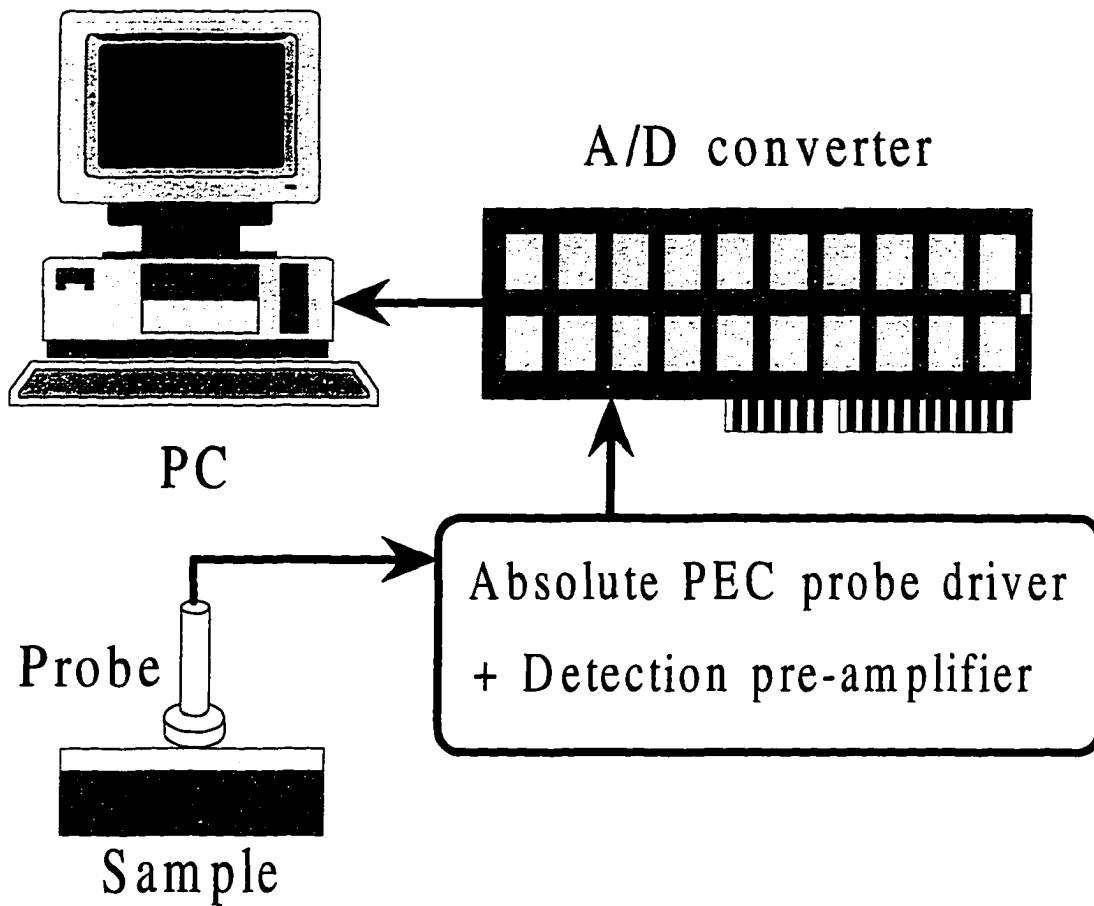


Figure 2. Block diagram of pulsed eddy-current instrument used in this work. The instrument is based on a fast (1 megasample/s) 16 bit A/D card installed in an i486-based PC. The probe is excited with a 5 V, 1 kHz TTL square wave and the current in the coil is monitored by digitizing the voltage across a $1\ \Omega$ resistor in series with the coil.

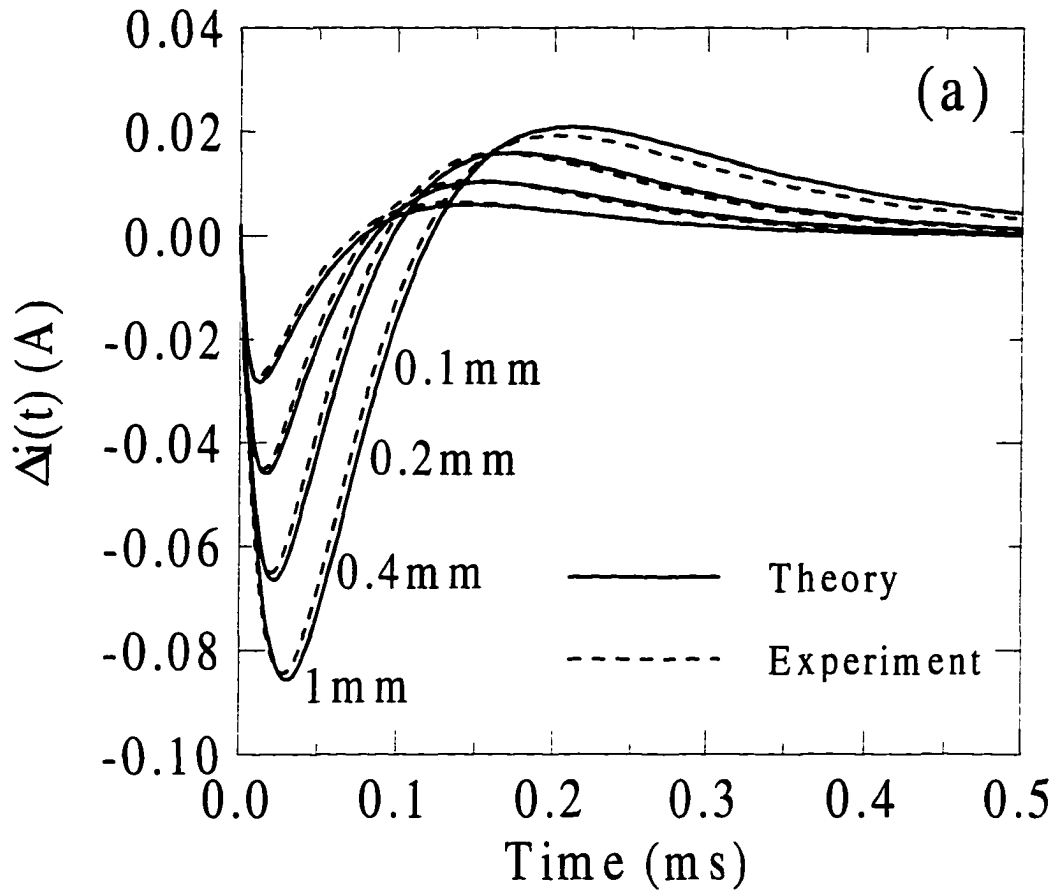


Figure 3. Comparison of theory and experiment for pulsed eddy-current measurements: (a) aluminum foils of different thickness on a titanium alloy substrate; (b) titanium foils of different thickness on a aluminum alloy substrate. As is evident, the agreement is excellent. No adjustable parameters were used in the theory.

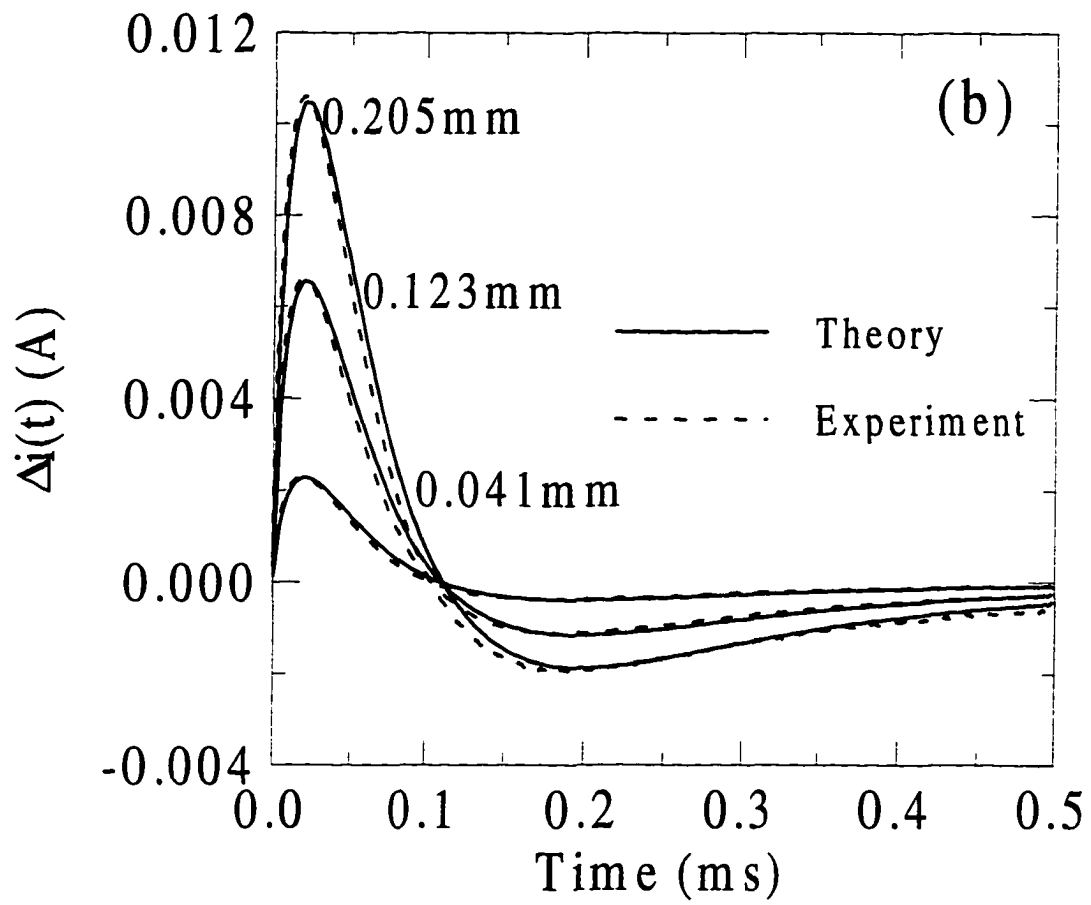


Figure 3. (Continued)

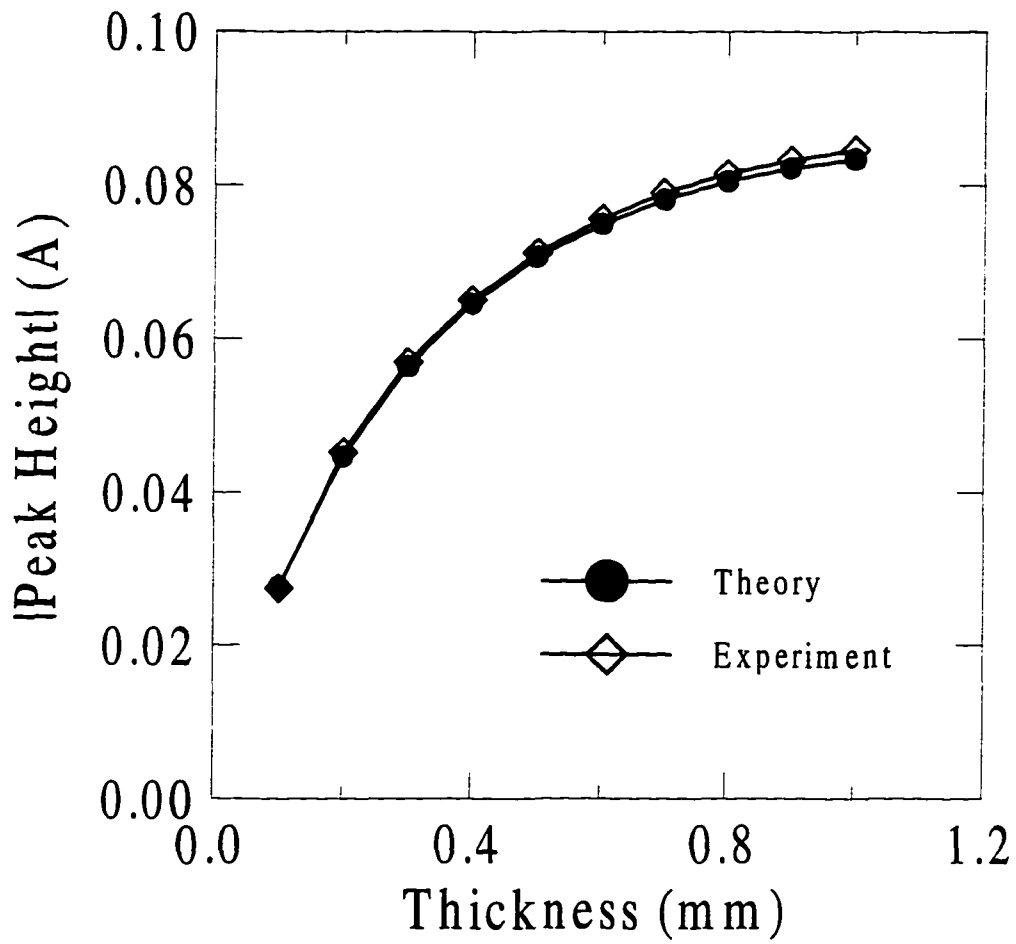


Figure 4. The absolute value of the height of the peak in $\Delta i(t)$ as a function of the thickness of layers.

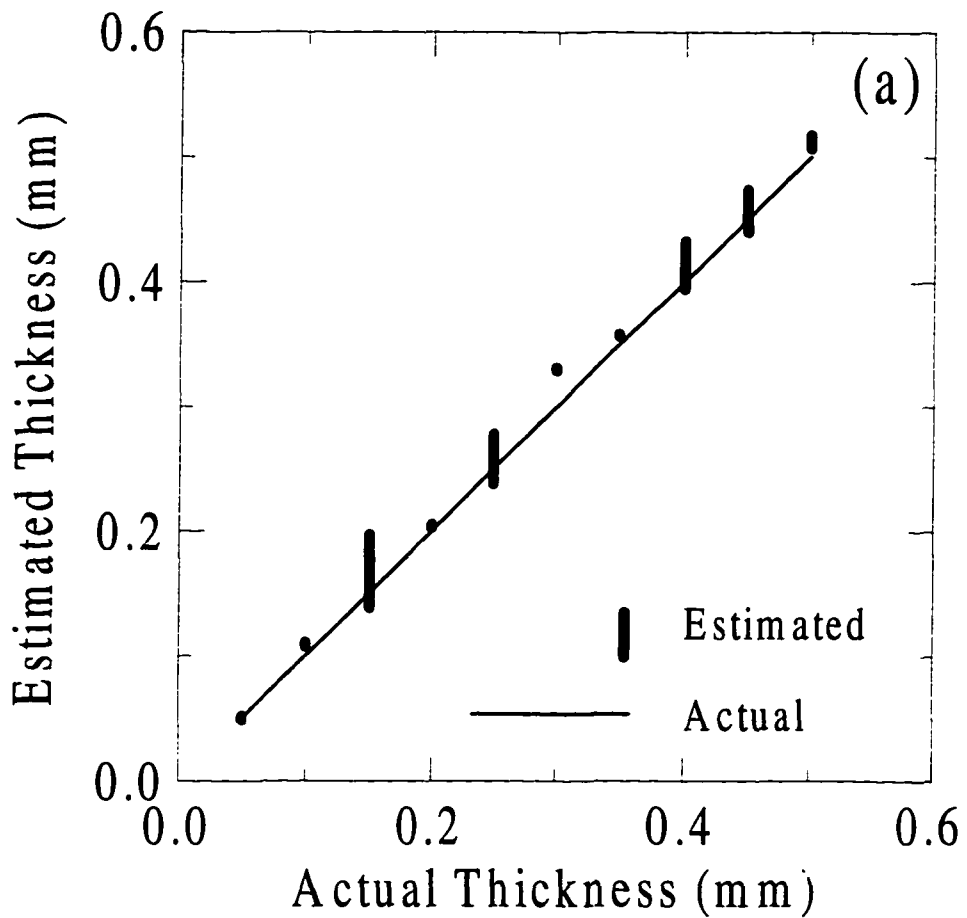


Figure 5. Thickness and conductivity estimated simultaneously for copper layers on stainless steel. The vertical lines indicate the range of the estimates over five separate measurements: (a) estimated thickness plotted vs. actual thickness, and (b) estimated conductivity as a function of layer thickness. The solid line shows the actual conductivity.

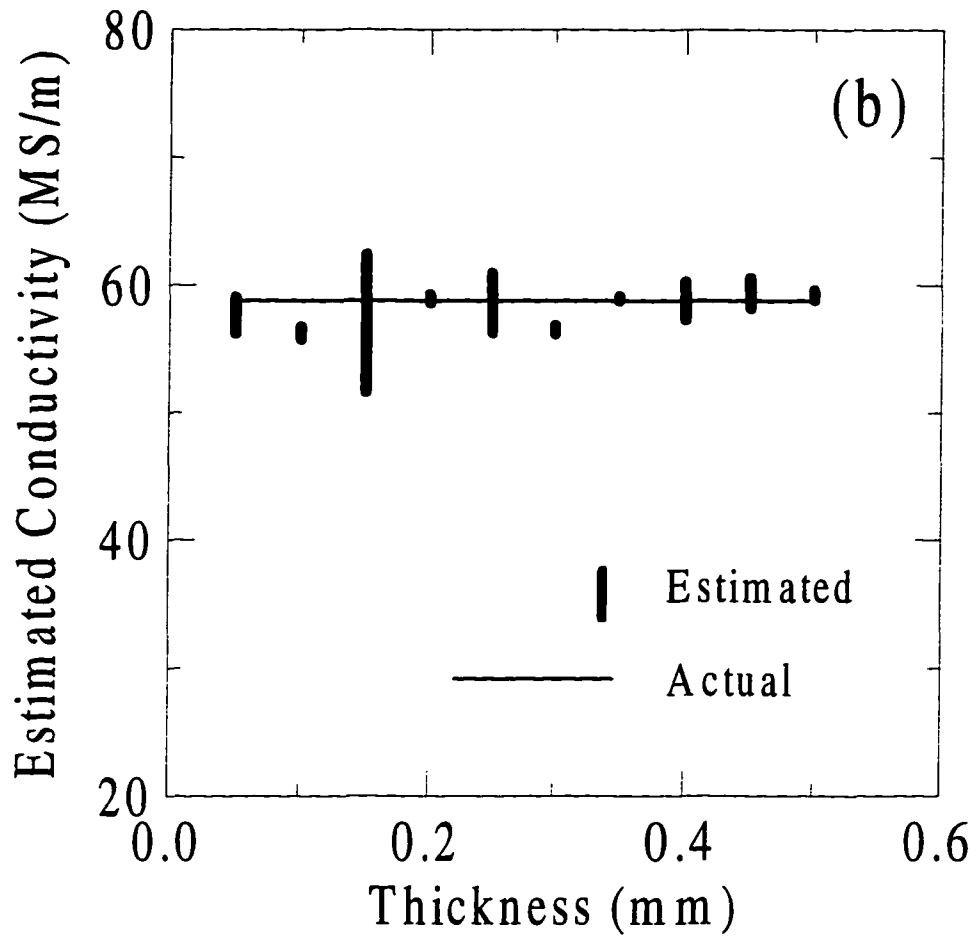


Figure 5. (Continued)

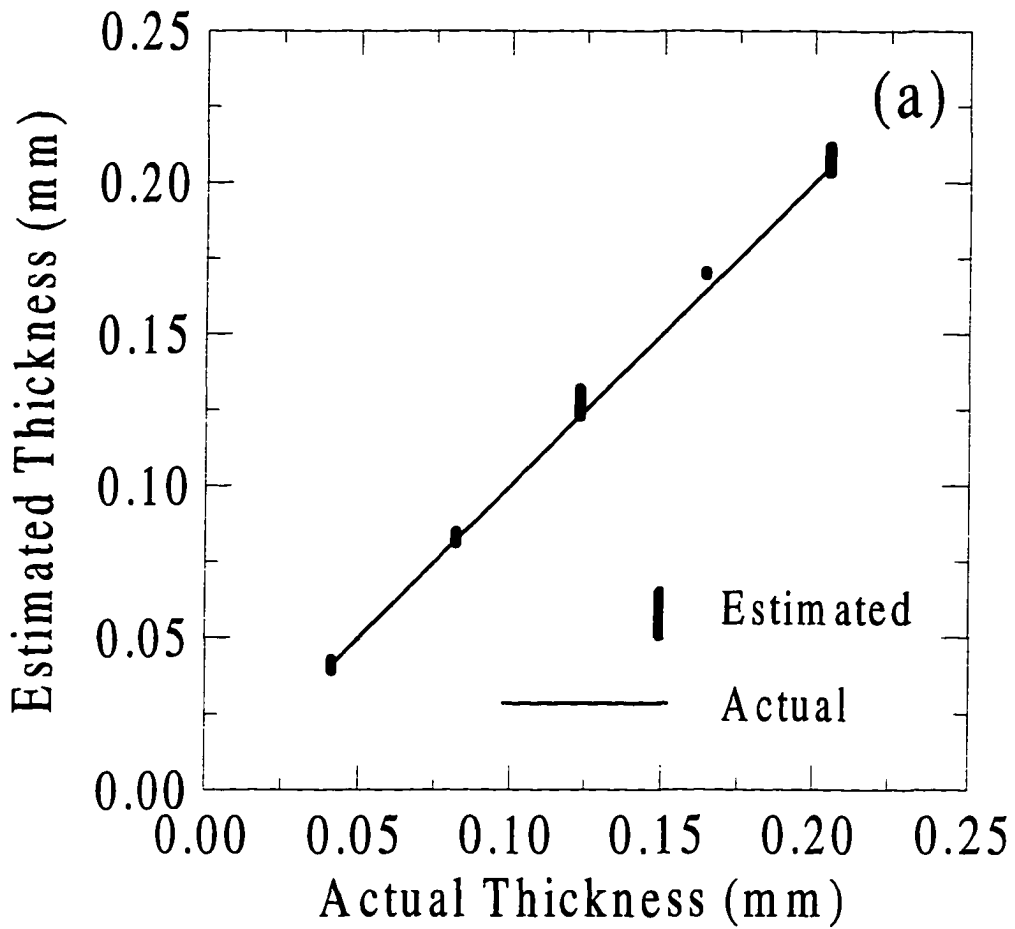


Figure 6. Thickness and conductivity estimated simultaneously for titanium layers on 7075 aluminum. The vertical lines indicate the range of the estimates over five separate measurements: (a) estimated thickness plotted vs. actual thickness, and (b) estimated conductivity as a function of layer thickness. The solid line shows the actual conductivity.

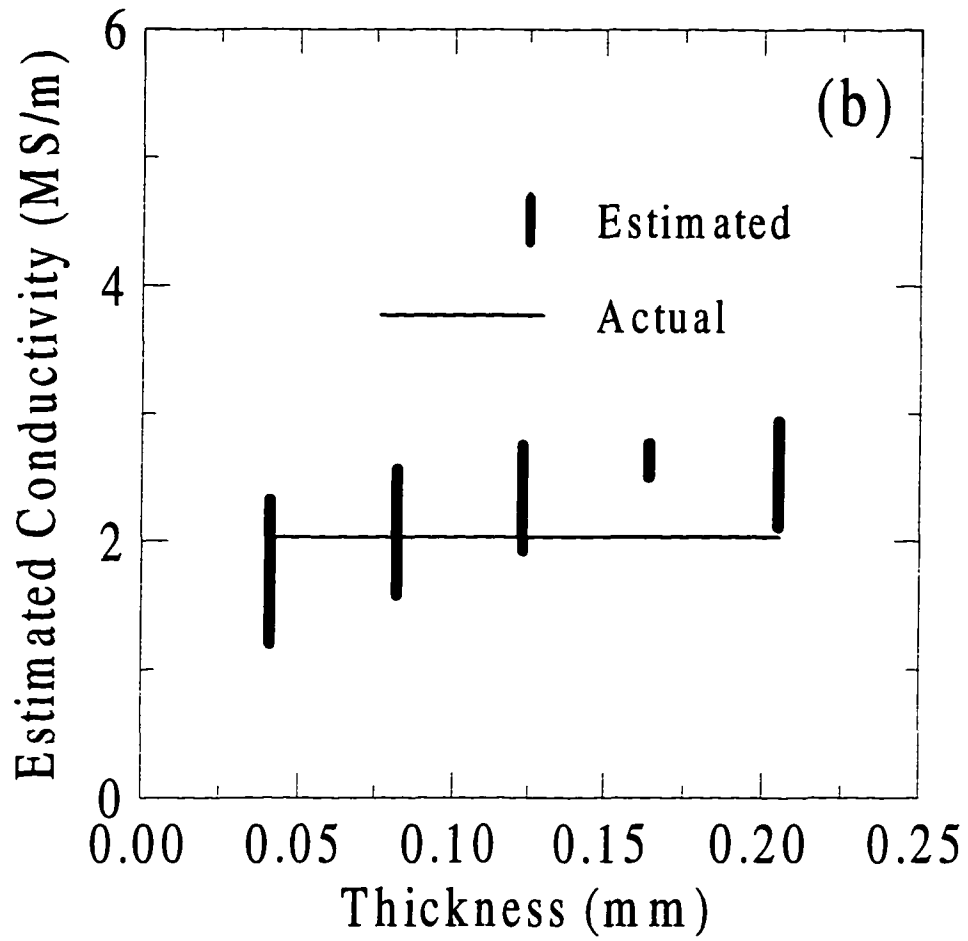


Figure 6. (Continued)

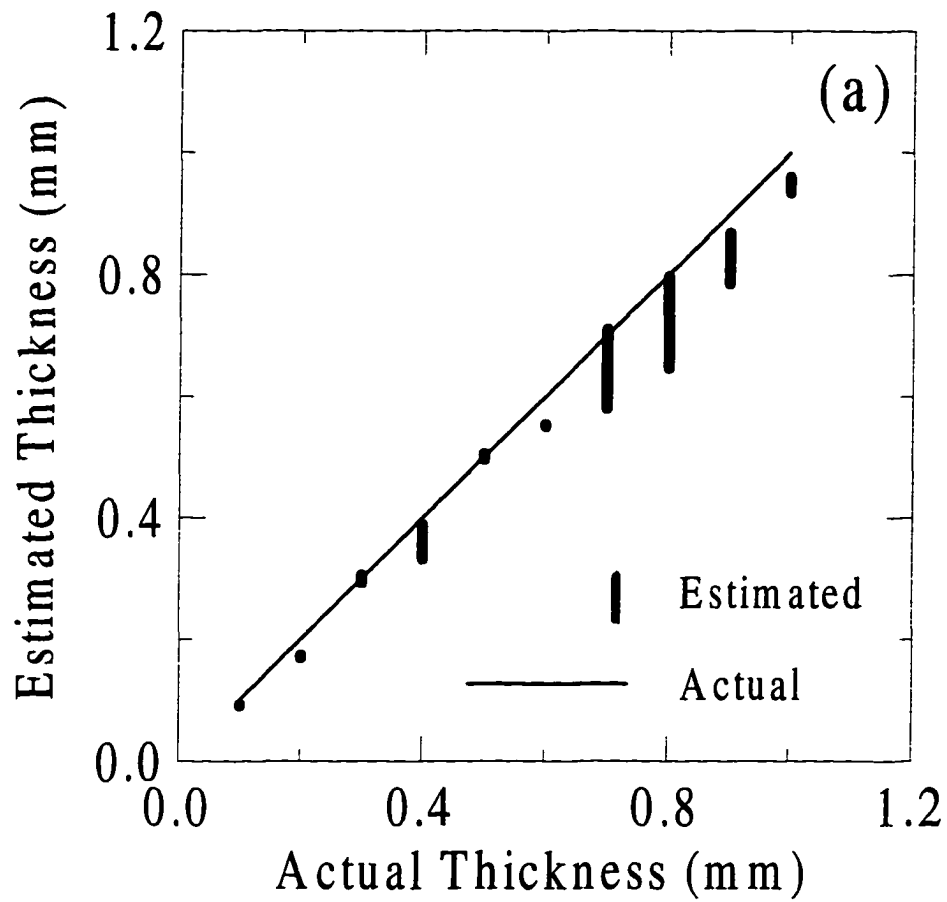


Figure 7. Thickness and conductivity estimated simultaneously for aluminum layers on Ti-6Al-4V. The vertical lines indicate the range of the estimates over five separate measurements: (a) estimated thickness plotted vs. actual thickness, and (b) estimated conductivity as a function of layer thickness. The solid line shows the actual conductivity.

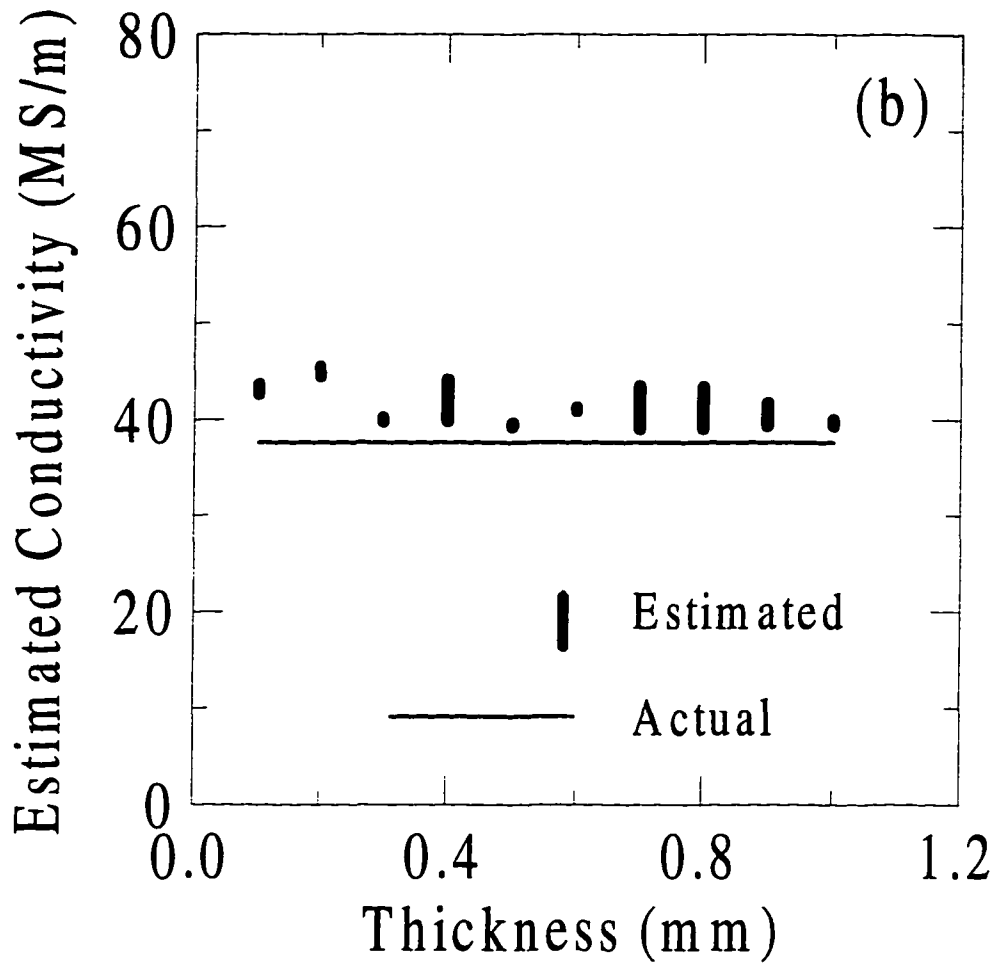


Figure 7. (Continued)

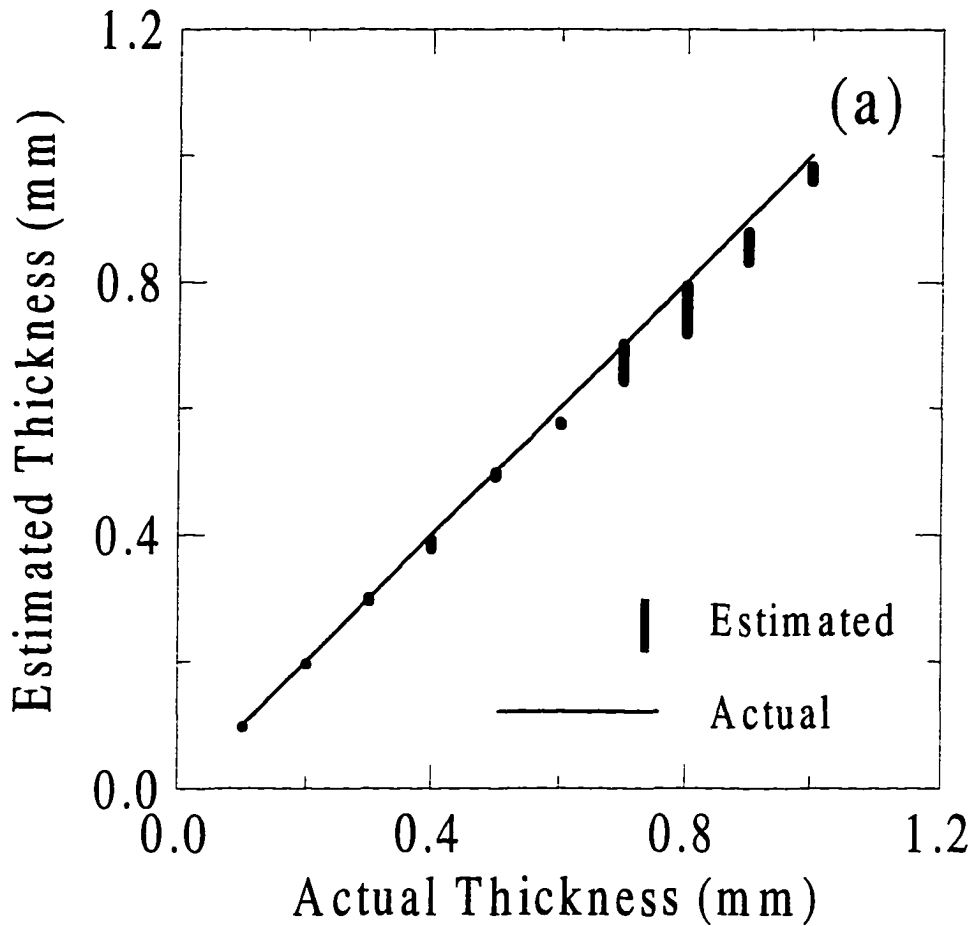


Figure 8. Aluminum layers on Ti-6Al-4V. (a) Estimated thickness plotted vs. actual thickness. The conductivity was assumed to be known. The estimates for the thickness are improved generally. [see Fig. 7(a)] (b) Estimated conductivity as a function of layer thickness; the thickness was assumed to be known. The conductivity estimation improved greatly. [see Fig. 7(b)]

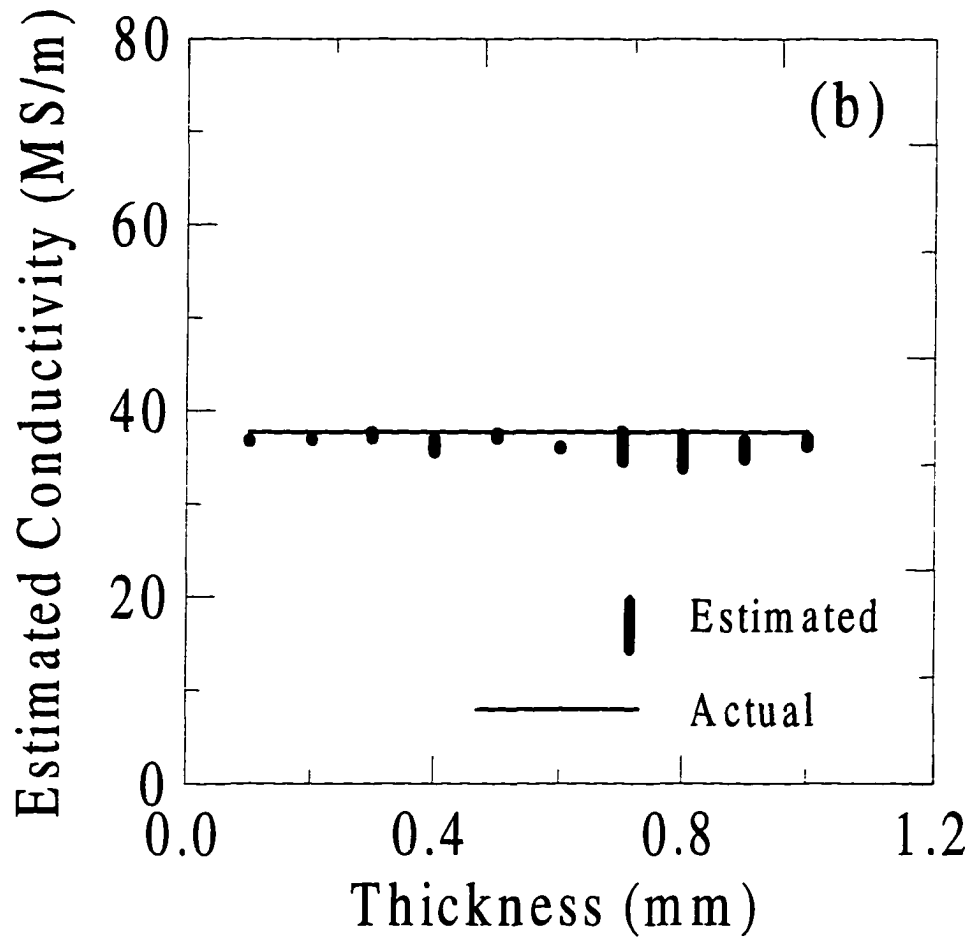


Figure 8. (Continued)

CHAPTER 3.

EXTREME SENSITIVITY OF EDDY-CURRENTS TO THE SURFACE
CONDITIONS OF NICKEL

A manuscript submitted to the *Review of Progress in QNDE*

James H. Rose, Cheng-Chi Tai, and John C. Moulder

Center for Nondestructive Evaluation

I. Introduction

Eddy currents are used to inspect metals for small near-surface cracks and other defects. The eddy-current signal can be calculated quantitatively, at the cost of some effort, for non-magnetic metals at room temperature. Surprisingly, the same cannot be said for ferromagnetic metals [1]. Neither a quantitative nor a qualitative understanding exists for the change in the impedance when an air-core coil is placed next to an otherwise unspecified ferromagnetic metal. Nickel and iron are the ferromagnetic metals most commonly used in commercial applications. The authors are conducting an experimental/theoretical program aimed at developing a fundamental understanding of the swept-frequency impedance of coils placed next to thick plates of these elements. We start with commercially pure nickel.

What is the appropriate model for the impedance of a weakly-excited air-core coil placed next to a ferromagnetic metal? Engineers generally assume that the permeability is local, independent of frequency and spatially isotropic. They also make two additional assumptions that are more questionable. First, they treat the permeability as uniform. Second, they assume that the permeability of the sample doesn't change with time – i.e., there is no significant aging if the reasonable care is taken with the sample. We have found, on the contrary, that any useful model for elemental Ni must include a thin surface layer of greatly reduced permeability – as previously observed for transformer metals and then apparently forgotten [2]. Second, one must account for changes in the permeability with time – i.e., the sample ages.

The theories of Cheng [3] and of Dodd and Deeds [4] allow one to accurately calculate the impedance change for a coil placed next to either a uniform or layered thick plate of *non-magnetic* metal. This theory assumes that the conductivity and permeability are uniform in each layer. We have adopted the same approach for magnetic metals and computed the swept-frequency impedance. This allows us to quantitatively test our understanding of our measurements.

The structure of this paper is as follows. We first describe the samples and the measurement procedures. We then show that it is necessary to include a thin (10 – 100 μm) surface layer of greatly reduced permeability in any model of the eddy-current response of elemental Ni. Next, we show that the eddy-current response of the samples changes over a period ranging from days to months and that the aging is due to atmospheric exposure. Finally, we conclude the paper with a brief summary.

II. Experimental Set-up and Measurements

Measurements were performed using an automated eddy-current work station. The complex impedance of the coil was determined with a Hewlett Packard 4194A impedance analyzer. Measurements were made at 401 equally-spaced frequencies in the range 1 kHz to 1 MHz. A precision-wound and nearly right cylindrical coil, denoted probe L, was used. The inner and outer diameters of the coil were 1.07 and 2.62 mm, the lift-off was 0.62 mm, the coil length was 2.93 mm and there were 235 turns of copper wire in the coil. Measurements were first taken with the probe in air, then with the probe in firm contact with the sample. Data are reported here as the difference of the complex impedance, $\Delta Z = Z_{\text{metal}} - Z_{\text{air}}$.

Three samples, cut from a rod of 99.98% Ni had the shape of right-cylinders with a height of 30 mm and a radius of 12 mm. No special care was taken with the surfaces of the samples when they were initially cut. The surfaces were smooth to the eye and grayish in color. After cutting, the samples were vacuum annealed for two hours at a temperature of 1073 K, furnace cooled and demagnetized. One sample was sacrificed and fashioned into a ring. A very low frequency (0.03 Hz) transformer-based measurement determined that the relative initial permeability of the ring specimen was approximately 300, in good agreement with a handbook value of the static permeability for pure Ni.

III. Results

Extreme Sensitivity to Surface Condition

The change in the coil's reactance depended sensitively the surface condition of the sample. Figure 1 shows the change in the coil's reactance measured on sample 1 for three different

surface states: "as cut and annealed," after the surface was wet-sanded to a smooth finish with 400 grit sandpaper, and after the surface was etched with a chemical polishing solution. $\text{Im } \Delta Z$ was *reduced* by mechanically polishing the surface as shown by the dashed line. $\text{Im } \Delta Z$ *increased* after chemical polishing and was much larger than the result for the mechanically polished surface. Figure 2 shows the change in the eddy-current reactance as sample 2 was repeatedly etched with a chemical polish to remove more and more of the surface material. As can be seen, $\text{Im } \Delta Z$ increased with the removal of surface material and reached its maximum value when 180 μm of Ni was removed. Further polishing caused a small variability in the reactance but no further systematic change was observed.

Aging

The eddy-current signal also depended strikingly on the aging of the sample. For example, the solid line in Fig. 3 shows $\text{Im } \Delta Z$ for sample 2 measured after chemical polishing. The dashed line shows $\text{Im } \Delta Z$ measured for the same sample after six months. The position of the zero-crossing was reduced by more than a factor of two. Our studies of this phenomenon are incomplete. However, Fig. 4 shows recent measurements made on sample 2, following the changes in $\text{Im } \Delta Z$ as the surface was repeatedly etched until the signal quit changing. Measurements were then made on the day of the final etching and every twenty-four hours subsequently. It is evident that the signal decreased significantly over several days.

Exposure to Air

The aging of the nickel samples is due to its exposure to air. We tested this hypothesis in two ways. First, sample 2 was electropolished using a solution designed to passivate the surface with a tenacious sulfide layer a few monolayers thick. The purpose of this fluoride layer was to prevent the exposure of the bare nickel to air. Up to the present time (> five months) no aging has been observed for this passivated sample. Second, we chemically etched sample 1 in the usual way (no passivation) and immediately placed it in a desiccating chamber that was evacuated and back filled with dry argon. No aging was observed for this sample as long as contact with air was prevented. The swept-frequency impedance of sample 1 was unchanged immediately after the sample was removed from the desiccating chamber (after 3 weeks). Aging resumed after the sample was exposed to the atmosphere.

IV. Fit to Model Calculations

We attempted to extract the initial relative permeability from the measurements by assuming that the permeability was uniform throughout the sample (probably a bad assumption from the results given above). If the model were correct, a strong frequency dependence of the initial permeability for the nickel samples would have been necessary to account for the measurements. Similar results were found for other magnetically soft alloys like Permalloy and Armco iron. See Ref. [1] for details. Estimates of the relative permeability of nickel ranged from 30 to 160 depending on the factors mentioned above.

Our measurements lead us to the hypothesis that the permeability is, in fact, *independent* of frequency and that the apparent dependence on frequency arises from the

presence of a surface layer with much lower permeability than in the bulk [2]. The fit between theory and experiment can be significantly improved by assuming that the sample is inhomogeneous and consists of a high-permeability core and a low-permeability surface layer. Figure 5 shows the measured ΔZ for sample 1 as a solid line. The dashed line is a theoretical calculation that assumes a uniform low permeability layer atop a high permeability base metal. The layer was assumed to have a thickness of 10 μm and a relative permeability of 70. The relative permeability of the base metal was assumed to be 200. The fit between the experiment and theory is relatively good. There is some disagreement at the highest frequencies. The estimates for the thickness and permeability of the surface layer are reasonable on the whole.

V. Implications for NDE and Conclusions

The eddy-current response of Ni is sensitive to the surface condition, thermal history, aging and exposure to air. The surface of polycrystalline nickel has a layer of reduced permeability. The apparent permeability of this layer can be *reduced* by mechanical damage. The apparent permeability can be *increased* by chemically removing material from the surface. The apparent permeability also depends sensitively upon thermal history. The apparent permeability of the surface layer is time-dependent, with changes occurring over a period of days and months. Finally, the aging of the sample is apparently caused by the exposure of the samples to air. It is clear that reactance change due to magnetically soft, 99.98% Ni cannot be modeled by regarding the metal plate as a uniform half-space continuum. At the minimum, a quantitative model will have to incorporate the following

features: first, a thin surface layer of low permeability; second, changes in the surface layer with thermal annealing, mechanical and chemical polishing, and with exposure to air.

The primary use of eddy-currents in NDE is to detect cracks. What is an appropriate model for eddy-current inspection of cracks in nickel plates? A layer of reduced permeability exists on the surface of the part and must be included. Our results indicate that the permeability of Ni is very sensitive to the introduction of defects – either by gentle mechanical polishing or by simple exposure to the atmosphere. The formation of a crack is inevitable connected with plastic deformation and the introduction of mechanical defects in the surrounding material. Thus, we expect that the material in the immediate vicinity of the cracks will have a reduced (possibly greatly reduced) permeability compared to bulk metal. In Figure 6 we have indicated schematically the minimum requirements for an eddy-current crack model. First, the crack itself is denoted by the dark line. It is assumed that there is no electrical conduction through this boundary. Next, the lightly cross-hatched region indicates a thin surface layer with reduced permeability (the value of 20 is typical). The darkly cross-hatched region indicates a damage zone around the crack where the permeability is likely to be even lower than in the surface region. The permeability in the damage zone and in the surface layer may be expected to change with time due to atmospheric exposure. The eddy-current signal is expected to depend sensitively on all these features.

What do our results imply for materials of more general industrial use? This question is open. In some ways, elemental nickel is an extreme case, being a magnetically "soft" metal. Indeed, we increased its softness as much as possible by annealing and demagnetizing the sample. Thus, it is not too surprising that it was very sensitive to the introduction of defects,

which tend to lock up the magnetic domains and thus to magnetically "harden" the material. Preliminary work on elemental iron and other magnetically soft metals indicates that results similar to those reported for Ni may be common for these materials. On the other hand, we have little data for magnetically hard materials such as industrial steels – where the domain structure is determined by defects. It may well be that our observations will not generalize well to this class of materials.

Acknowledgments

This work was supported by the NSF Industry/University Center for NDE at Iowa State University.

References

- [1] J. H. Rose, E. Uzal, and J. C. Moulder, "Magnetic Permeability and Eddy Current Measurements," in *Review of Progress in Quantitative NDE*, Vol. 14, edited by D. O. Thompson and D. E. Chimenti, Plenum Press, New York, p. 315 (1995).
- [2] E. Peterson and L. R. Wrathall, "Eddy Currents in Composite Laminations," *Proceedings of the Institute of Radio Engineers* 24, p. 275 (1936).
- [3] D. H. S. Cheng, *IEEE Trans. Instrumentation and Meas.* IM-14, 107 (1965).
- [4] C.V. Dodd and W. E. Deeds, *J. Appl. Phys.* 39, 2829 (1968).

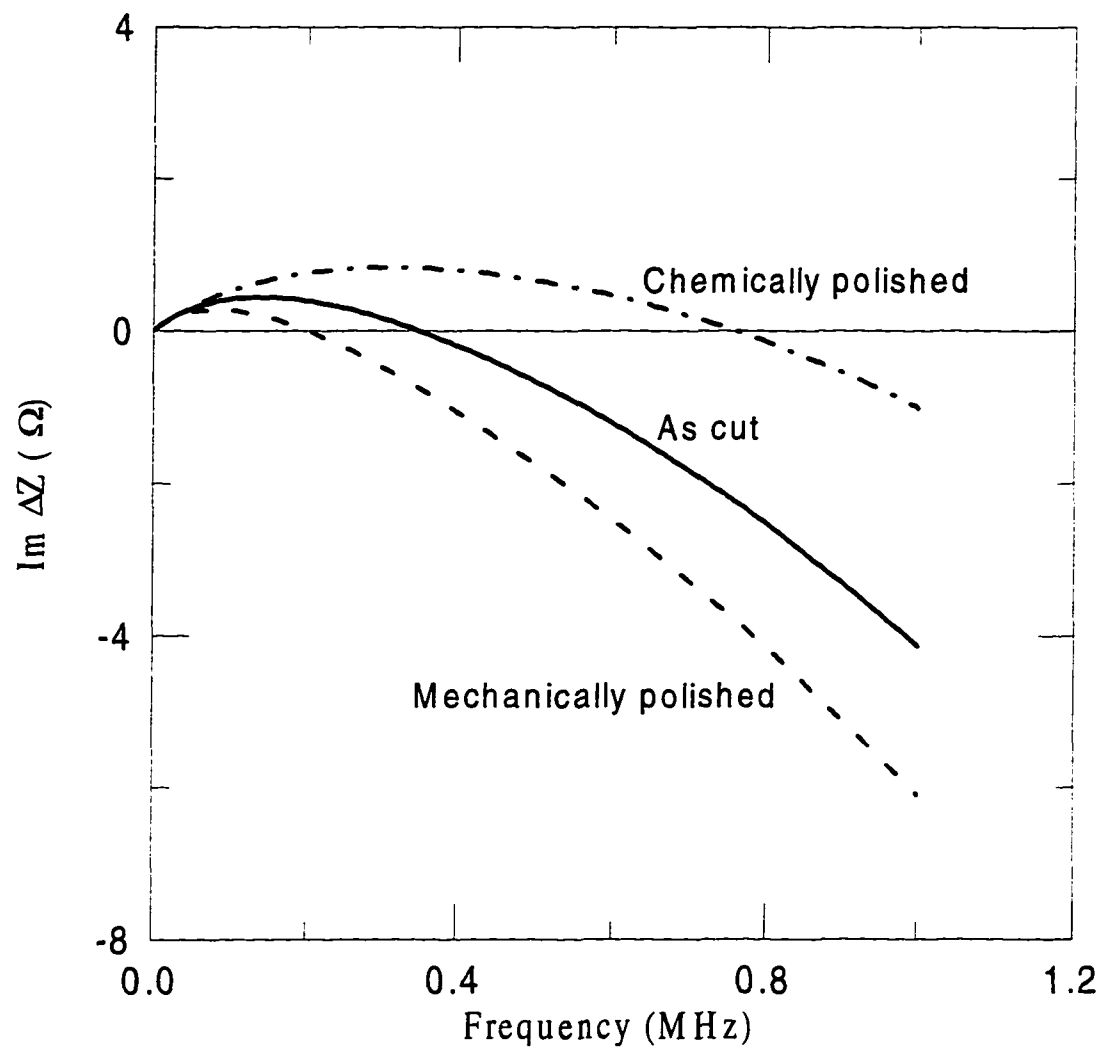


Figure 1. Shows Im ΔZ for Ni specimen after anneal and following surface treatments.

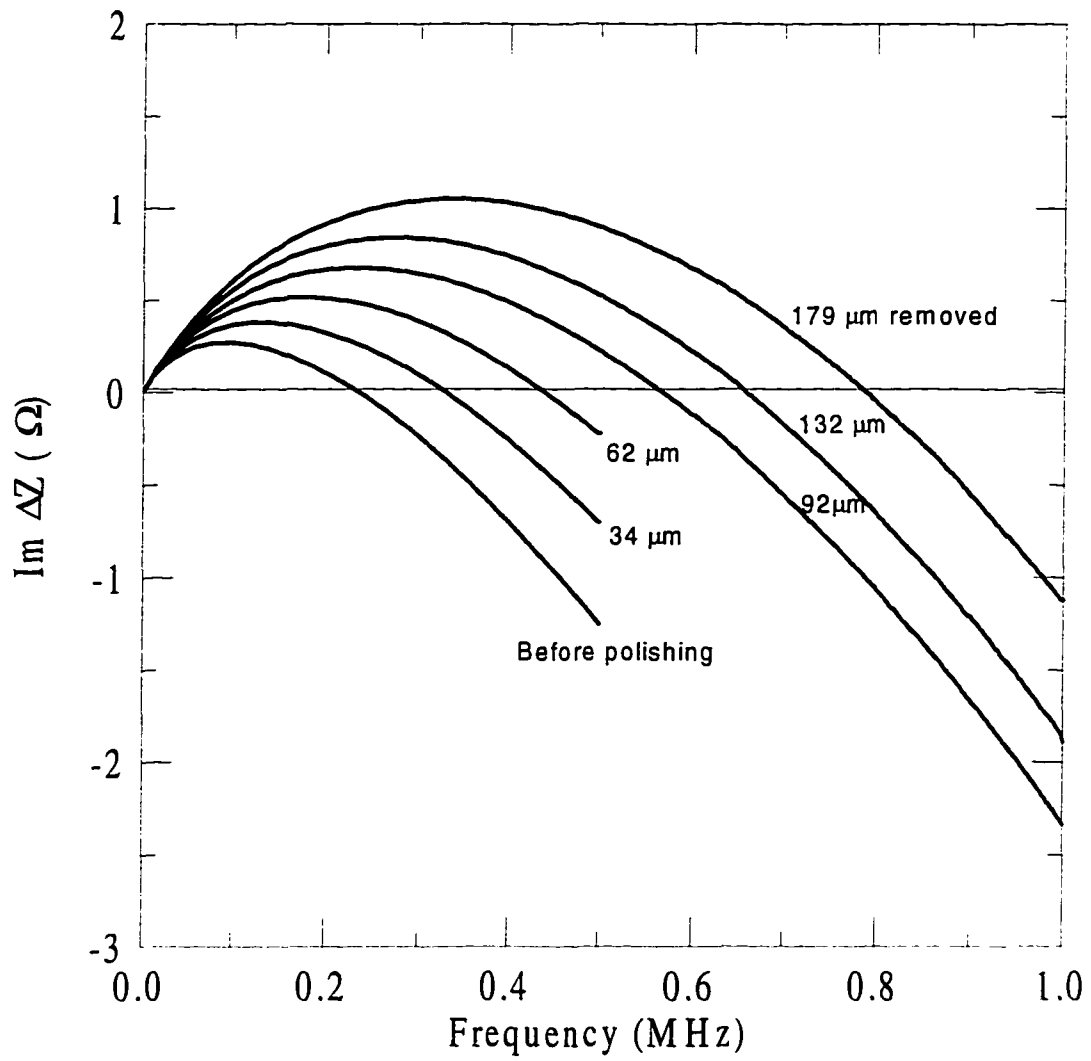


Figure 2. Shows $\text{Im } \Delta Z$ for Ni specimen with progressive etching.

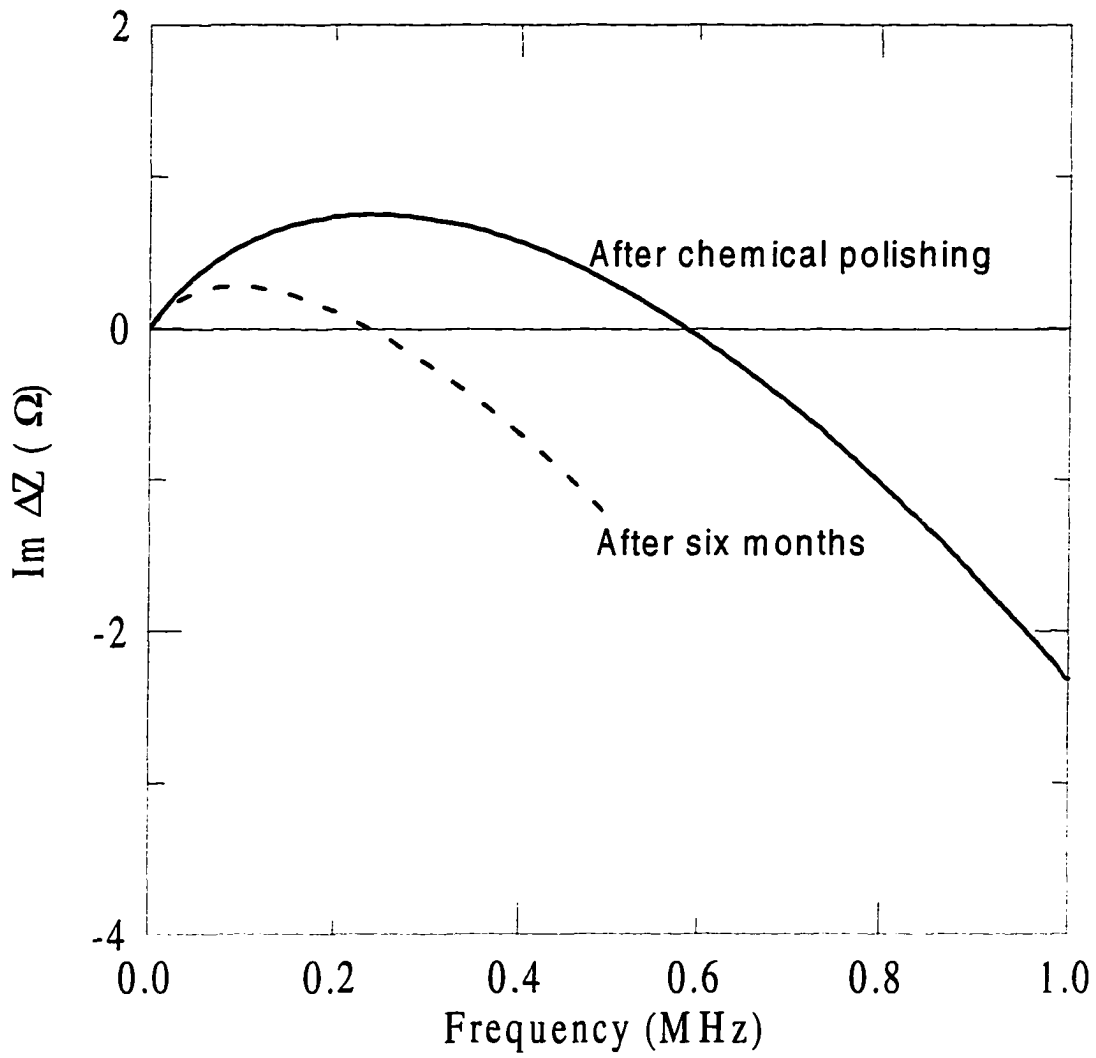


Figure 3. Effect of aging on $\text{Im } \Delta Z$ for Ni specimen.

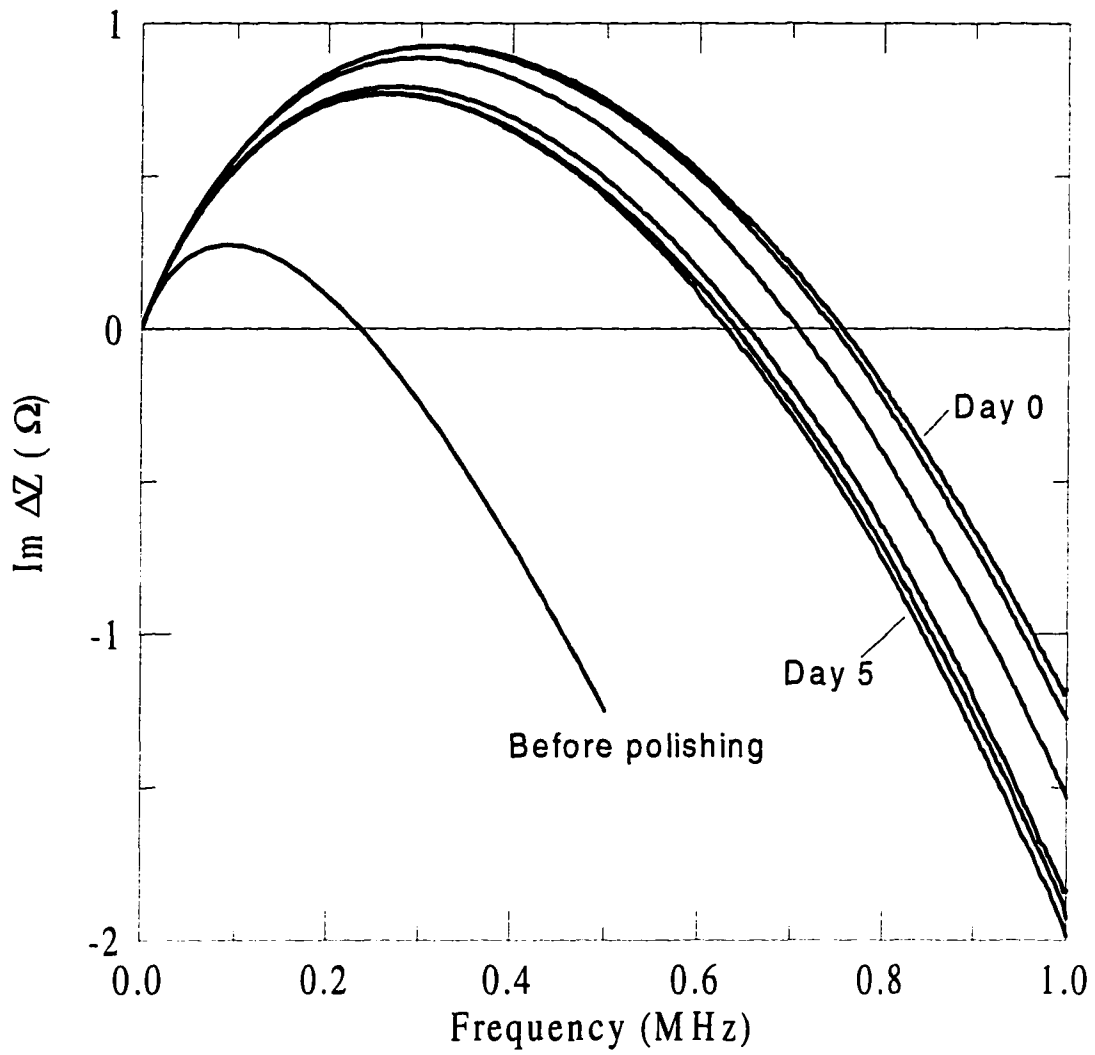


Figure 4. Prompt changes in $\text{Im } \Delta Z$ for Ni specimen after etching.

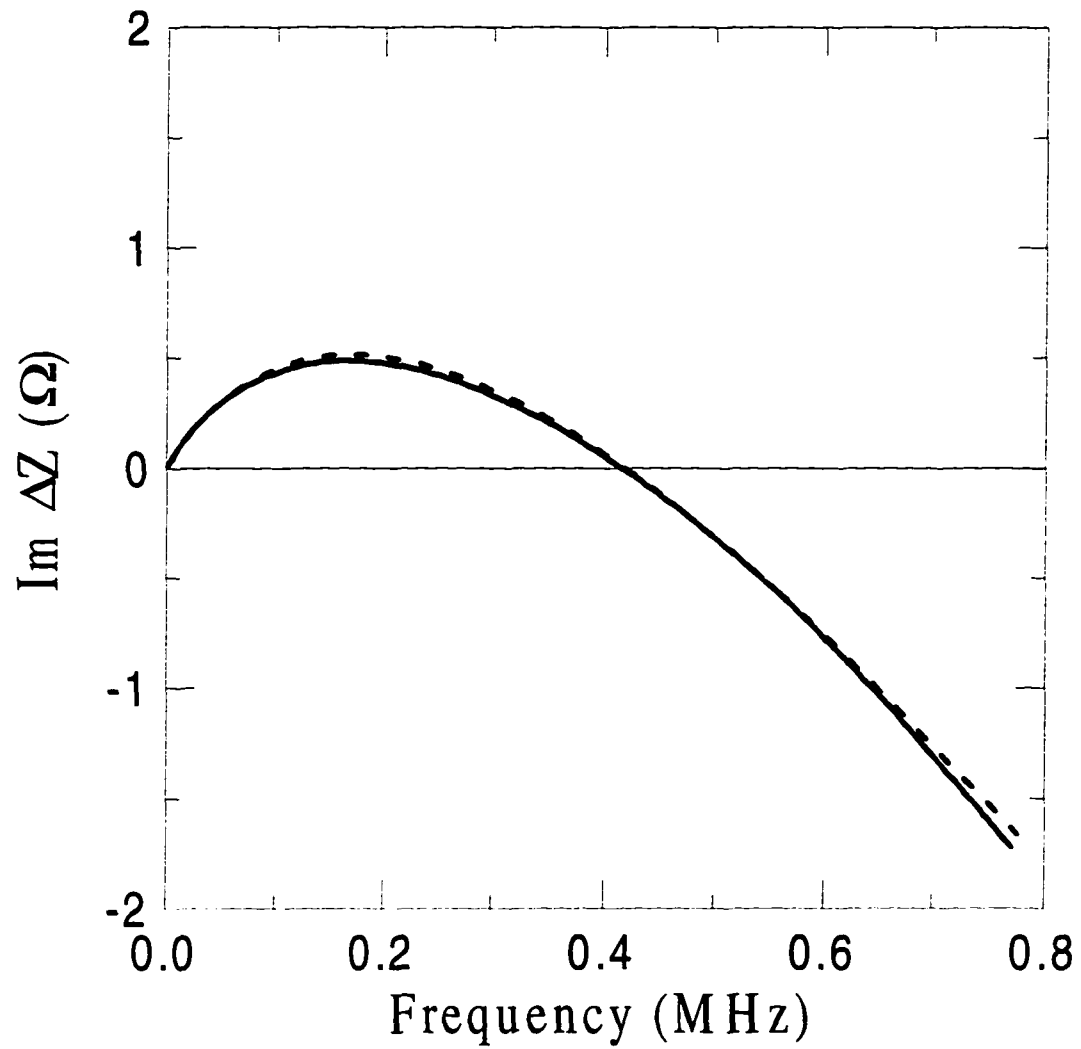


Figure 5. Compares measured impedance change as a function of frequency for a chemically etched and annealed sample with calculation for a sample with a surface layer of reduced permeability.

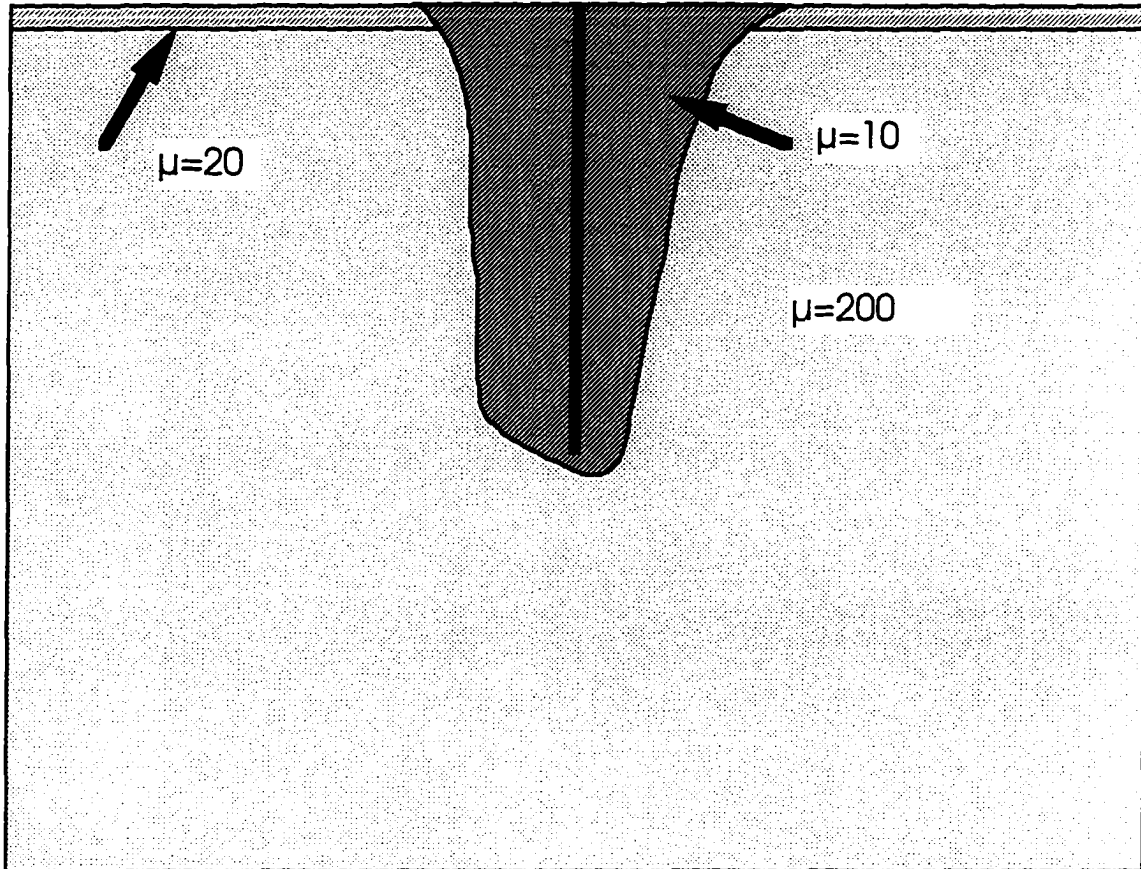


Figure 6. Schematic drawing of a crack in a Ni plate. The surface layer is indicated by the light cross-hatching, while the damage zone is indicated by the dark cross-hatching.

CHAPTER 4.

CHARACTERIZATION OF COATINGS ON MAGNETIC METALS USING SWEPT-FREQUENCY EDDY CURRENT AND TRANSIENT EDDY CURRENT METHODS

A manuscript submitted to the *Review of Progress in QNDE*

Cheng-Chi Tai, James H. Rose, and John C. Moulder

Center for Nondestructive Evaluation

I. Introduction

Eddy currents can be used to characterize the conductivity and thickness of coatings on metals. However, when the same techniques were applied to magnetic metals, some uncertainties were found. We have discovered that the broadband behavior of eddy current coils in proximity to ferromagnetic surfaces depends dramatically upon very thin surface layers. For nickel, we found a 10–100 micrometers thick dead layer at the surface that reduces the apparent relative magnetic permeability substantially [1]. Conversely, this extreme sensitivity to surface conditions means that measurement methods can be devised that will be sensitive to very thin surface coatings, on the order of a few micrometers thick or less.

Recently Moulder, Uzal, and Rose [2] developed a swept-frequency eddy current technique for determining the thickness and the conductivity of a conducting layer over a

metal substrate of known conductivity. Their approach was based on an absolute comparison of measurement to an exact solution for the impedance of an air-core coil over a layered metal by Cheng [3] and by Dodd and Deeds [4]. No calibration specimens were either required or used. The approach of Moulder *et al.* provided good estimates for both the thickness and conductivity. Sethuraman and Rose [5] developed a more rapid (several seconds on the same processor) solution that was based on isolating three characteristic features of the frequency-domain response and then relating the thickness and conductivity to these features. Tai, Rose and Moulder [6] developed a transient eddy current method that can determine the thickness and the conductivity of a conducting layer over a metal substrate of known conductivity. A rapid inversion method based on a look-up table was developed to determine the thickness and conductivity.

Previous studies were restricted to nonmagnetic metals. In this paper, we develop a measurement technique using either swept-frequency eddy current or transient eddy current methods for determining the thickness, conductivity, and permeability of metallic coatings on metal substrates for the case when either coating, metal, or both are ferromagnetic. The method involves using the empirically determined permeability of the material as input to the model calculation. We demonstrate this technique for copper layers over nickel substrates, nickel layers over copper substrates, and zinc layers over steel substrates. The latter measurements imply that the new method can be used to characterize the galvanization of steel, an important technological process.

The organization of this paper is as follows. In the next section, we review and develop the theory needed to describe frequency domain impedance for the swept-frequency eddy

current method and the current-voltage response function for the pulsed eddy-current instrument. Then we describe the experimental setup and measurements. Results are described and theory and experiment are compared in the last section. Finally, the paper is concluded with a summary.

II. Theory

Impedance Difference: Swept-frequency Eddy Current Method

The theoretical calculation of the impedance of a right-cylindrical, air-cored eddy-current coil placed over a magnetic, single layered half-space is presented in this section. Figure 1 shows the schematic diagram of the model under study. The conductivity and permeability of the layer is denoted by σ_1 and μ_1 , and that of the substrate by σ_2 and μ_2 . μ_0 is the permeability of free-space. The thickness of the layer is denoted by c . The base of the coil is at a height l_1 above the surface and the top of the coil is at $z = l_2$. The coil parameters of importance are number of turns N , inner and outer radii r_1 and r_2 , and coil length $L = l_2 - l_1$. See Table 1. and Fig. 2. for the parameters and geometry of the coils used in this study.

Cheng, Dodd and Deeds [7] have given analytic solutions for calculating the coil impedance when coils were put above stratified conductors. We present the solutions in an alternative form for the case of two-layer magnetic metals. The coil impedance above a magnetic, single layered half-space is

$$Z_L = K \int_0^\infty \frac{P^2(r_2, r_1)}{\alpha^5} \left\{ 2L + \frac{1}{\alpha} \left[2e^{-\alpha(l_2 - l_1)} - 2 + A(\alpha)\phi(\alpha) \right] \right\} d\alpha, \quad (1)$$

where

$$\phi(\alpha) = \frac{(\alpha\mu_1 + \alpha_1\mu_0)(\alpha_1\mu_2 - \alpha_2\mu_1) + (\alpha\mu_1 - \alpha_1\mu_0)(\alpha_1\mu_2 + \alpha_2\mu_1)e^{2\alpha_1c}}{(\alpha\mu_1 - \alpha_1\mu_0)(\alpha_1\mu_2 - \alpha_2\mu_1) + (\alpha\mu_1 + \alpha_1\mu_0)(\alpha_1\mu_2 + \alpha_2\mu_1)e^{2\alpha_1c}}, \quad (2)$$

$$A(\alpha) = (e^{-\alpha l_2} - e^{-\alpha l_1})^2, \quad (3)$$

$$\alpha_i = \sqrt{\alpha^2 + j\omega\mu_i\sigma_i}, \quad (4)$$

$$K = \frac{j\omega\pi\mu_0 N^2}{(l_2 - l_1)^2 (r_2 - r_1)^2}, \quad (5)$$

and

$$P(r_2, r_1) = \int_{\alpha r_1}^{\alpha r_2} x J_1(x) dx. \quad (6)$$

The impedance of the coil above a layer-free reference half-space is given by

$$Z_{HSP} = K \int_0^\infty \frac{P^2(r_2, r_1)}{\alpha^5} \left\{ 2L + \frac{1}{\alpha} \left[2e^{-\alpha(l_2 - l_1)} - 2 + A(\alpha) \frac{\alpha\mu_2 - \alpha_2\mu_0}{\alpha\mu_2 + \alpha_2\mu_0} \right] \right\} d\alpha. \quad (7)$$

We measure the coil impedance for the coil above single layered half-space and a half-space of the base material. The impedance difference, ΔZ , of the impedance for these two cases is reported.

$$\Delta Z = K \int_0^{\infty} \frac{P^2(r_2, r_1)}{\alpha^6} A(\alpha) \left(\phi(\alpha) - \frac{\alpha\mu_2 - \alpha_2\mu_0}{\alpha\mu_2 + \alpha_2\mu_0} \right) d\alpha. \quad (8)$$

Current Difference: Transient Eddy Current Method

The change in the current induced by a step-function change of voltage in a right-cylindrical, air-cored coil when it is placed next to a layered metal plate compared to when it is placed next to a layer-free reference plate is calculated in this section. The calculation proceeds roughly as follows. We start in the frequency domain. First, we calculate Z_L , the impedance of a right-cylindrical, air-cored eddy-current coil placed next a layered half-space. We also calculate Z_{HSP} , the impedance of the coil placed next to a layer-free reference half-space. We obtain the admittance difference ΔY by subtracting the inverse of Z_{HSP} from the inverse of Z_L . The current difference in the frequency domain, $\Delta I(\omega)$, is obtained by multiplying ΔY by the input voltage $V(\omega)$. Next, we take the inverse Fourier transform of $\Delta I(\omega)$ to get the transient current response. The result, $\Delta i(t)$, can then be compared with measurements.

The transient current, $\Delta i(t)$, due to a step-function applied voltage, is obtained from the inverse Fourier transform of $\Delta I(\omega)$

$$\Delta i(t) = IFT(\Delta I(\omega)) = \frac{1}{2\pi} \int_{-\infty}^{\infty} \frac{\Delta Y(\omega)}{i\omega} \exp(i\omega t) d\omega. \quad (9)$$

Here, $\Delta I(\omega) = \Delta Y(\omega)V(\omega)$ and $\Delta Y = 1/Z_L - 1/Z_{HSP}$ is the admittance difference. Furthermore, $V(\omega)$ is the Fourier transform of the applied step-function voltage $v(t)$. We can further simplify the above formula and one finds

$$\Delta i(t) = \frac{1}{\pi} \int_0^{\infty} \frac{\text{Re}(\Delta Y(\omega)) \sin(\omega t) + \text{Im}(\Delta Y(\omega)) \cos(\omega t)}{\omega} d\omega, \quad (10)$$

since $\Delta Y(t)$ is pure real.

III. Experiment

The experimental setup and measurements are described in this section. Two apparatuses were used in this work — the swept-frequency eddy current system and a newly developed pulsed eddy current system (Fig 3a & 3b). Frequency domain measurements were done by using an automated eddy-current work station. The complex impedance of the coil was determined with a Hewlett-Packard HP 4194A impedance analyzer. Measurements were made at 400 equally-spaced frequencies that ranged from 1 kHz to 1 MHz. The coil and its associated cable were connected to the impedance analyzer and the coil was mounted in a fixture over the specimen to permit placing the coil on the surface in a reproducible manner. Measurements were taken both on the layered material Z_L and on the uncovered substrate Z_{HSP} . Data are reported here as the difference of the two complex impedances, $\Delta Z = Z_L - Z_{HSP}$.

All current difference measurements were taken with a pulsed eddy-current instrument. The pulsed instrument contains two important components. The first is a 1 MHz 16 bit A/D

converter and associated computer. The second is an external apparatus which is responsible for driving the probe, and amplifying the return signal. All the measurements reported here have 500 points lying between 0 μs and 499 μs . The coil and its associated cable were connected to the absolute PEC probe driver and the coil was mounted in a fixture over the sample to permit placing the coil on the surface in a reproducible manner. Measurements of the current were obtained both on the layered material and on a part of the substrate not covered by the layer. We recorded the difference of the two currents, Δi , at each time point.

Two precision-wound and nearly right cylindrical coils were used as probes. The first, denoted probe A, was relatively large; the second was smaller and denoted probe L. Actual dimensions of these probes are given in Table I. The shape of the air-core coil is shown in Fig. 2. It consists of N turns wound in a circular coil of rectangular cross section. The resistance of the coil will be canceled when we calculate the impedance difference. But this value is crucial for calculating the current difference in the time-domain, since the admittance difference, ΔY , is used in this case. The absolute PEC probe driver allows one to measure current changes in the output of a single coil. The idea here is to drive a single coil with a step voltage, and then monitor the resulting time behavior of the current flow. This is a more direct comparison with the way the impedance analyzer works.

Measurements were taken for a variety of samples, including layers of zinc, copper and nickel over steel, nickel, and copper substrates. Nickel and steel are magnetic metals. Eight foil samples of pure nickel were prepared by stacking to different thickness ranging from 0.025 mm to 0.2 mm . Copper foils of thickness ranging from 0.025 mm to 0.2 mm were prepared in a similar fashion using copper 101. Eight zinc foils were used ranging from 0.025

mm to 0.4 *mm*. For most of the measurements we report here these foils were placed in contact with a given substrate and the probe then placed upon the foil. Table II contains the electrical conductivities and permeabilities of the layers and substrates we used.

The method we used to determine the permeability of metals is based on comparing the theoretical estimations to the practical measurements by the swept-frequency eddy current method (Fig. 4.). This arises from the complexities of interaction between the coil impedance and magnetic metals. If the material is conducting and ferromagnetic ($\sigma > 0, \mu_r > 1$) (such as nickel, iron, steel or ferrites), the exciting coil reactance changes in a different way than with nonmagnetic test materials. The flux lines within the magnetic material find portions of their path in such material to have far less reluctance than air. This means that the path of the flux lines is shortened, and then the magnetic flux density in the coil is increased. The coil inductance and inductive reactance increase dramatically when a highly permeable magnetic material is tested. However, if the frequency of the ac current is high enough (up to a megahertz), the influence of eddy currents becomes predominant. The net effect is to decrease the inductance with increasing frequency. A zero-crossing occurs when these two effects are in balance, and it provides a sensitive measure of the ratio μ/σ . If the conductivity is known, it accurately predicts the permeability for the uniform half-space model.

IV. Results

We report the coating thickness estimated from experimental data in this section. Three combinations of foil and substrate metals were studied: zinc, nickel, and copper foils over

steel, copper, and nickel substrates. For most of the cases we have studied, experiment and theory agree fairly well, within 5%, with no adjustable parameters.

Some selected measurements are compared with theory in Fig. 5. Figure 5(a) shows the case for nonmagnetic coatings on magnetic base metal using the frequency-domain eddy-current method. We compare theory and experiment for swept-frequency eddy current measurements of zinc foils of different thickness on a steel alloy substrate. Figure 5(b) shows the case for magnetic coatings on a nonmagnetic base metal using the time-domain eddy-current method. We compare theory and experiment for pulsed eddy current measurements of nickel foils of different thickness on a copper substrate. The permeabilities of the magnetic metals were determined by the method described in the experiment section. As is evident from the comparison of these results, the signal is sensitive to the thickness of the coating and the conductivity and permeability of the underlying material.

Coating thickness can be determined from the features of the signal. Figures 6 and 7 show coating thickness estimation using eddy current methods. We assumed that both the conductivities and the permeabilities of the metals are known. As shown in Fig. 5(a), the key features of the swept-frequency eddy current signal are the peak-height, peak-frequency and zero-crossing frequency. Figure 6(a) compares calculated and measured zero-crossing in the real part of the impedance change between specimen with layer and substrate alone for a series of zinc foils of varying thickness on a steel substrate. Figure 6(b) shows the inferred thickness of zinc foils compared to actual thickness. Thickness was determined from zero-crossing in the real part of impedance change between specimen with layer and substrate

alone by using theoretical prediction of the relation between zero-crossing frequency and thickness.

Figure 7 shows the determination of coating thickness from the pulsed eddy current method. As shown in Fig. 5(b), the features of the pulsed eddy current signal are the peak-height, peak arrival time and zero-crossing time. Figure 7(a) compares calculated and measured peak-height of the current change between specimen with layer and substrate alone for a series of nickel foils of varying thickness on a copper substrate. Figure 7(b) shows inferred thickness of nickel foils compared to actual thickness. Thickness was determined from peak-height of the current change between specimen with layer and substrate alone by using theoretical prediction of the relation between peak height and thickness.

V. Summary

We have developed measurement methods for determining the thickness, conductivity and permeability of metallic coatings on metal substrates for the case when either coating, metal, or both are ferromagnetic. The methods can be quite accurate, and are sensitive to very thin coatings, on the order of several micrometers. This work paves the way for development of new, quantitative methods to characterize surface layers on ferrous materials, such as depth of case hardening.

Acknowledgments

This work was supported by the NSF Industry/University Center for NDE at Iowa State University.

References

- [1] J. H. Rose, C.-C. Tai, and J. C. Moulder, "Extreme Sensitivity of Eddy-Currents to the Surface Conditions of Nickel", in *Review of Progress in QNDE*, Vol. 16, edited by D. O. Thompson and D. E. Chimenti (Plenum Press, New York, 1997).
- [2] J. C. Moulder, E. Uzal, and J. H. Rose, "Thickness and Conductivity of Metallic Layers from Eddy Current Measurements", *Rev. Sci. Instrum.* 63, p. 3455 (1992).
- [3] D. H. S. Cheng, *IEEE Trans. Instrumentation and Meas.* IM-14, p. 107 (1965).
- [4] C. V. Dodd and W. E. Deeds, *J. Appl. Phys.* 39, p. 2829 (1968).
- [5] A. Sethuraman, J. H. Rose, *J. Nondestr. Eval.* 14, p. 39 (1995).
- [6] C.-C. Tai, J. H. Rose, and J. C. Moulder, "Thickness and Conductivity of Metallic Layers From Pulsed Eddy Current Measurements", in *Review of Progress in QNDE*, Vol. 15, edited by D. O. Thompson and D. E. Chimenti, p. 409 (Plenum Press, New York, 1996).
- [7] C. C. Cheng, C. V. Dodd, and W. E. Deeds, *Int. J. Nondestr. Test.* Vol. 3, p. 109 (1971).

Table I. Coil and measurement parameters for the probes used.

Probe	A	L
Number of turns, N	504	235
Inner radius, r_1	3.8 mm	0.535 mm
Outer radius, r_2	5.635 mm	1.31 mm
Height, $l_2 - l_1$	2.42 mm	2.93 mm
Lift-off, l_1	0.125 mm	0.62 mm
Resistance of the coil, R	56.7 Ω	5.83 Ω

Table II. Conductivity and permeability of the metals used in the experiments.

Layer			Substrate		
Material (foil)	Relative Permeability	Conductivity (MS/m)	Material	Relative Permeability	Conductivity (MS/m)
Zn	1	17	Steel	42	5
Ni	17	14.6	Cu	1	58
Cu	1	58	Ni	180	14.6

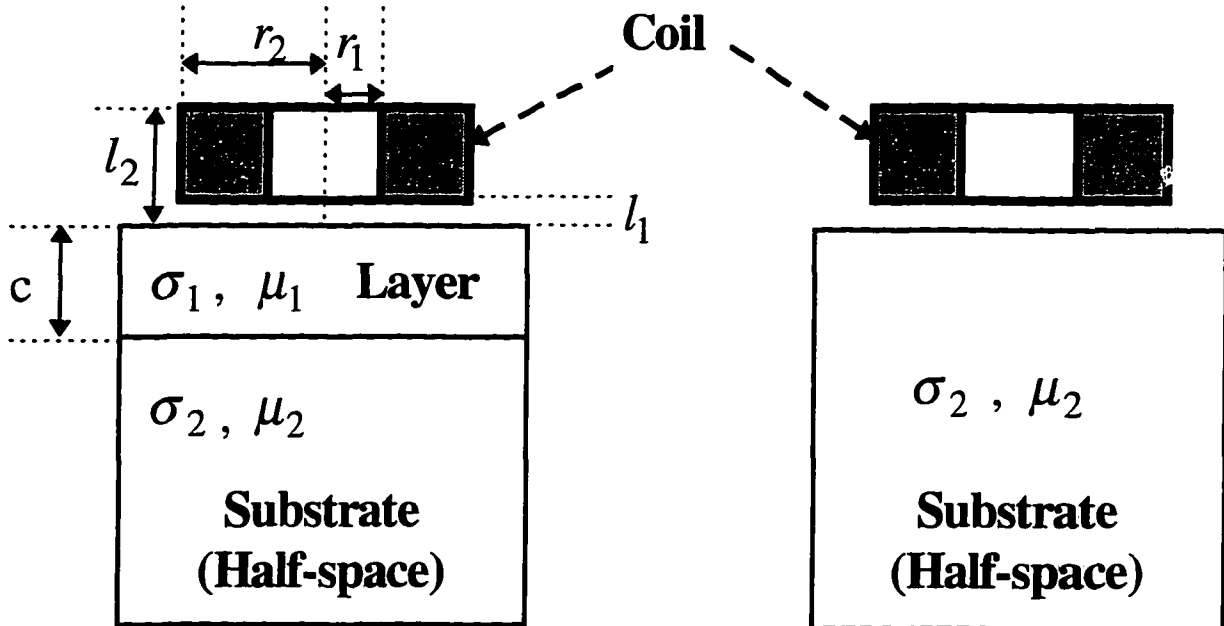


Figure 1. Schematic representation of the model.

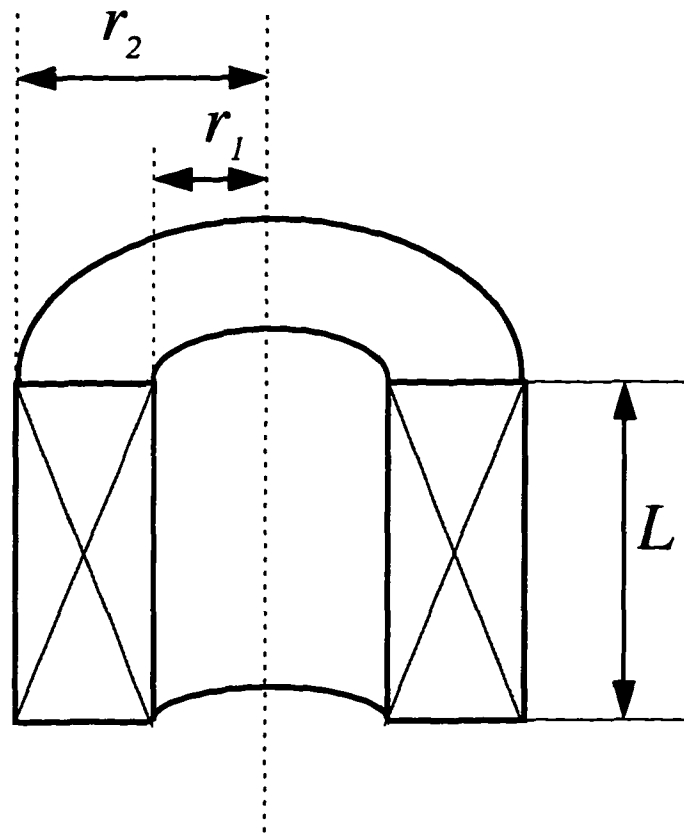


Figure 2. Geometry of the air-core coil used in the experiments.

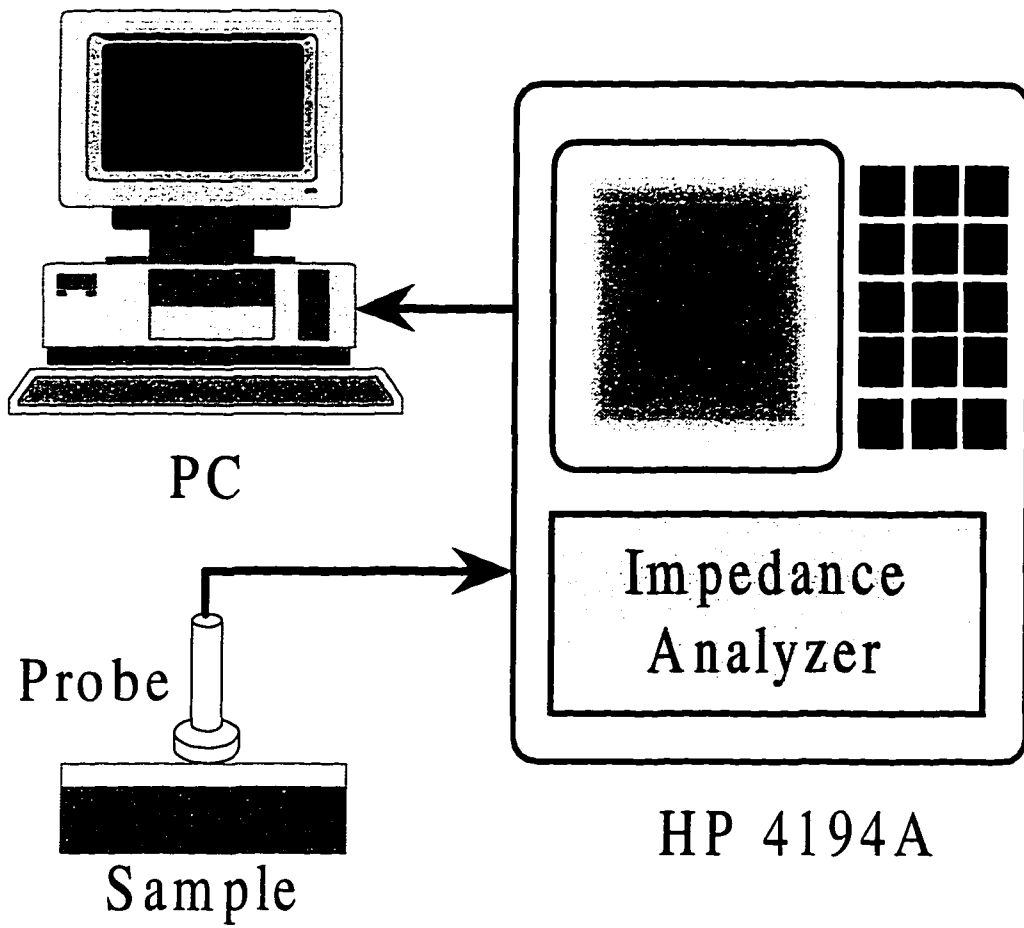


Figure 3(a). Block diagram of the swept-frequency eddy current system used in this work.

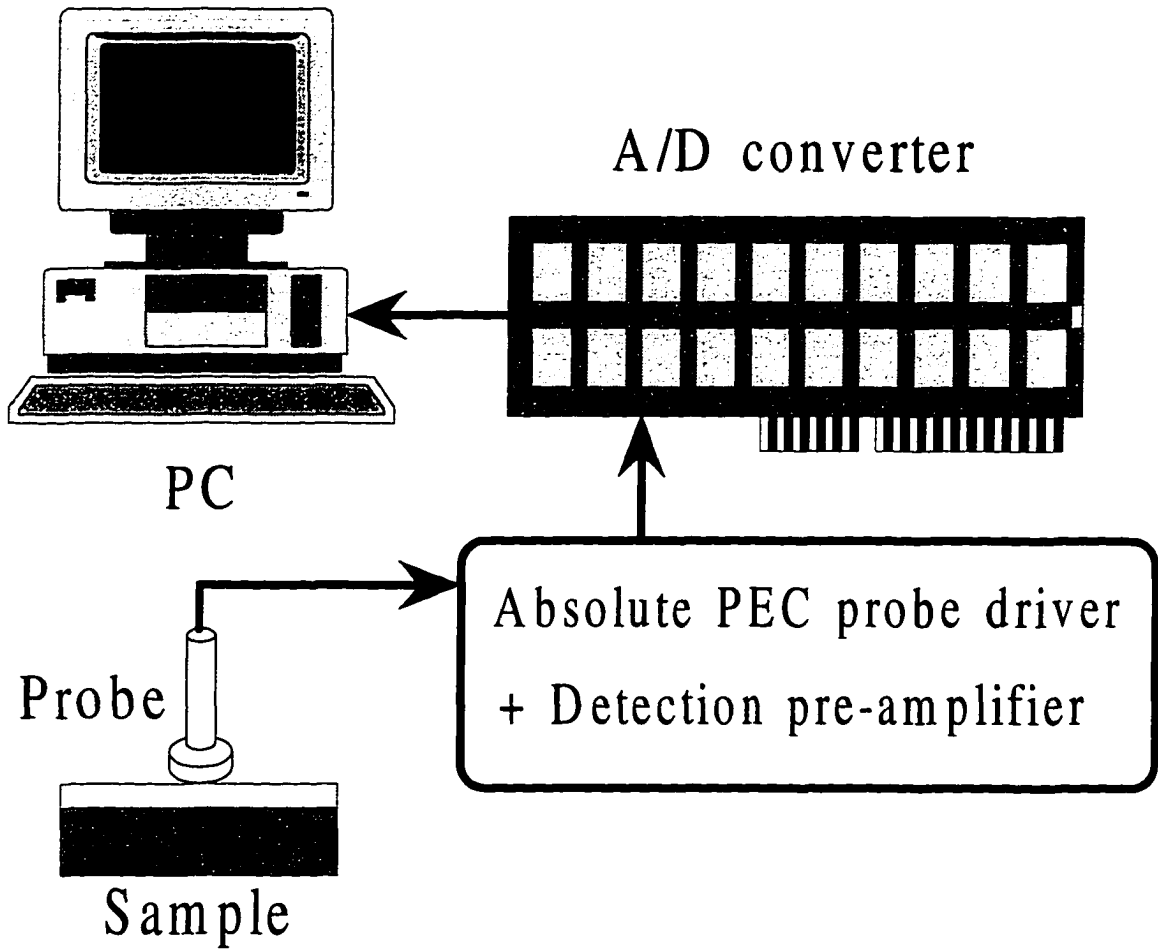
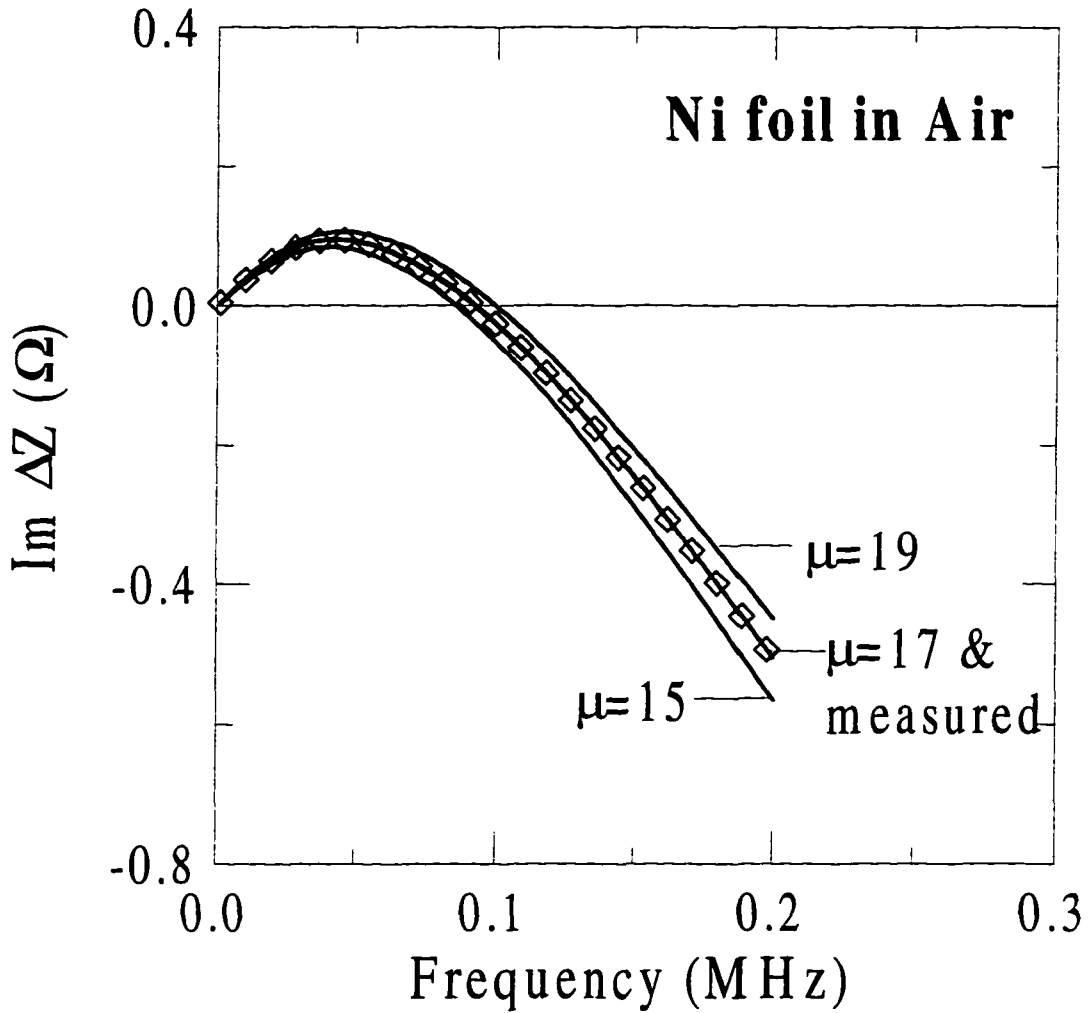
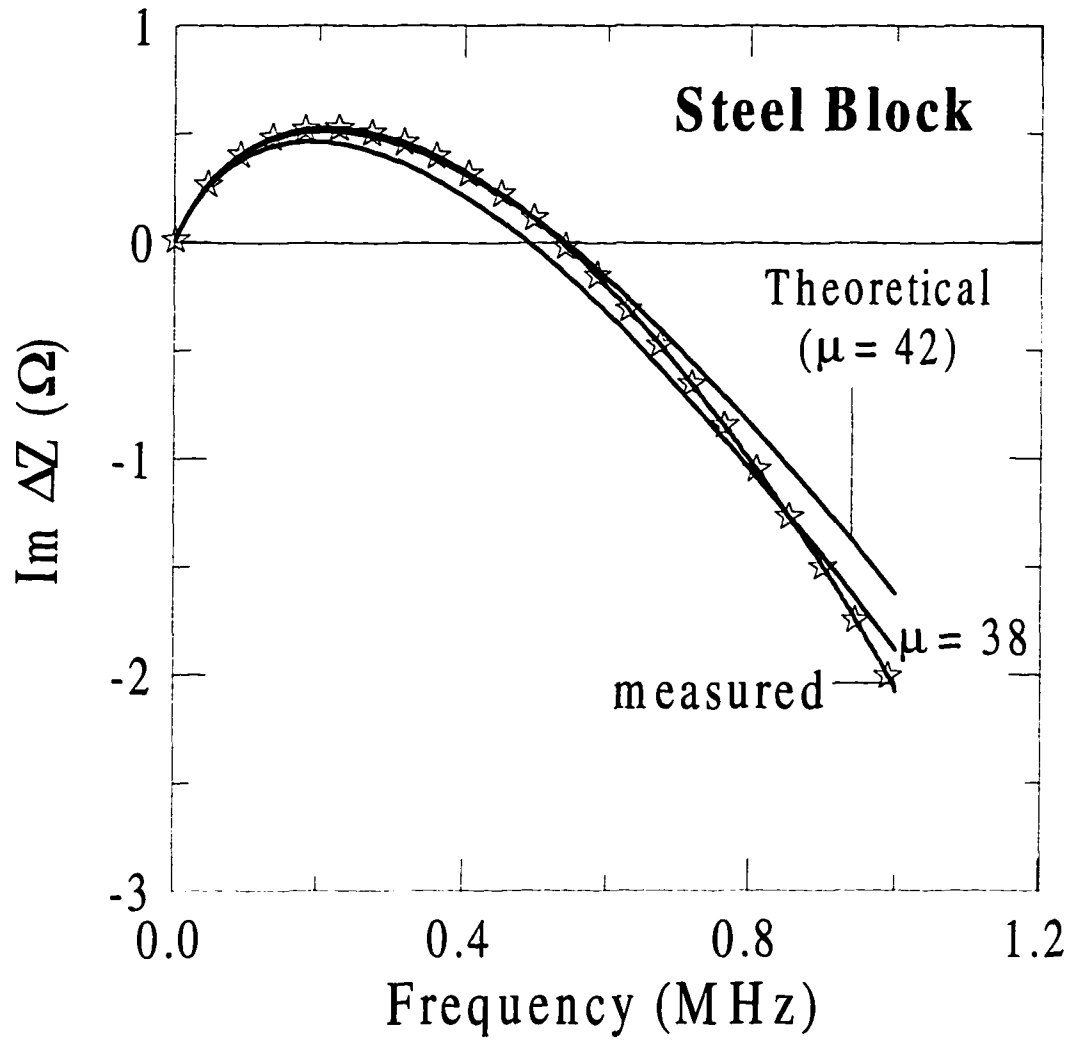


Figure 3(b). Block diagram of the pulsed eddy current instrument used in this work.



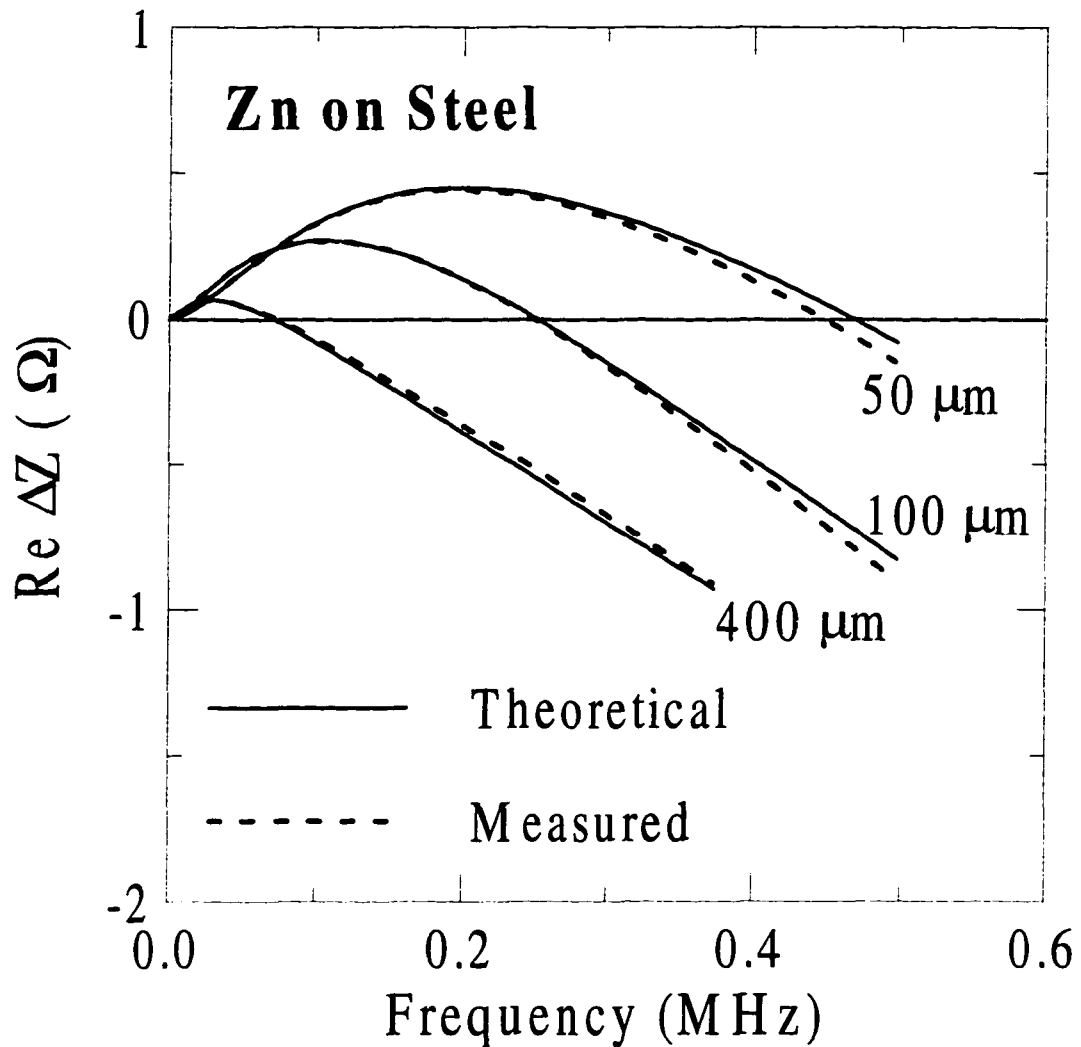
(a)

Figure 4. Determination of permeability of metals. Calculations of the change in the coil impedance when going from metal to air compared to measured values. Theoretical calculations are for different values of initial permeability. Frequency at which impedance crosses zero is proportional to initial permeability.



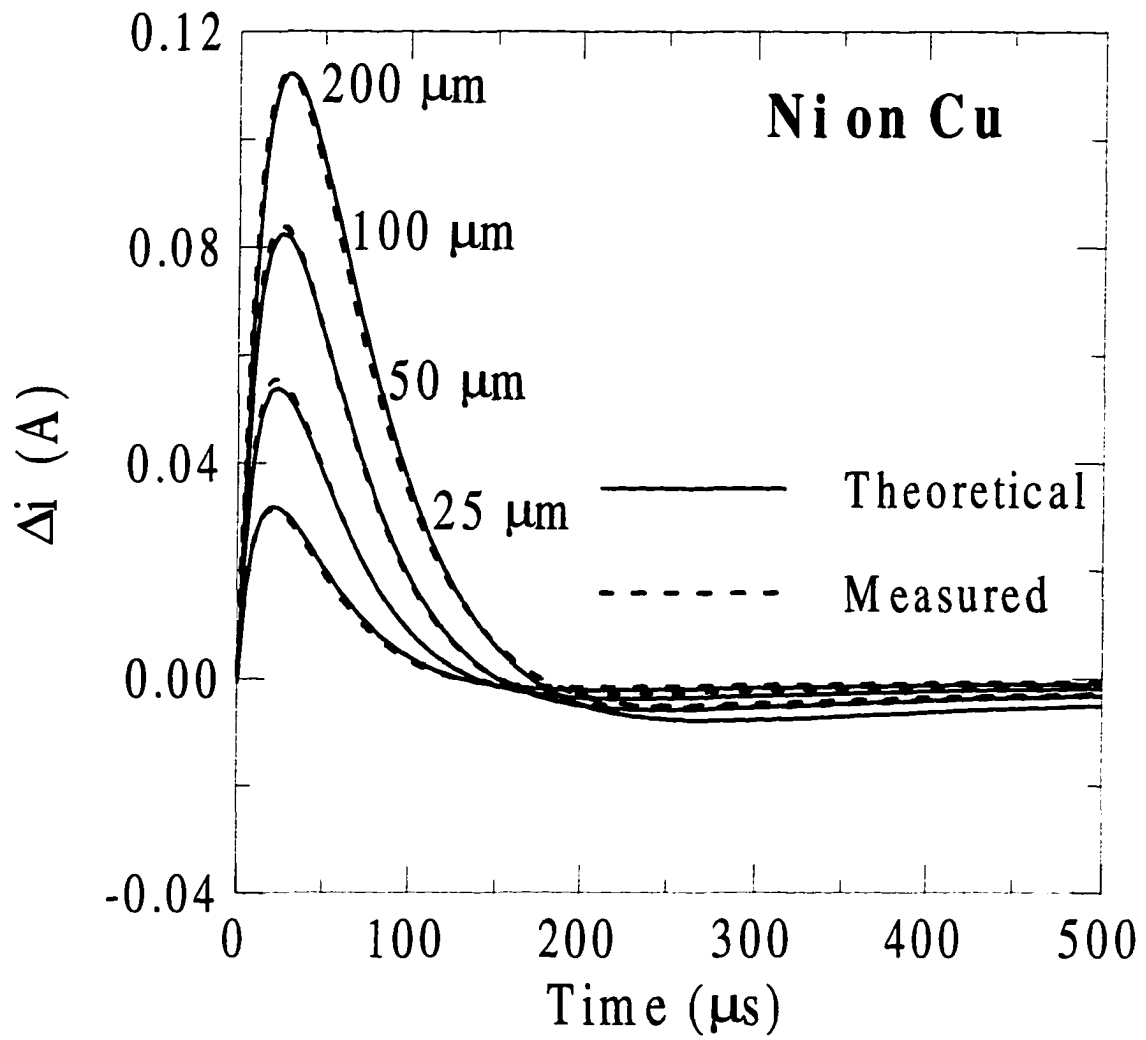
(b)

Figure 4. (Continued)



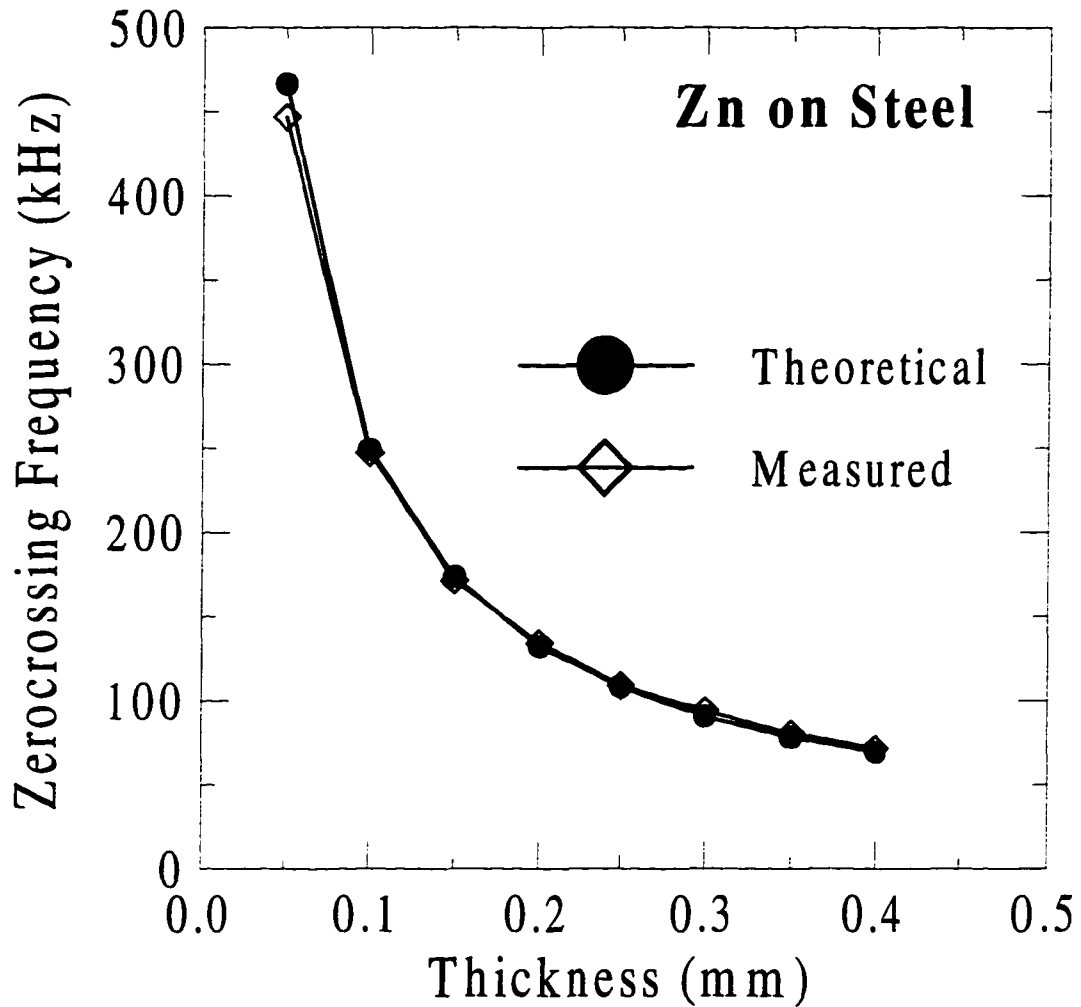
(a)

Figure 5. (a) Comparison of theory and experiment for swept-frequency eddy current measurements of zinc foils of different thickness on a steel alloy substrate. (b) Comparison of theory and experiment for pulsed eddy current measurements of nickel foils of different thickness on a copper substrate. As is evident, the agreement is excellent. No adjustable parameters were used in the theory.



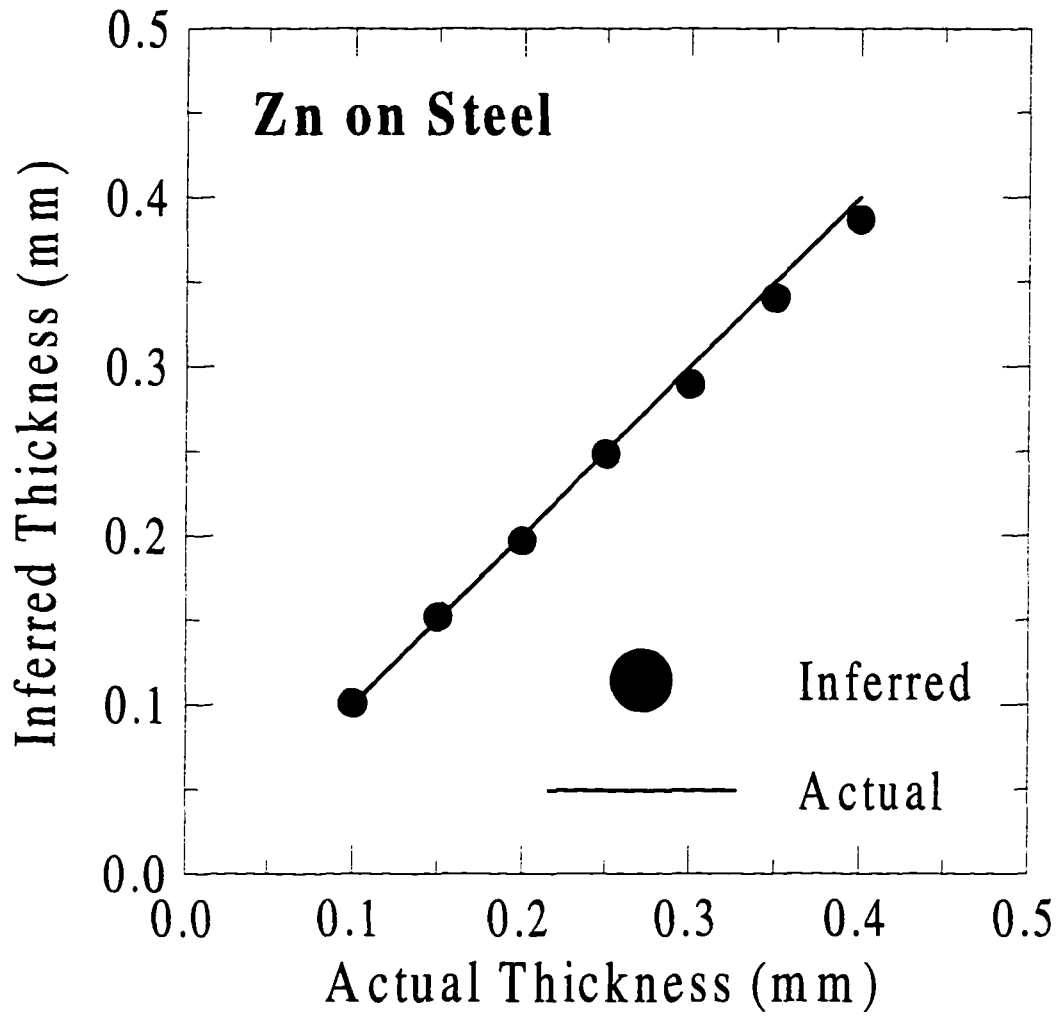
(b)

Figure 5. (Continued)



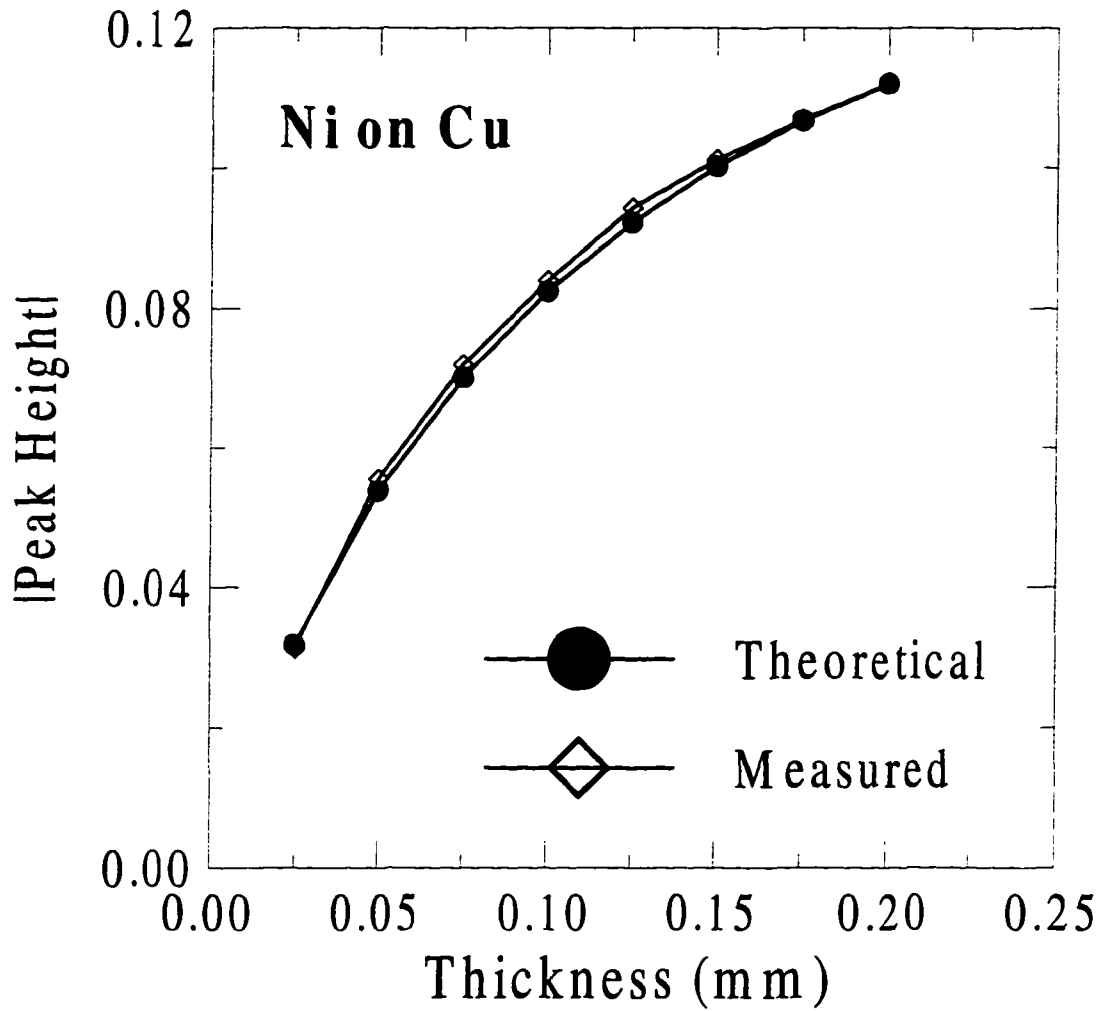
(a)

Figure 6. Coating thickness estimation using swept-frequency eddy currents method. (a) Compares theoretical and measured zero-crossing frequency in the real part of the impedance change. (b) Inferred thickness compared to actual thickness.



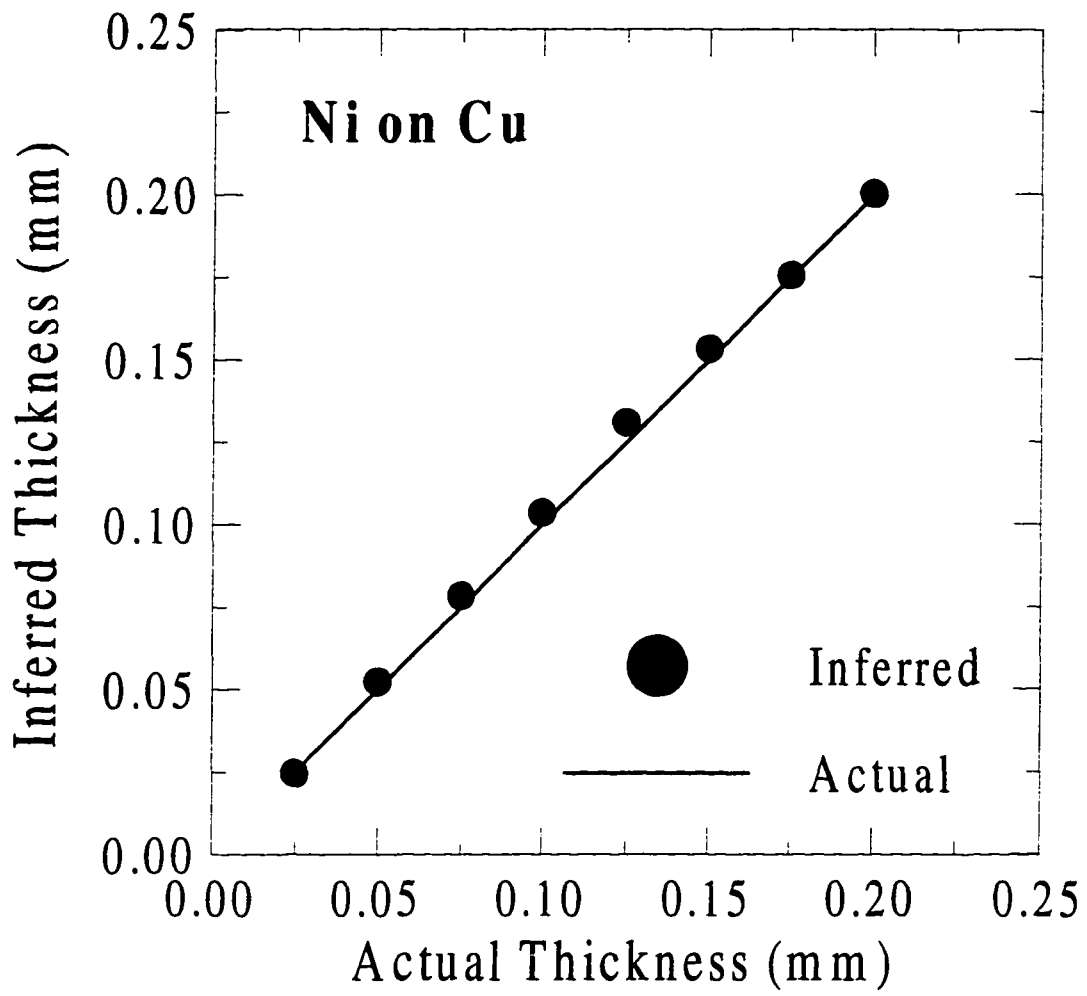
(b)

Figure 6. (Continued)



(a)

Figure 7. Coating thickness estimation using pulsed eddy currents method. (a) Compares theoretical and measured peak-height of the current change. (b) Inferred thickness compared to actual thickness.



(b)

Figure 7. (Continued)

CHAPTER 5.

PHOTOINDUCTIVE IMAGING FOR BOLT HOLE CORNER CRACK INSPECTION

A manuscript to be submitted to the *Journal of NDE*

Cheng-Chi Tai and John C. Moulder

Center for Nondestructive Evaluation

Abstract

Photoinductive (PI) imaging is a novel NDE technique that combines eddy current and laser-based thermal wave methods. It provides an imaging technique with microscopic resolution using eddy-current sensors. We applied this technique to characterize corner cracks on the surface around a bolt hole. Crack images with excellent signal-to-noise-ratios were obtained. The PI signals reflect the geometrical shape of the triangular and rectangular electrical-discharge-machined (EDM) notches that were examined. The results show promise for using this technique to characterize the length, and possibly depth and shape of corner cracks. In this study we present and compare measurement results for 0.25 mm, 0.50 mm, and 0.75 mm rectangular and triangular EDM notches. We also show measurement results for a very small notch (< 0.25 mm) which would be difficult to detect using eddy current techniques. The behavior of PI signals with chopping frequency and eddy current frequency

are compared. To show that the photoinductive imaging technique can be used to image real cracks, we display images of fatigue cracks grown in a specimen of Ti-6Al-4V. Finally, we show eddy current images obtained for a 0.75 mm triangular EDM notch using a rotating bolt hole scanner for comparison with the photoinductive imaging results.

I. Introduction

Crack detection is a critical problem in quantitative nondestructive evaluation (NDE). The ultrasonic method is predominant for detection of subsurface discontinuities, while the eddy current method allows rapid inspection for surface cracks. One main disadvantage of conventional eddy current methods for surface crack detection is the low resolution, due to the interaction between the eddy current probe and the metal under inspection. The photoinductive imaging method is a new NDE technique that combines eddy current and laser-based thermal wave methods. It provides an imaging technique with microscopic resolution using eddy current sensors. We applied this technique to characterize corner cracks at the edge of a bolt hole.

Photoinductive mapping of eddy current fields interacting with cracks is a newly devised technique that is similar to photothermal imaging, but is based on eddy current detection of thermal waves. Thermal waves produce a localized modulation of electrical conductivity in the specimen, which can be detected through its effect on the impedance of a nearby eddy current coil. Moulder, and others¹⁻⁶ showed that this new technique can be used to calibrate and characterize eddy current probes. This calibration method is electro-optical in character; calibration can be accomplished quickly and reliably under computer control. The

method offers a means to determine the electric field intensity of eddy current probes, a quantity that is directly related to their performance for flaw detection and characterization. One promising feature of photoinductive imaging is its potential for high resolution, especially when compared with the resolution possible with eddy current probes alone. Moulder *et al.*⁷⁻⁹ experimentally showed the high resolution capability inherent in this technique by adapting a photoinductive sensor developed for a fiber optic probe to an existing photoacoustic microscope.

Previous research showed that the photoinductive eddy current technique can successfully show the interaction of eddy currents with through-cracks on a gold/chromium film that was evaporated onto a glass substrate.¹⁰ Other studies demonstrated the ability of the technique to image stress corrosion cracks in Inconel tubing. An alternative is to use the same method to characterize cracks on thick metals. Of particular interest is the detection of a corner crack on the surface surrounding a bolt hole, especially the problem of determining the crack's depth.

In this article we describe new experiments designed to apply the photoinductive imaging technique to bolt hole cracks. We show and compare measurement results for 0.25-mm, 0.50-mm, and 0.75-mm rectangular and triangular EDM notches [Table I]. We show that the PI imaging technique can be used to image cracks by displaying images of real fatigue cracks. We show measurement results for a very small notch (< 0.25 mm) [Table I] which would be difficult to detect using conventional eddy current techniques. The behavior of PI signals with variation of chopping frequency and eddy current frequency is described. We show eddy current images of a 0.75 mm triangular EDM notch that were obtained by

using a conventional rotating bolt hole scanner for comparison with the photoinductive imaging results.

The organization of this article is as follows. We introduce the physics of the PI imaging technique in the next section. The PI imaging system is briefly described in Sec. III. In Sec. IV, we present the experimental results using the PI imaging technique and show eddy current imaging results for comparison. We show that the PI technique can reveal information about the depth, length and shape of corner EDM notches. We also discuss the phenomenon of PI imaging in this section. Finally, we give a summary and conclusions in Sec. V.

II. The Photoinductive Effect

The photoinductive imaging method is a technique that combines two NDE modalities: the thermal-wave and eddy current methods. The physics of the technique are thermophysical in nature. Although there are theoretical calculations that predict the PI signal for simple geometry,^{6,12} theoretical predictions for more complex crack shapes are still under development. We introduce the basic phenomenology of the PI technique in this section.

A generic inspection geometry for the PI method is illustrated in Fig. 1. The method works in an exciter-receiver mode; a heat source such as a laser beam is used to excite a specimen thermally, and an EC probe is placed near the excited region to detect the resulting thermal excitation. Let $T(\bar{x})$ denote the temperature distribution in the specimen. The electrical properties such as conductivity σ and permeability μ of the specimen metal are

temperature dependent, and therefore any temperature variation ΔT results in variations of σ and μ via

$$\Delta\sigma = \frac{d\sigma}{dT} \Delta T, \quad \Delta\mu = \frac{d\mu}{dT} \Delta T. \quad (1)$$

An EC probe, on the other hand, is sensitive to the variations $\Delta\sigma$ and $\Delta\mu$ through the usual EC phenomena. Consequently it can detect the thermal fluctuation ΔT through Eq. (1).

In principle, the PI effect can be calculated as follows. A modulated laser beam is focused on the surface of the conductive metal. The resulting temperature fluctuation induces a highly localized change in the conductivity and permeability of the metal, which in turn induces a change in the impedance of the eddy current probe. It can be shown from Auld's reciprocity relation^{6,15} that this impedance change is

$$\Delta Z = -\frac{1}{I^2} \int_V dV \Delta T \left\{ \left(\frac{\partial \sigma}{\partial T} \right) (\bar{E} \cdot \bar{E}') + i\omega \left(\frac{\partial \mu}{\partial T} \right) (\bar{H} \cdot \bar{H}') \right\}, \quad (2)$$

where V is the entire volume of the metal, \bar{E} and \bar{H} are the electric and magnetic field intensities in the metal when laser beam is on, \bar{E}' and \bar{H}' are the electric and magnetic field intensities in the metal when laser beam is off, ω is the angular frequency of eddy currents, ΔT is the ac temperature change in the metal, and σ and μ are the conductivity and permeability of the metal. For practical calculations a perturbation approach may be used to

simplify the calculation. Since the temperature fluctuation induces only a small perturbation to the fields, the perturbed fields can be replaced by the unperturbed fields with good accuracy. For our experiments, a Ti-6Al-4V (nonmagnetic) metal was used so that $d\mu/dT=0$ and the $\bar{H} \cdot \bar{H}'$ term vanishes. In the quasi-static approximation only the tangential components of \bar{E} and \bar{H} contribute to Eq. (2).

The resolution and quality of the PI image are governed by laser beam focusing, chopping frequency and eddy current frequency. The spatial resolution of this technique is governed only by the size of the thermal spot, one of the main advantages of the PI technique over other methods. The image blurring effect is caused by temperature diffusion and laser beam size⁶. The laser-beam size can be reduced mechanically (focusing), while the temperature diffusion effect can be reduced by increasing chopping frequency. The thermal wave is governed by the thermal diffusion equation,¹⁶

$$\nabla^2 T - \alpha \frac{\partial T}{\partial t} = 0, \quad (3)$$

where $\alpha = \lambda / \rho_m C_p$. The temperature distribution extends only over a finite range given by the thermal diffusion length, $\delta_{th} = \sqrt{2\lambda / \rho_m C_p \Omega}$, where Ω is the angular laser chopping frequency, λ is the thermal conductivity, ρ_m is the material density, and C_p is the specific heat of the material. The effect of chopping frequency on the PI signals are shown in Sec. IV.

The reason that the PI imaging technique can be used to map corner cracks is mainly due to the way that eddy currents flow around the crack [Fig. 2]. The induction of eddy currents in the metal is also governed by a diffusion equation,

$$\nabla^2 J = \sigma \mu (\partial J / \partial t). \quad (4)$$

Consider a metal specimen with conductivity σ and permeability μ , in close proximity to an eddy current probe driven with an ac current source operating at the angular frequency ω . Owing to their resistivity, metals are diffusive media for electromagnetic fields, and the penetration of the fields into the metal is given by the skin depth δ_{ec} , where $\delta_{ec} = \sqrt{2 / \mu \sigma \omega}$. The diffusion length of eddy currents, which in some ways is similar to the thermal diffusion length, can dominate the shape in the crack's images, as shown in Sec. IV.

The photoinductive image results from a complex interaction of eddy current skin depth (δ_{ec}) and thermal diffusion length (δ_{th}) effects. We wish to determine the shape of the crack, especially the depth and length. The eddy current skin depth predominantly affects the shape determination. In order to reveal the shape of the crack, the eddy currents must be distributed as uniformly as possible around the crack. We expect that when lower frequency eddy currents are applied, a better image of the crack will be obtained. On the other hand, the main effect of thermal diffusion length is on image resolution and crack depth information. In order to reveal more depth information, the thermal diffusion length should be as long as possible. Nevertheless, longer thermal diffusion length will involve more volume affected by

the thermal energy. This means that the resolution of the image will be reduced when the thermal diffusion length is increased.

We consider the photoinductive phenomena based on the diffusion length effects (δ_{ec} and δ_{th}) and the special scheme used in this article (bolt hole corner crack). Three different cases are discussed, as follows.

1. $\delta_{ec} \gg \delta_{th}$:

When the eddy current skin depth is much greater than the thermal diffusion length, we expect better determination of shape (especially the length) and a higher resolution image. But, due to the smaller thermal diffusion length, the depth information is inferior.

2. $\delta_{ec} \ll \delta_{th}$:

In contrast to the first case, when the eddy current skin depth is much less than the thermal diffusion length, the crack length information is inferior. But more depth information is obtained.

3. $\delta_{ec} \approx \delta_{th}$:

This is the case we used in most of the work in this article. We want the eddy currents to interact with the entire crack and, at the same time, we want the thermal wave to diffuse to the deepest area of the crack.

When we consider the physics of the photoinductive imaging technique, the noise problems that exist in most physical measurements must be taken into account as well. As discussed above, although we can increase the eddy current skin depth to obtain a better

image, the signal level will be reduced at the same time (due to the lower eddy current density). In order to maintain an acceptable signal-to-noise ratio (SNR), there is a lower bound to the eddy current frequency. On the other hand, thermal diffusion length has a similar SNR restriction. We can reduce the thermal diffusion length to obtain a higher resolution image, but the signal level will be reduced when the chopping frequency is increased. The tradeoff between the signal level and image quality must be considered.

Another phenomenon that may have an effect on the photoinductive signal is optical trapping. When the laser beam is right on the EDM slot, part of the light will be trapped inside. The trapped light will heat the walls of the slot more effectively (multiple absorption). In this situation, the energy of the laser beam will be absorbed by the sample with better efficiency. This phenomenon has a greater effect on open slots (EDM notches) than on the cracks (fatigue cracks).

III. Photoinductive Imaging System

The instrument we built to image bolt hole corner cracks using the photoinductive technique is shown in Fig. 3. The PI system comprises a personal computer with a GPIB control board, an eddyscope, two lock-in amplifiers, a laser beam chopper, an argon ion laser, a motion controller for the positioning stage, and the optical subsystem. The computer subsystem controls the operation of the entire instrument: acquiring, analyzing, displaying, and storing the data. The eddyscope detects fluctuations in the impedance of an eddy current probe, and displays them in an impedance plane format (the imaginary component is usually on the vertical axis, and real along the horizontal axis). The laser source is a medium-power

(5 W nominal power), multi-mode argon ion laser. The wavelength of the photon depends on the specific energy level involved, usually it is between 457.9 and 514.5 nm — in the range of green or blue visible light. The laser output is modulated with a chopping wheel.

Ordinarily, we operate the laser at 0.4–1 W power and at 10–100 Hz chopping frequency.

Modulation of the argon laser is required for the signal detection scheme we employ. The lock-in amplifiers use synchronous detection to measure small signals in the presence of noise via the super-heterodyne method, which requires a carrier with amplitude modulation (AM). Although the instrument records all the photoinductive signal components (magnitude and phase), in this article we only present data on the absolute magnitude of the signals.

The specimens used in this research are titanium blocks (Ti-6Al-4V) with 6 mm bolt holes. The specimens contain EDM notches at the edge of the bolt hole [Fig. 4]. The notches are 0.25, 0.50 or 0.75 mm in both length and depth and 0.1 mm in width [Table I]. The shape of the notches are triangular or rectangular as shown in Fig. 4. A specially designed coil probe (inner diameter = 2.54 mm, outer diameter = 4.1 mm, length = 0.76 mm and number of turns = 50) was inserted in the bolt hole with the coil firmly positioned beside the edge of the bolt hole. The probe was operated at a range of frequencies from 100 kHz to 2 MHz.

IV. Results and Discussion

In this section the results of measurements using the photoinductive imaging method are presented and compared. A measurement using a conventional eddy current imaging method is also shown for comparison.

Photoinductive imaging

First we will show PI signals obtained for the EDM notches. The effects of eddy current diffusion length were compared by varying the coil excitation frequency from 100 kHz to 2 MHz. The thermal diffusion length effects were compared by using 10 to 100 Hz chopping frequency. We also compared PI signals for 0.25 mm, 0.50 mm, and 0.75 mm triangular EDM notches. The only data processing method applied to the PI data shown in this article is smoothing. No other artificial means were used to extract the features of the signals (except Fig. 7).

Figure 5 shows the PI surface maps of a 0.25 mm rectangular EDM notch and a 0.50 mm triangular EDM notch. Figure 5(a) is the surface map of a 0.25 mm rectangular EDM notch at 500 kHz eddy current frequency, 40 Hz laser beam chopping frequency, and 1 Watt laser power (See Tables II and III for the eddy current skin depth and the thermal diffusion length). Figure 5(b) is the surface map of a 0.5 mm triangular EDM notch at 1 MHz eddy current frequency, and the same chopping frequency and laser power as in Fig. 5(a). The PI surface maps correspond closely to the shape and length of the notches. They also reveal information about depth. Ordinarily, when eddy currents are distributed uniformly around the corner crack (i.e. $\delta_{ec} \gg$ crack length), cracks with sizes ranging from $1/4 \delta_{ec}$ to $1/2 \delta_{ec}$ can be mapped with good fidelity.

One prominent feature of the PI images is the depth information that is exhibited in the figures (signal strength \propto flaw depth). This phenomenon can be interpreted as follows. When the laser beam is right on the crack, the laser beam will be trapped in the crack. Although it is out of focus, most of the heat of the laser beam will be absorbed by the walls of

the crack. The energy of the laser beam has two ways to go. Either it is reflected into the air or absorbed by the specimen. Since the walls of the crack are surrounded by eddy currents, a greater volume will be affected by the heat. That will generate a stronger signal. A deeper crack has more wall area to absorb the energy. That is why the PI images reveal information on the depth of these cracks. Note that this may not be the case for a tight fatigue crack.

Figure 6 shows the surface map and image of a 0.75 mm rectangular EDM notch. The PI image closely maps the length of this notch, but not its shape. The shape distortion at the end of the crack is due to the limited skin depth of the eddy currents. This PI imaging phenomenon can be interpreted as follows. The eddy currents penetrate into the Ti-6Al-4V sample about 0.91–0.64 mm (δ_{ec} , skin-depth) when the coils are excited at 500 kHz – 2MHz. Lower eddy current densities will induce weaker PI signals. The end of the crack that is nearer the coil has a stronger signal, while the end far from the coil has a weaker signal. Better images can be obtained when the eddy currents are more uniformly distributed across the crack face, as shown in Figs. 5(a) and 5(b).

There is another interesting phenomenon also displayed in the PI images. As shown, the high-resolution capability of the PI imaging method can be verified visibly from the sharp edges in the cracks' images. Figure 7 shows the edges the rectangular notches formed by taking the differential of the PI images. Figure 7(a) shows the edges of a 0.25-mm long and 0.1-mm wide notch. Since the whole crack is surrounded by eddy currents, we can see all the edges around the crack. Figure 7(b) shows the edges of a 0.75-mm long, 0.1-mm wide notch. The side edges are quite obvious, while the edge at the end is ambiguous. That is due to a lower eddy current density at the far end.

To demonstrate the capability of the PI imaging technique, we measured a very small EDM notch which would be hard to detect using conventional eddy current methods. Figure 8 shows the surface and contour maps of a 0.075-mm deep and 0.15-mm long rectangular EDM notch [Table I.]. As shown in Fig. 8(a), the PI method can easily detect this tiny notch. The shape is ambiguous because of the weak signal generated by this very small crack. The diffusion of eddy currents into the material can be easily seen from the profile of the map. There is no doubt that the PI method has the capability to detect cracks that are less than 0.25-mm long.

The effects of eddy current frequency on the PI imaging signals are shown in Figs. 9 and 10. Figure 9(a) shows that better crack images are obtained by reducing the eddy current frequencies. As shown, the shape of the image is distorted at the end of the crack at higher eddy current frequency. Lower frequencies generate more uniform eddy currents around the crack. When the frequencies are in the range from 300 to 500 kHz, good maps of a 0.25-mm long rectangular EDM notch were obtained (see Fig. 5a). As shown in Fig. 9(b), images of the longer cracks (> 0.5 mm) can be improved by using lower frequency ac current to excite the coil. However, the signal amplitude is reduced greatly when lower eddy current frequencies are applied. As can be seen, the signal is almost undetectable when a 100 kHz ac current source was used to excite the coils. There is a trade-off between the image's shape information and signal-to-noise ratio. Figure 10 shows the variation of the peak PI signal (maximum value in a PI image) with eddy current frequency for a 0.75 mm rectangular notch. Higher eddy current frequencies give larger signals, although the signals approach saturation when the frequency is higher than 1 MHz. Usually frequencies between 200 kHz and 1 MHz

were used to excite the coil. Higher eddy current frequencies generate a stronger signal, but smaller diffusion length. Lower eddy current frequencies have a weaker signal, but greater diffusion length. For smaller cracks (length < 0.5 mm) in this titanium alloy, we found an eddy current frequency of 300–500 kHz to be best for imaging the cracks we studied.

Figure 11 shows how resolution varies with laser chopping frequency for transverse scans across a 0.25 mm long and 0.1 mm wide notch (scan direction perpendicular to notch axis). The spatial resolution of PI images depends on the focal spot of the laser beam and the thermal diffusion length. The focusing can be improved optically ($\sim 50 \mu\text{m}$ for the laser source used in this article), while the thermal diffusion length can be reduced by applying higher chopping frequency. Reducing the thermal diffusion length means a smaller volume of metal is affected by the heat from the laser. That will generate a higher spatial resolution image. As shown in Fig. 11, when higher chopping frequencies were applied, sharper edges were obtained. Although higher chopping frequencies increase the resolution of the image, they also reduce the signal's level (from 10 mV @ 10 Hz to 0.1 mV @ 100 Hz) at the same time. To maintain an acceptable signal level and image resolution we found the best results were obtained with a chopping frequency of approximately 40 Hz.

Figure 12 shows the variation in the peak PI signal (maximum value in a PI image) with chopping frequency. The signal's level drops exponentially as chopping frequency is increased. The signal drops very quickly when the chopping frequency increases from 10 to 50 Hz. It then decays more slowly from 50 to 100 Hz. The signal is almost undetectable when the chopping frequency is raised to 150 Hz. Ordinarily, 20–100 Hz chopping frequencies were used, although we avoided 60 Hz.

Figure 13 shows a comparison of PI signals for three different length triangular EDM notches. The signals correlate with the notches' depth and length quantitatively. Notice that the only processing applied to the data shown in this figure is smoothing. We could improve the images' quality by background removal (normalization).

To show that the photoinductive imaging technique is also effective for fatigue cracks, we used this method to image a real fatigue crack grown at the edge of a bolt hole [Fig. 14]. This fatigue crack was produced using 35.6 kN load centered over the hole and cycled in three-point bending. After cycling the hole for 20,000 cycles, one crack 2.46-mm long was detected. As shown in Fig. 15, the PI images clearly reveal this tight crack that is almost invisible to the naked eye. Figure 16 shows the contour and surface maps of another, smaller fatigue crack.

Eddy current imaging

To compare the results of photoinductive imaging with conventional eddy current methods, we made measurements on the same samples using traditional eddy current imaging methods¹⁷. We used a differential probe that has two oppositely phased coils mounted very close to each other. The rotating EC probe scans across the crack repeatedly as it is driven into the bolt hole. A big signal upset occurs when the probe crosses the edge of the bolt hole. The most dominant features of the signals from the differential eddy current probe are the positive and negative peaks associated with the flaw.

Figure 17 shows images obtained from a 0.75-mm triangular EDM notch using the rotating bolt hole scanner. Figure 17(a) shows the imaginary component of the eddy current

signals after smoothing. Figure 17(b) and 17(c) show the real and imaginary components of the eddy current signals after background removal. The negative and positive peaks of the signals are characteristic signals due to the differential eddy current probe passing over the crack. Figure 17(d) shows the magnitude of the eddy current signal after processing. EC signals have a much stronger signal level than the PI signals, but the EC signals are much more strongly affected by the geometric discontinuity at the edge than is the case for the PI method. Thus, conventional eddy current methods may not detect very small edge cracks due to obscuration from the edge signal. The PI method is able to detect signals from the smallest defects at the edge.

V. Summary and Conclusions

This article has described a practical approach for using the photoinductive imaging method to map corner cracks in bolt holes. The initial results clearly demonstrate that this technique can be used to detect and to image corner cracks in a bolt hole. We examined a variety of EDM notches in Ti-6Al-4V that were triangular or rectangular in shape, with lengths between 0.15 mm and 0.75 mm. The PI imaging method proved capable of mapping the length and shape of EDM notches — when the length of the notch is in the range between $1/4 \delta_{ec}$ and $1/2 \delta_{ec}$. It also provides qualitative information about crack depth. Due to the eddy currents' limited penetration into the metal, the corner-crack's PI image is distorted when the length of crack is longer than $1/2 \delta_{ec}$. The PI technique can detect very tiny cracks less than 0.25-mm long, which are hard to detect using conventional eddy current techniques.

PI imaging is a high resolution technique. The resolution and quality of the images are governed by the eddy current frequency, laser beam chopping frequency and focusing. We showed that better images can be obtained by reducing the eddy current frequency. The relation between PI signal amplitude and eddy current frequency were determined. We showed that the resolution of the PI images can be improved by increasing the laser beam chopping frequency. We also showed the relation between PI signal amplitude and chopping frequencies.

When compared to traditional eddy current methods, the photoinductive method has much better SNR and higher resolution and so does not need signal processing to extract the signal's features as is required for ordinary eddy current methods. It may also yield more information about the critical features of the crack — the shape, length, and depth. The fact that the PI method can reveal information about the depth of EDM notches is due to the interaction between the specimen and the laser beam. More energy of the laser is absorbed by the sample when the laser is directed into the slot. Deeper slots have more area to absorb the energy, and will therefore generate a stronger signal.

It has been shown that the photoinductive imaging technique is capable of detecting real fatigue cracks at the edge of a bolt hole. Two real fatigue cracks were imaged, both are tight cracks and are invisible to the unaided eye. The photoinductive imaging technique was able to clearly delineate the surface length of the cracks. However, interpreting the depth of these real cracks will require further study.

Acknowledgments

This work was supported by the NSF Industry/University Center for NDE at Iowa State University. The authors gratefully acknowledge the contribution of Mr. Tauquir A. Khan in making measurements using the conventional eddy current imaging method. We would like to thank Dr. J. Chao of the Pratt & Whitney Company for providing several of the samples. We are also grateful to Mr. Brian F. Larson for preparing the fatigue crack samples. We are especially grateful to Dr. James H. Rose for first suggesting this study to the authors and for his helpful suggestions during the course of the investigation.

References

- [1] K. No, J. C. Moulder, D. O. Thompson, and J. F. McClelland, "Detection of Thermal-Waves in Metals by Eddy Current Probes — A New Approach for Nondestructive Evaluation (NDE)", Presented at the 5th International Topical Meeting on Photoacoustic and Photothermal Phenomena, Heidelberg, F.R.G., July 27-30, (1987).
- [2] J. C. Moulder, N. Nakagawa, K. S. No, Y. P. Lee, and J. F. McClelland, "Photoinductive Imaging: A New NDE Technique", in Review of Progress in Quantitative NDE, Vol. 8A, edited by D. O. Thompson and D. E. Chimenti, p. 599. Plenum, New York (1989).
- [3] M. W. Kubovich, J. C. Moulder, M. S. Hughes, B. A. Auld , "A Self-Calibrating Eddyscope", in Review of Progress in Quantitative NDE, Vol. 10A, edited by D. O. Thompson and D. E. Chimenti, p. 2243. Plenum, New York (1991).
- [4] M. S. Hughes, J. C. Moulder, M. W. Kubovich, B. A. Auld , "Mapping Eddy Current Probe Fields using the Photoinductive Effect", in Review of Progress in Quantitative NDE, Vol. 10A, edited by D. O. Thompson and D. E. Chimenti, p. 905. Plenum, New York (1991).
- [5] J. C. Moulder and N. Nakagawa, "Characterizing the Performance of Eddy Current Probes Using Photoinductive Field-Mapping", in Res. Nondestr. Eval, 4:221–236, Springer-Verlag New York Inc. (1992).

- [6] N. Nakagawa and J. C. Moulder. "Eddy Current Probe Calibration via the Photoinductive Effect", in *Review of Progress in Quantitative NDE*, Vol. 13A, edited by D. O. Thompson and D. E. Chimenti, p. 295. Plenum, New York (1994).
- [7] J. C. Moulder, M. W. Kubovich, J. M. Mann, M. S. Hughes, and N. Nakagawa. "Applications of Photoinductive Imaging", in *Review of Progress in Quantitative NDE*, Vol. 9A, edited by D. O. Thompson and D. E. Chimenti, p. 533. Plenum, New York (1990).
- [8] J. C. Moulder, D. N. Rose, D. C. Bryk, and J. S. Siwicki, "NDE Application of High-Resolution Photoinductive Imaging", *Springer Series in Optical Sciences*, Vol. 62, *Photoacoustic and Photothermal Phenomena II*, © Springer-Verlag Berlin, Heidelberg (1990).
- [9] J. C. Moulder, D. N. Rose, D. C. Bryk, and J. S. Siwicki, "High-Resolution Thermal-Wave Imaging Using the Photoinductive Effect", in *Review of Progress in Quantitative NDE*, Vol. 9A, edited by D. O. Thompson and D. E. Chimenti, p. 539. Plenum, New York (1990).
- [10] J. C. Moulder, and A. Degeratu, unpublished work, 1992.
- [11] J. C. Moulder, and W. Junker, unpublished work, 1991.
- [12] N. Nakagawa, "Theoretical Study of Photoinductive Inspection", in *Review of Progress in Quantitative NDE*, Vol. 10A, edited by D. O. Thompson and D. E. Chimenti, p. 1081. Plenum, New York (1991).
- [13] N. Nakagawa, S. Mitra and J. C. Moulder, "Eddy Current Corner Crack Inspection", in *Review of Progress in Quantitative NDE*, Vol. 11A, edited by D. O. Thompson and D. E. Chimenti, p. 233. Plenum, New York (1992).
- [14] N. Nakagawa and J. C. Moulder, "A Model of Bolt Hole Inspection via Eddy Current", in *Review of Progress in Quantitative NDE*, Vol. 12A, edited by D. O. Thompson and D. E. Chimenti, p. 259. Plenum, New York (1993).
- [15] B. A. Auld. In *Eddy-Current Characterization of Materials and Structures*, ASTM STP 722, edited by G. Birnbaum and G. Free, p. 332. American Society for Testing and Materials, Philadelphia (1981).
- [16] H. S. Carslaw and J. C. Jaeger, "Conduction of Heat in Solids", 2nd edition, Oxford University Press, 1959.
- [17] Naveen Bohra, "A Novel Inspection System for Aircraft Engine Turbine Disks" (Master thesis, Iowa State University, 1996).

Table I. Bolt hole corner notch standard.

Type	Depth (mm)	Length (mm)
Rectangular	0.25	0.25
Rectangular	0.50	0.75
Rectangular	0.75	0.75
Triangular	0.25	0.25
Triangular	0.50	0.75
Triangular	0.75	0.75
Rectangular	0.075	0.15

Table II. Eddy current skin depth in the Ti-6Al-4V.

Frequency (kHz)	Skin Depth (mm)
200	1.437
300	1.174
400	1.016
500	0.909
1000	0.643
2000	0.455

Table III. Thermal diffusion length in the Ti-6Al-4V.

Chopping Frequency (Hz)	Diffusion Length (mm)
10	1.36
20	0.96
30	0.79
40	0.68
50	0.61
100	0.43

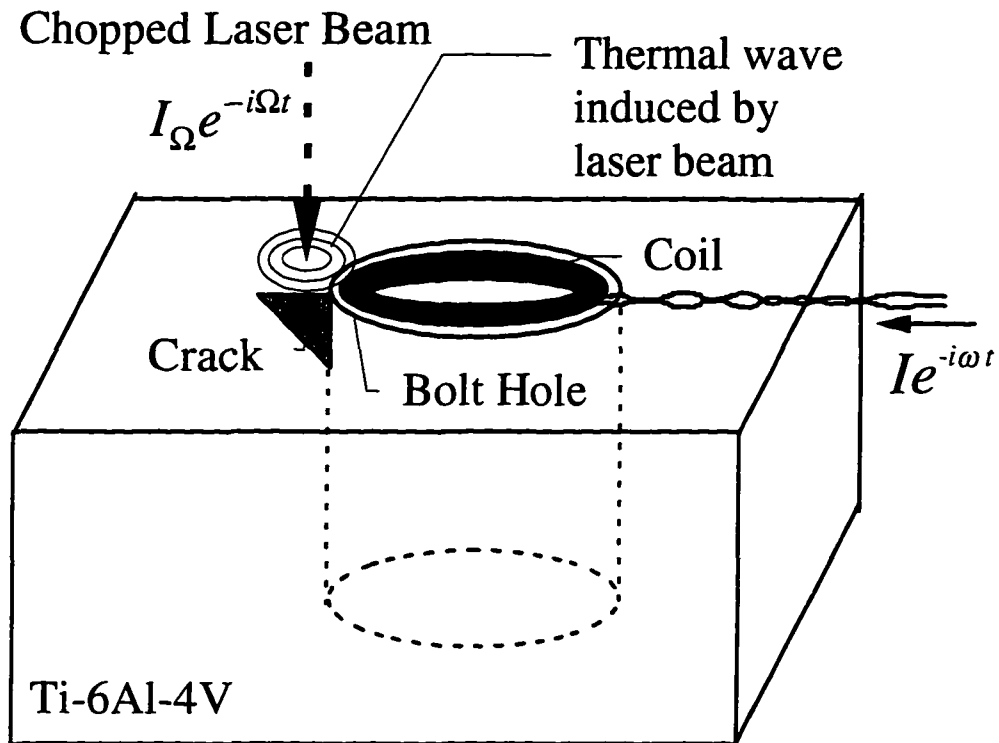


Figure 1. Generic photoinductive inspection geometry. A laser beam is used to excite the specimen thermally, and an EC probe is used to detect the resulting thermal excitation.

Eddy Current Flow

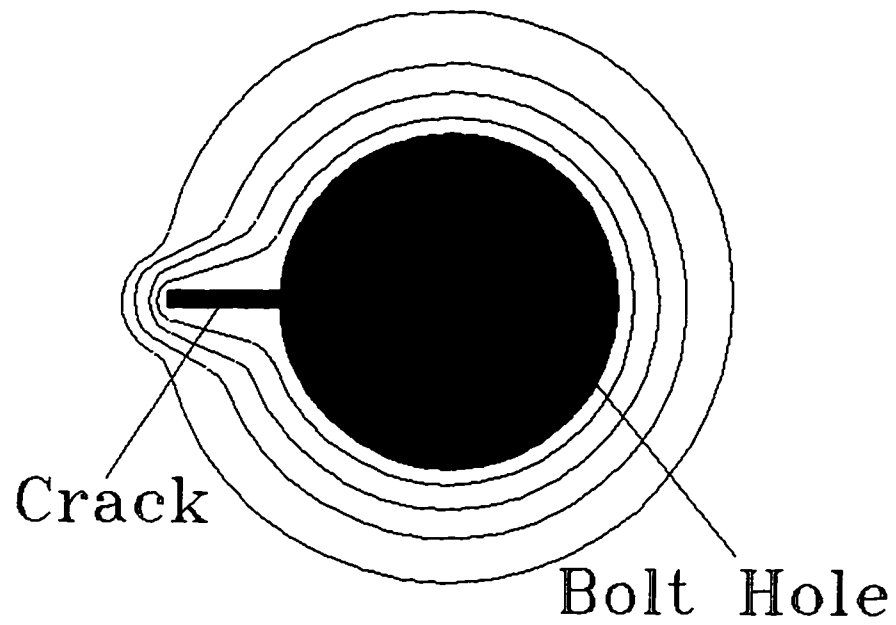


Figure 2. Eddy current flow around a bolt hole with a corner crack (top view).

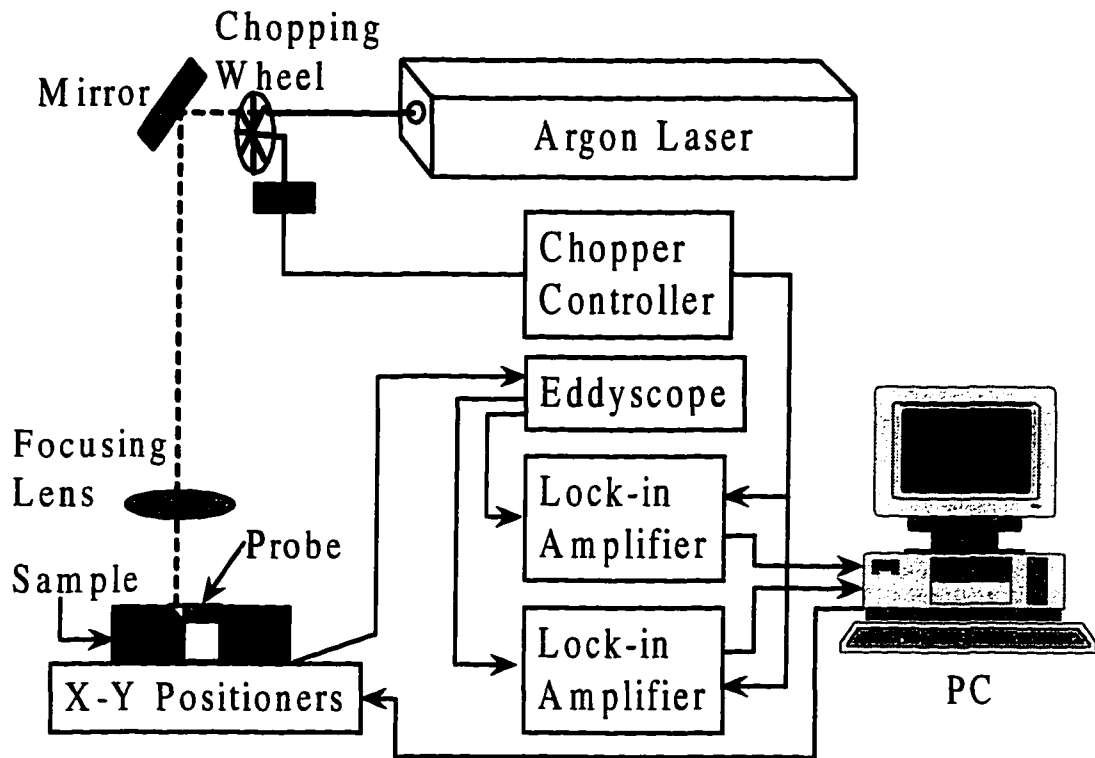


Figure 3. Photoinductive imaging system.

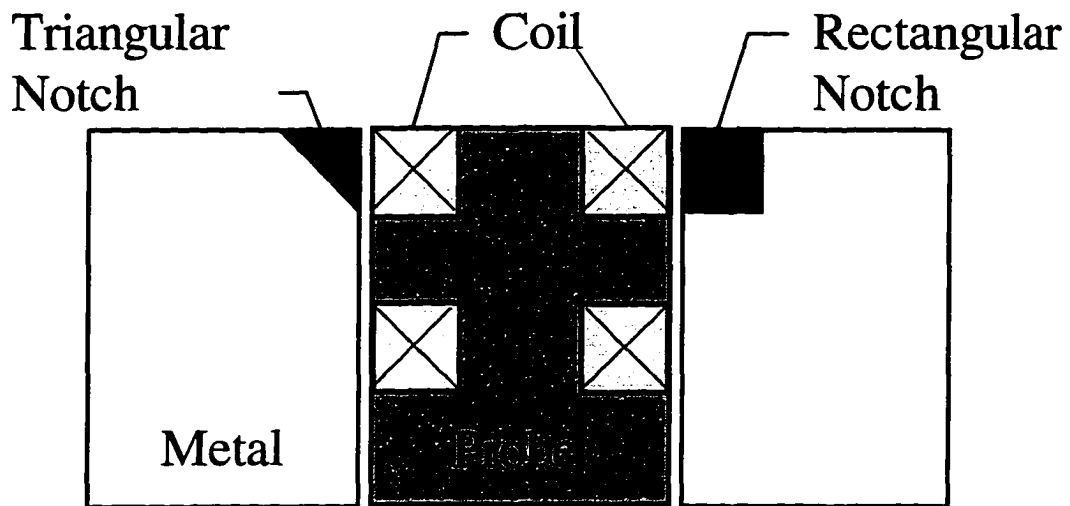
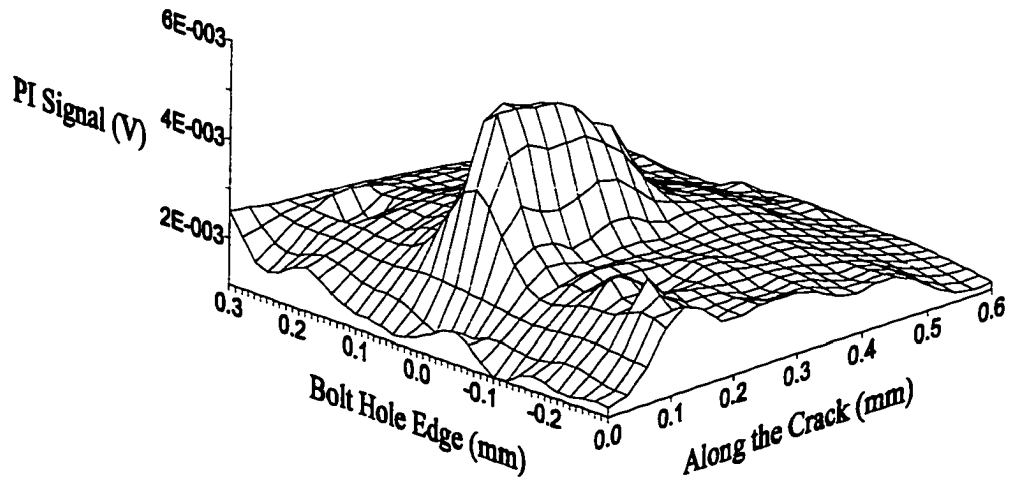
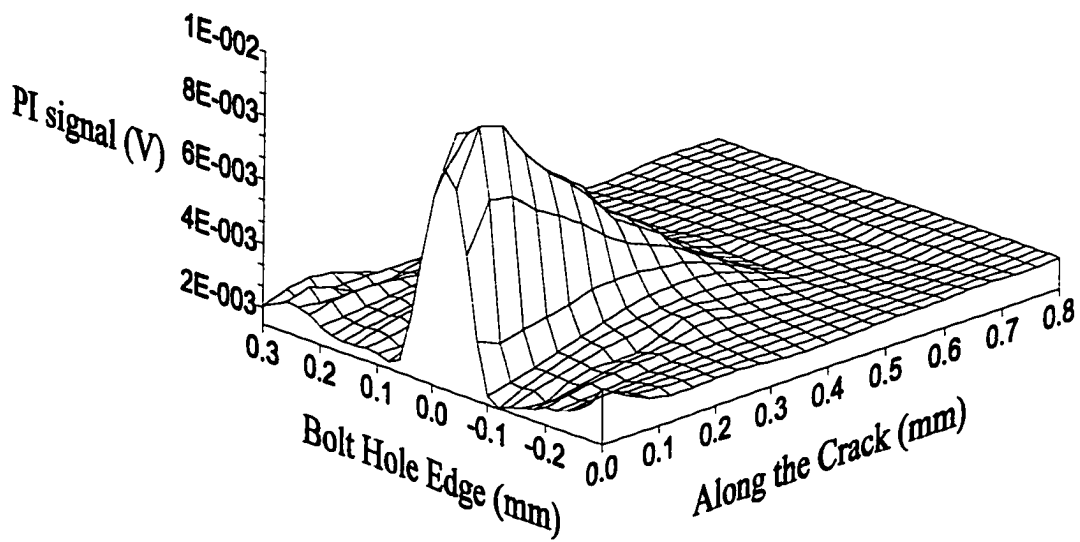


Figure 4. Probe and bolt hole corner cracks (triangular and rectangular EDM notches). The differential probe is used to detect the variation of inductance due to the incident thermal wave. Notches were 0.25–0.75 mm in depth and length, 0.1 mm in width.

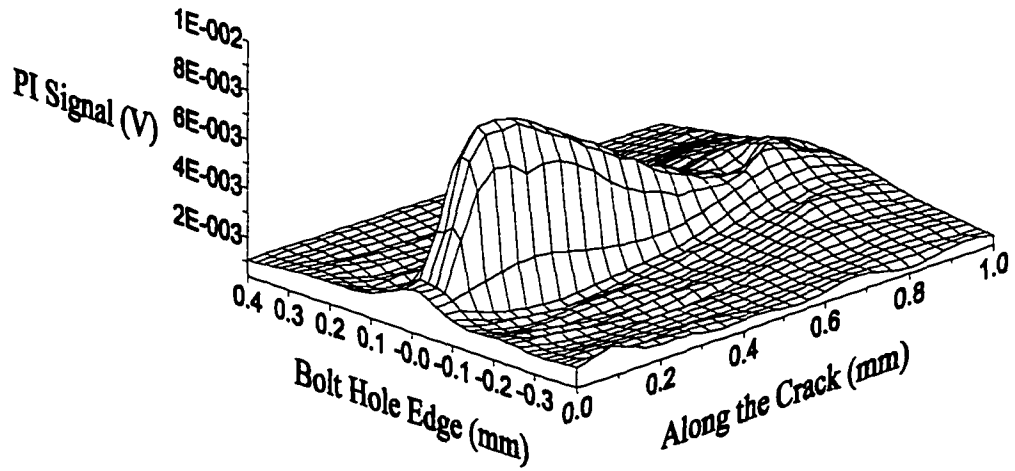


(a)

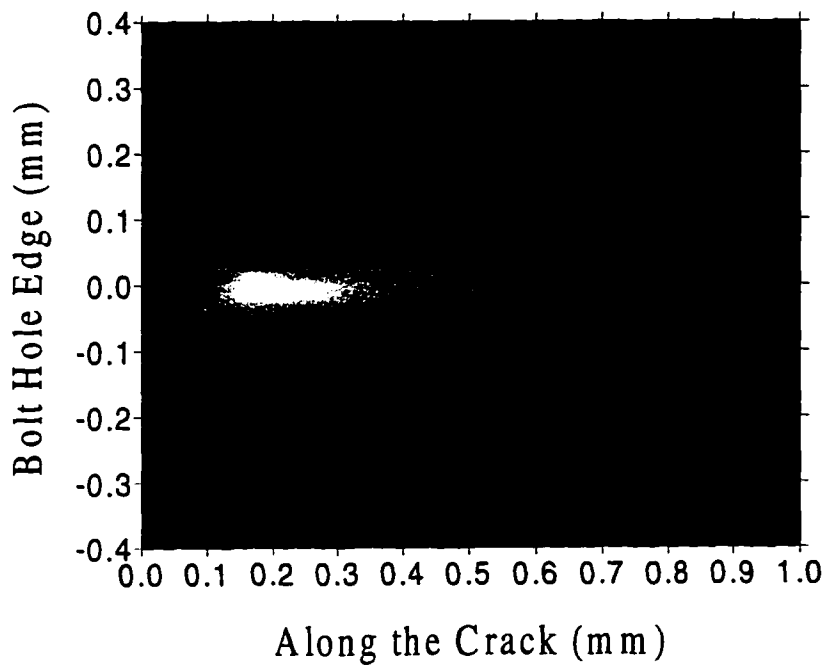


(b)

Figure 5. Photoinductive images for (a) 0.25-mm rectangular, and (b) 0.50-mm triangular EDM notches. (Eddy current frequency, 500 kHz for 5(a) and 1 MHz for 5(b); laser power, 1 W; chopping frequency, 40 Hz.)



(a)



(b)

Figure 6. Shows (a) the surface map, and (b) the image of a 0.75-mm rectangular EDM notch. (Eddy-current frequency, 500 kHz; laser power, 1 W; chopping frequency, 40 Hz.)

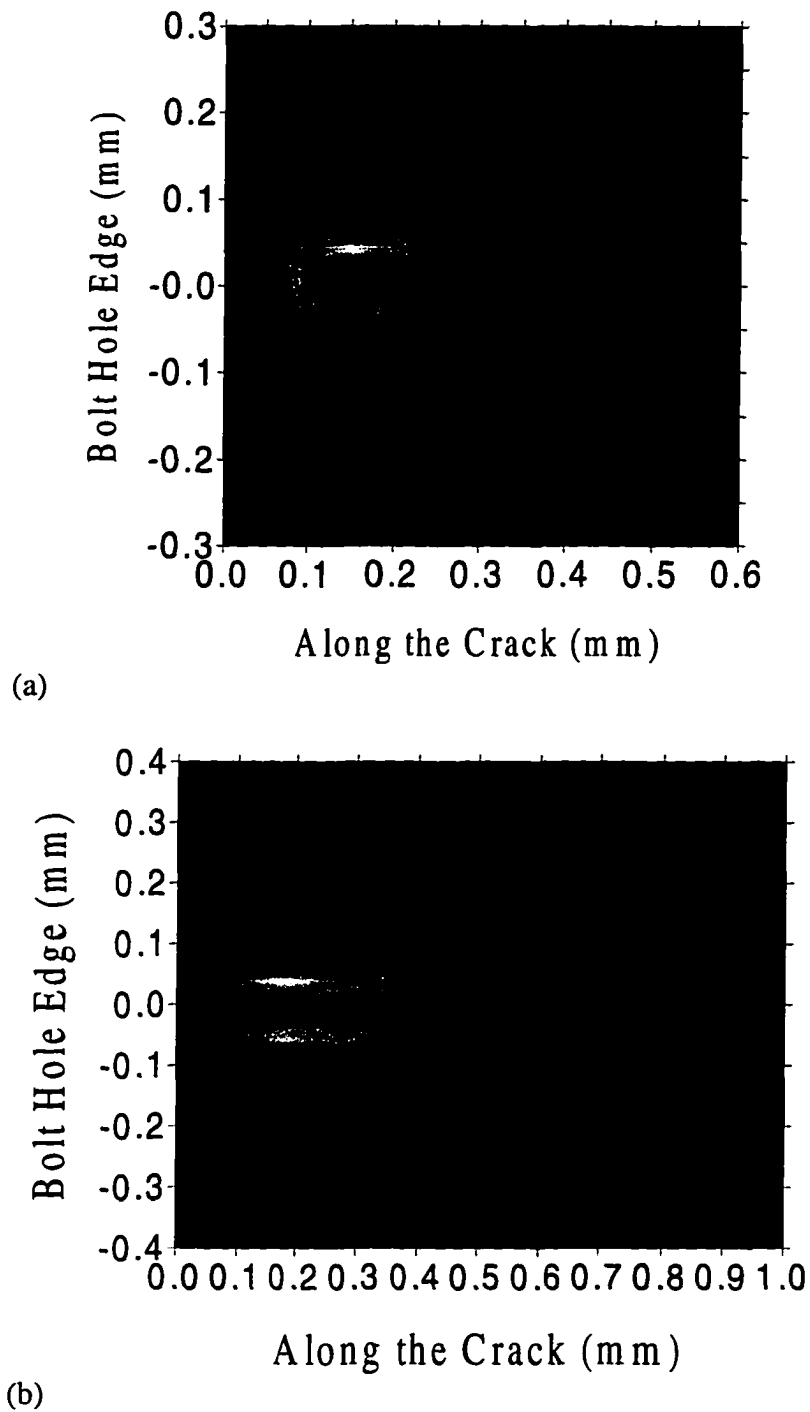
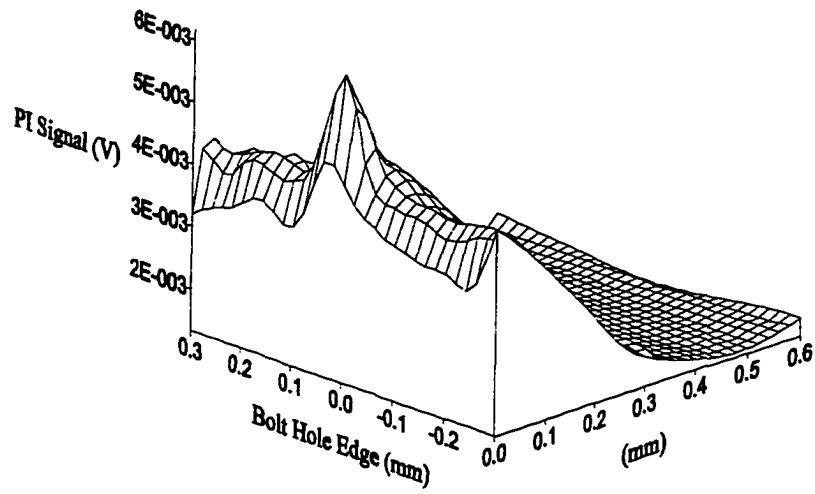
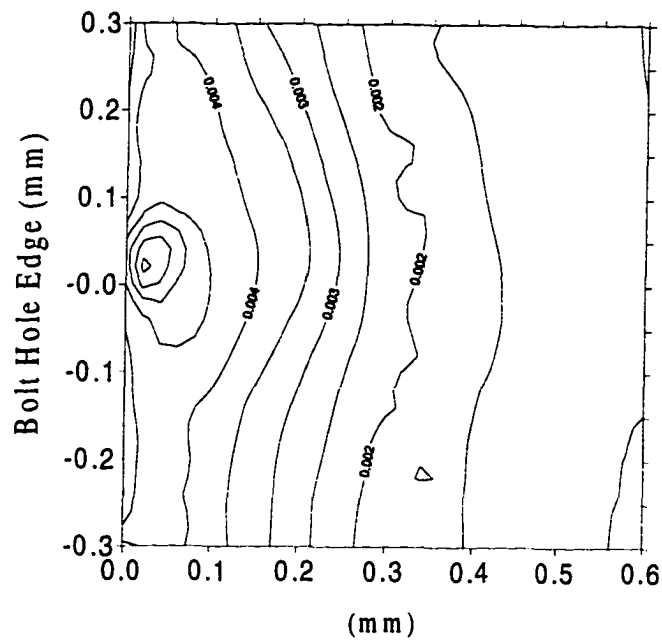


Figure 7. Edges of the cracks. (a) Edges of a 0.25-mm long and 0.1-mm wide rectangular EDM notch, (b) edges of a 0.75-mm long and 0.1-mm wide rectangular EDM notch. These images were formed by spatial differentiation of the original PI images.

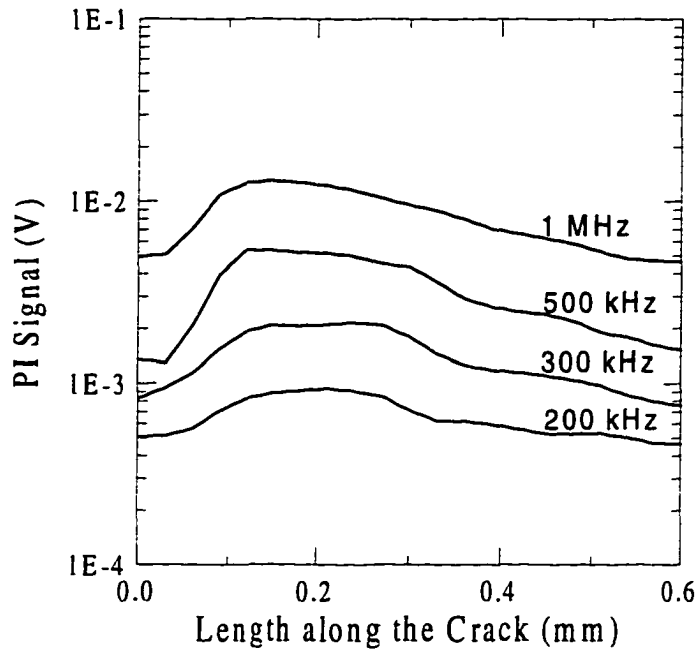


(a)

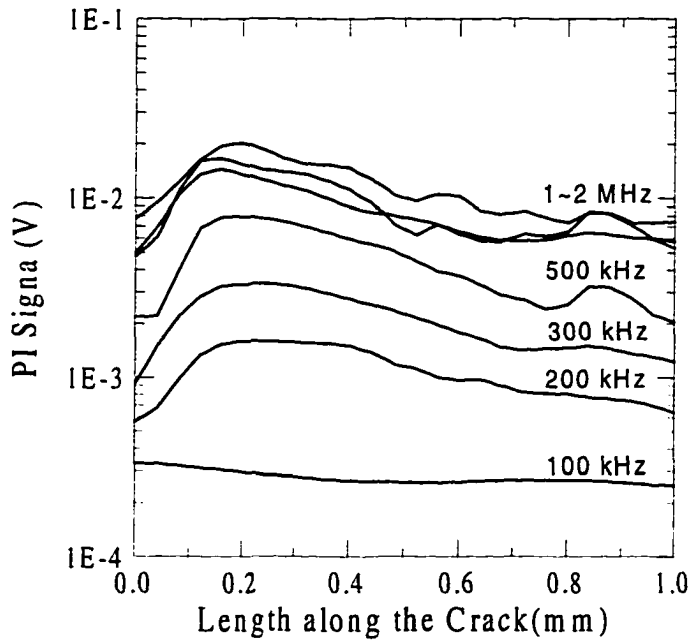


(b)

Figure 8. Shows the surface and contour maps of a 0.075-mm deep and 0.15-mm long rectangular EDM notch. (Eddy-current frequency, 1 MHz; laser power, 1 W; chopping frequency, 40 Hz.)



(a)



(b)

Figure 9. Photoinductive crack profiles at different eddy current frequencies. (a) 0.25-mm rectangular notch, (b) 0.75-mm rectangular notch. (Laser power: 1 W; chopping frequency: 40 Hz.)

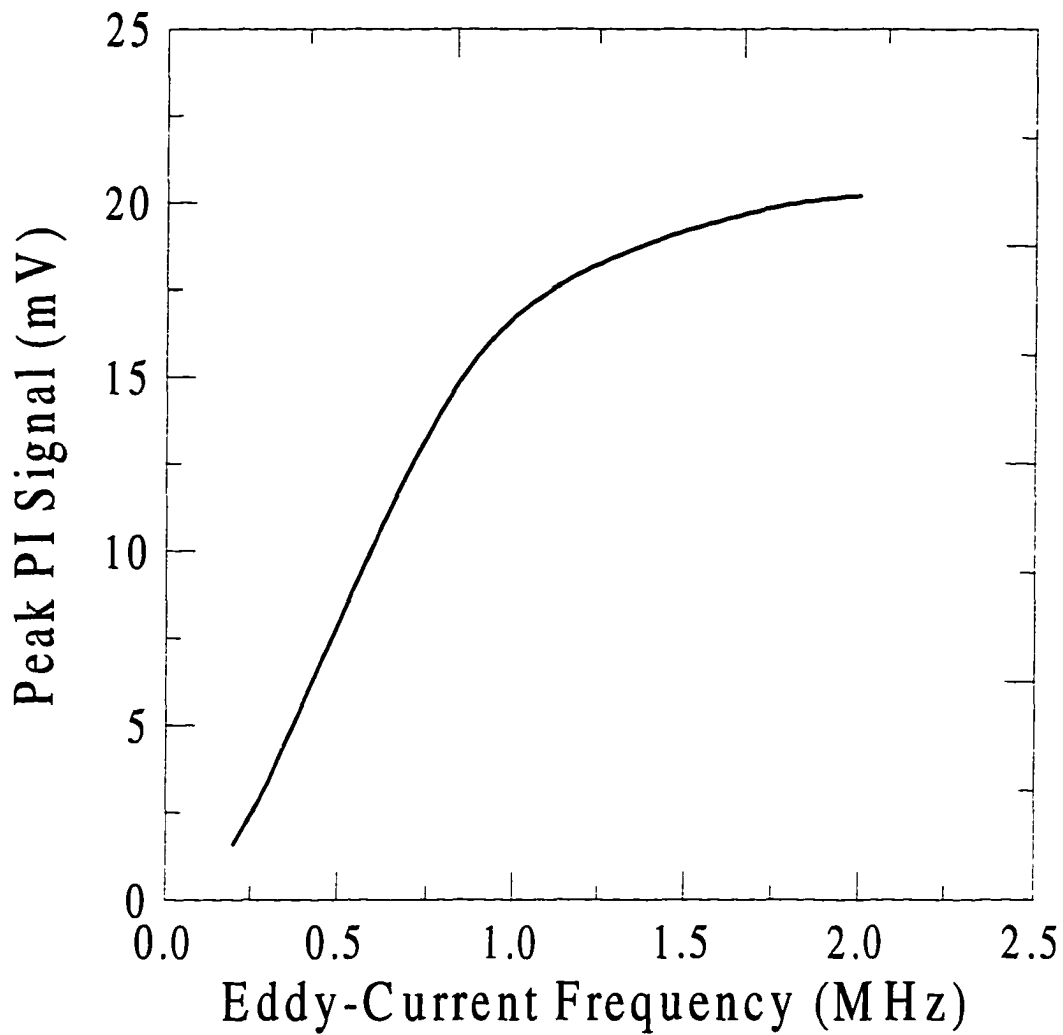


Figure 10. PI signal vs. eddy current frequency. (Laser power, 1W; chopping frequency, 40 Hz; 0.75 mm rectangular notch.)

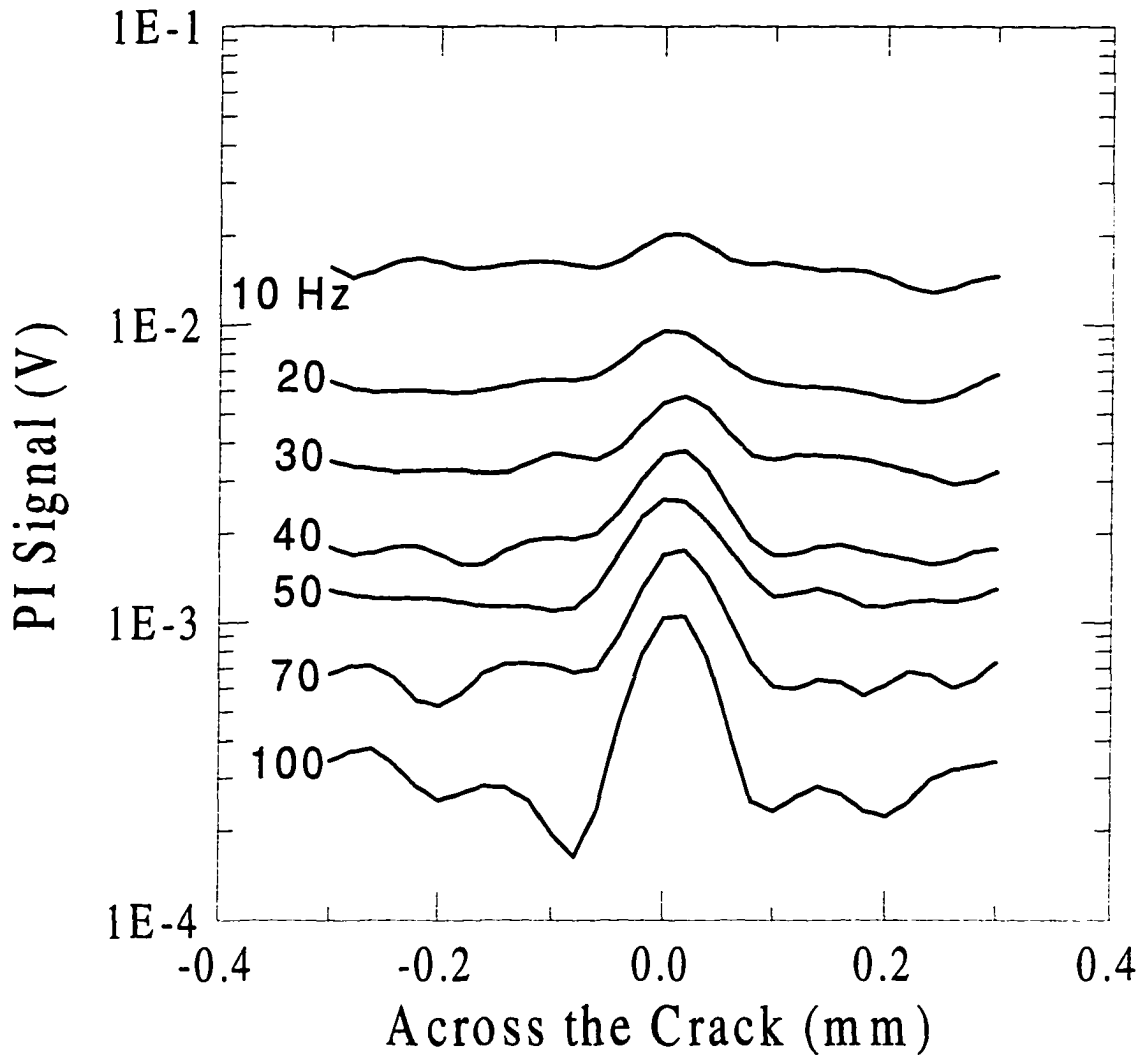


Figure 11. Resolution vs. laser chopping frequency. (Eddy-current frequency, 400 kHz, laser power, 1 W; 0.25 mm rectangular notch.)

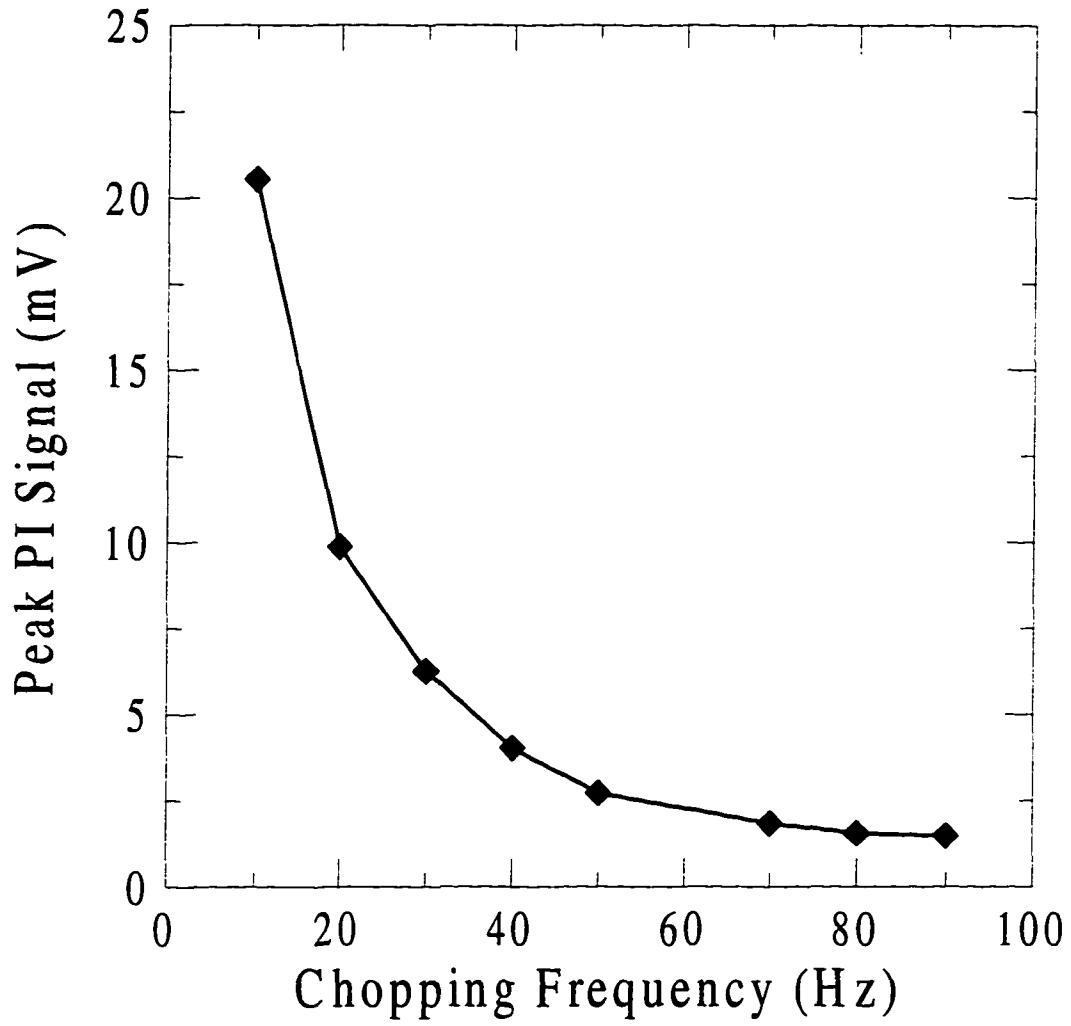


Figure 12. Peak PI signal level vs. laser chopping frequency. (Eddy-current frequency, 400 kHz; laser power, 1 W.)

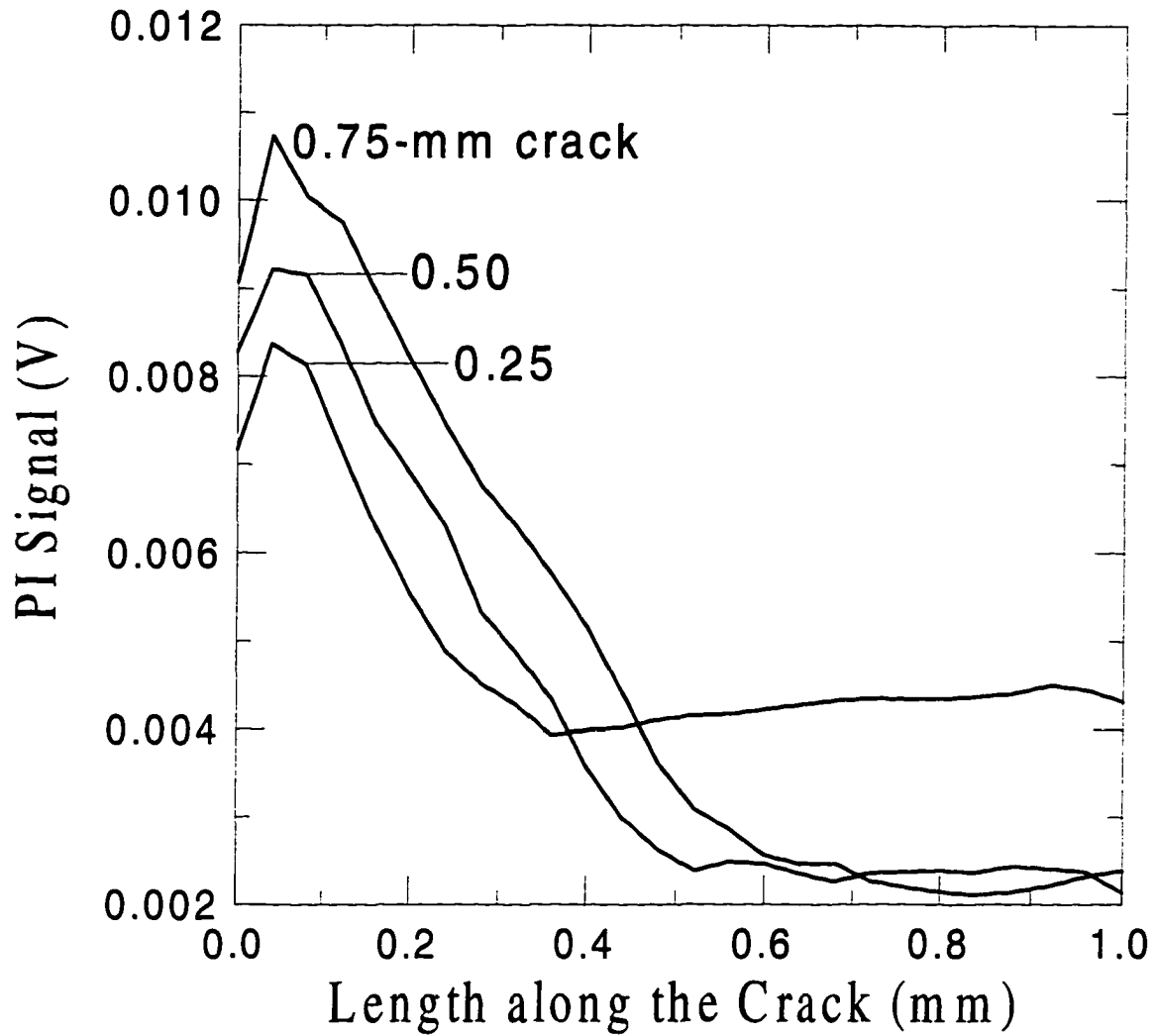


Figure 13. Variation of PI signals with the length and depth of EDM notches. (Eddy-current frequency, 1 MHz; laser power, 1 W; chopping frequency, 40 Hz.)

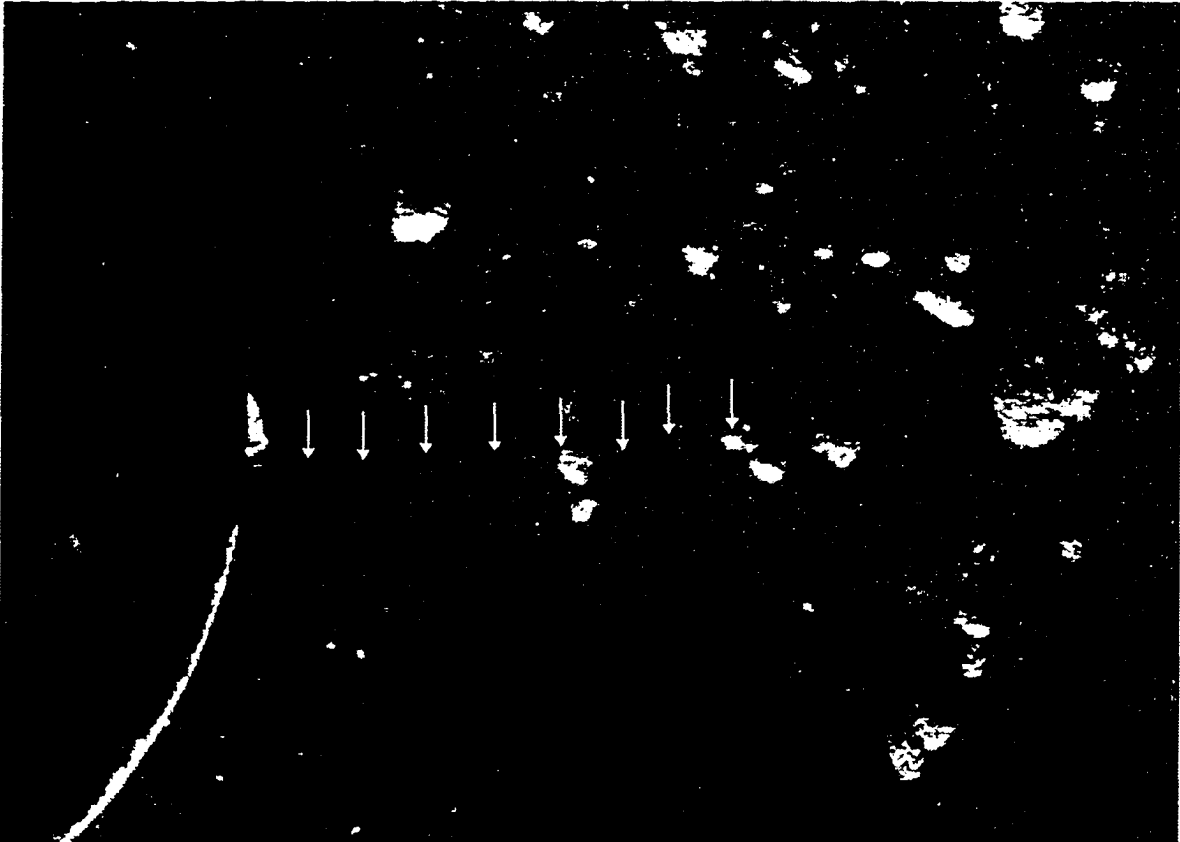


Figure 14. Shows the microscopic photograph of a real fatigue corner crack initiated from the bolt hole edge. (Diameter of the bolt hole = 6 mm; crack length \approx 2.46 mm.)

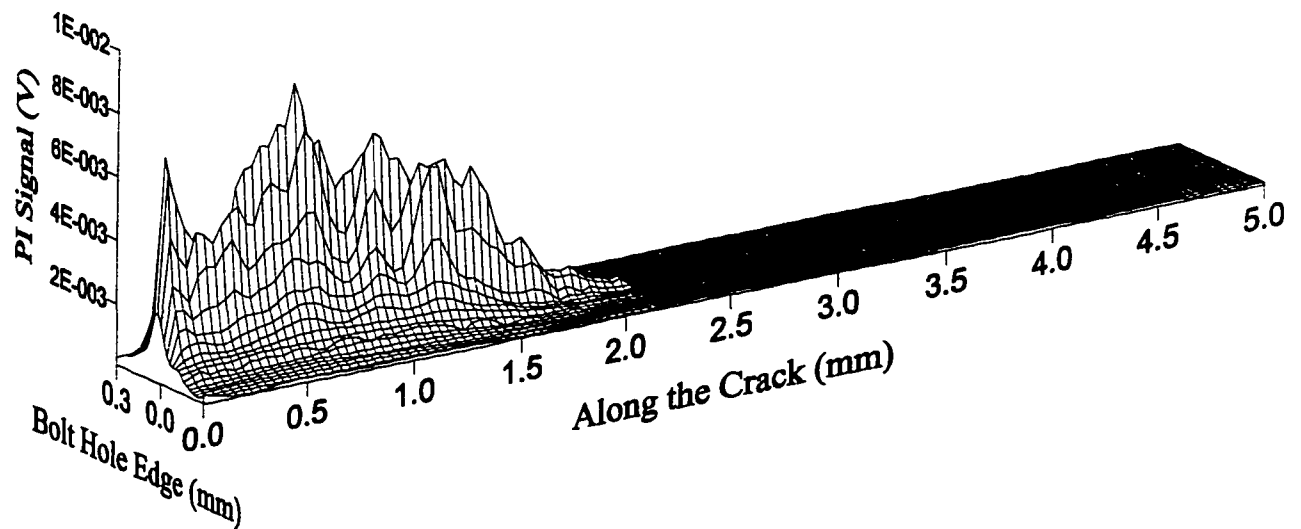
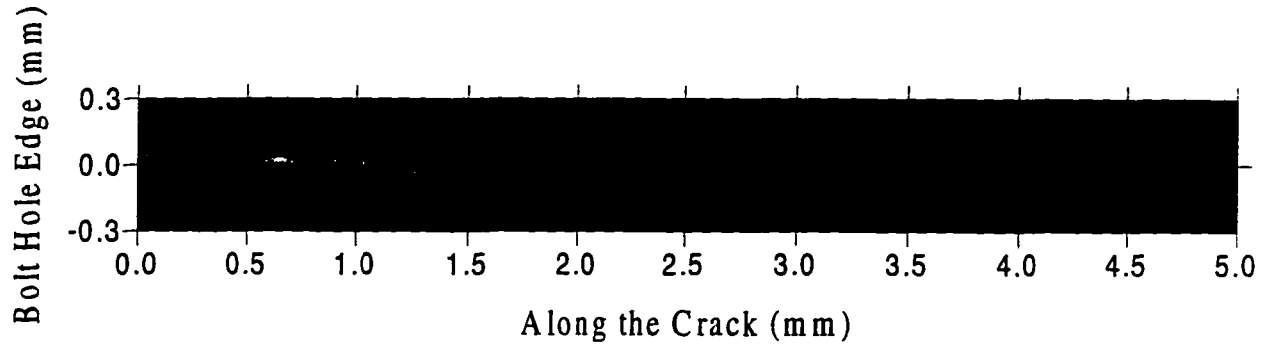


Figure 15. Shows the photoinductive image and surface maps of the real fatigue crack shown in Fig 14. (Eddy-current frequency, 200 kHz; laser power, 0.4 W; chopping frequency, 40 Hz.)

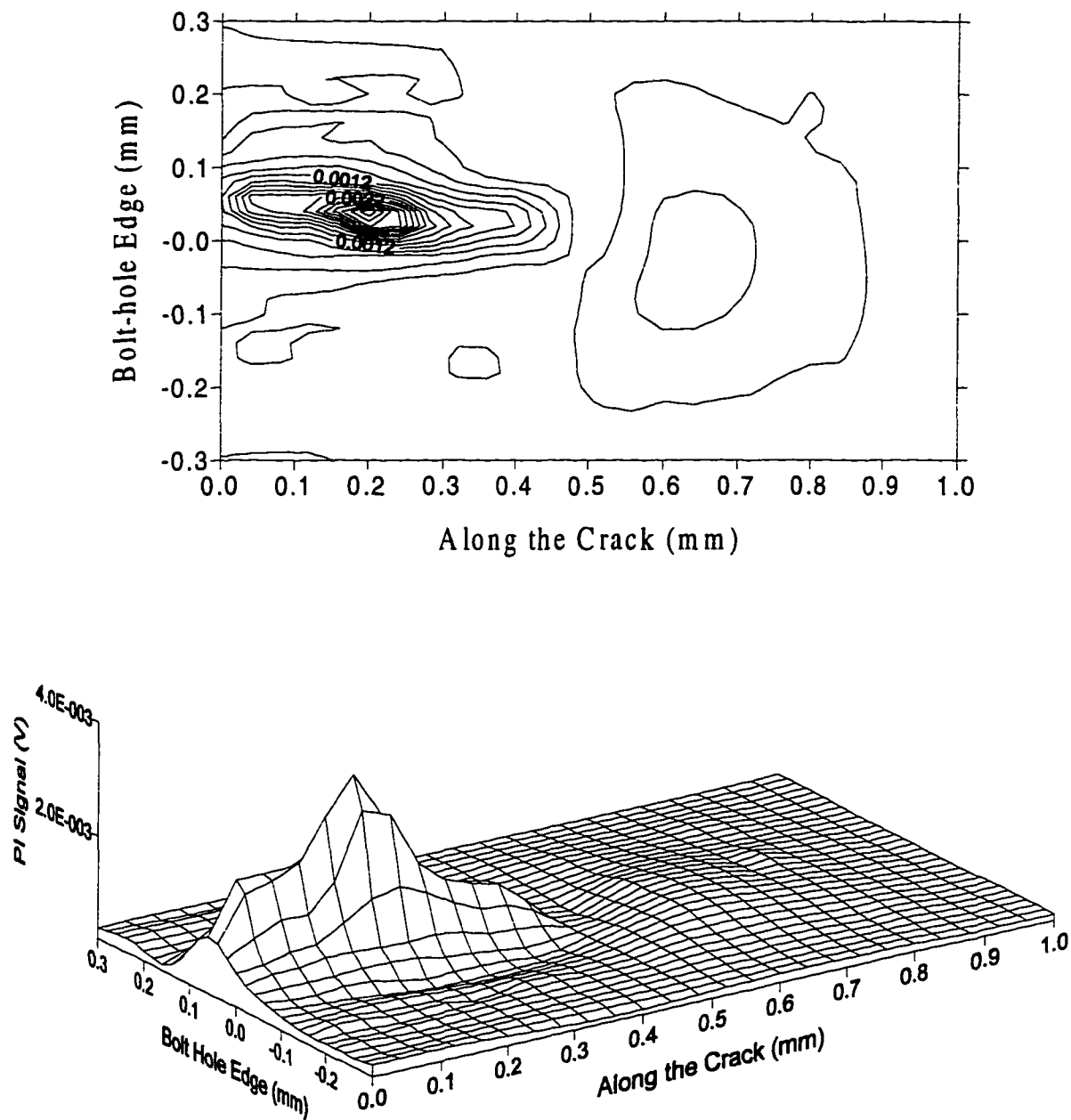
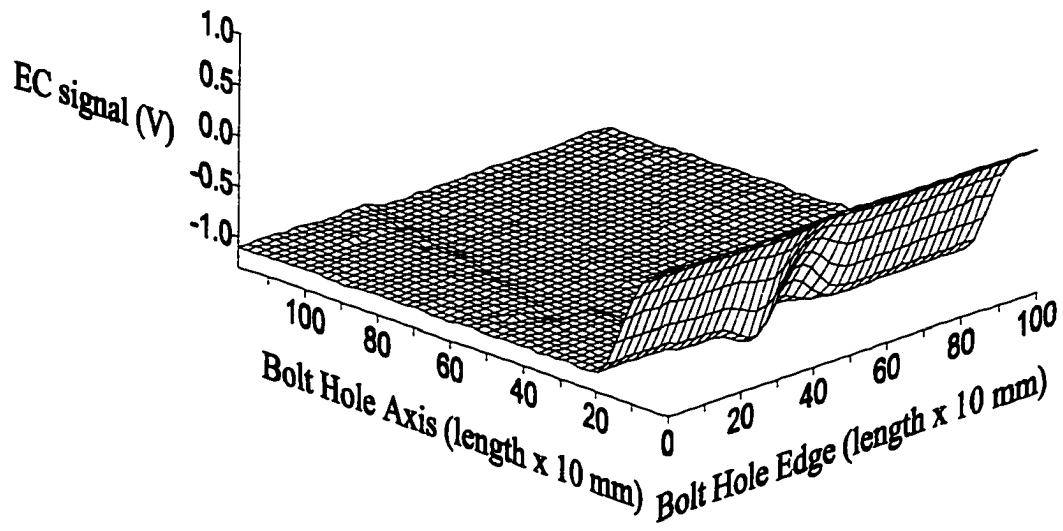
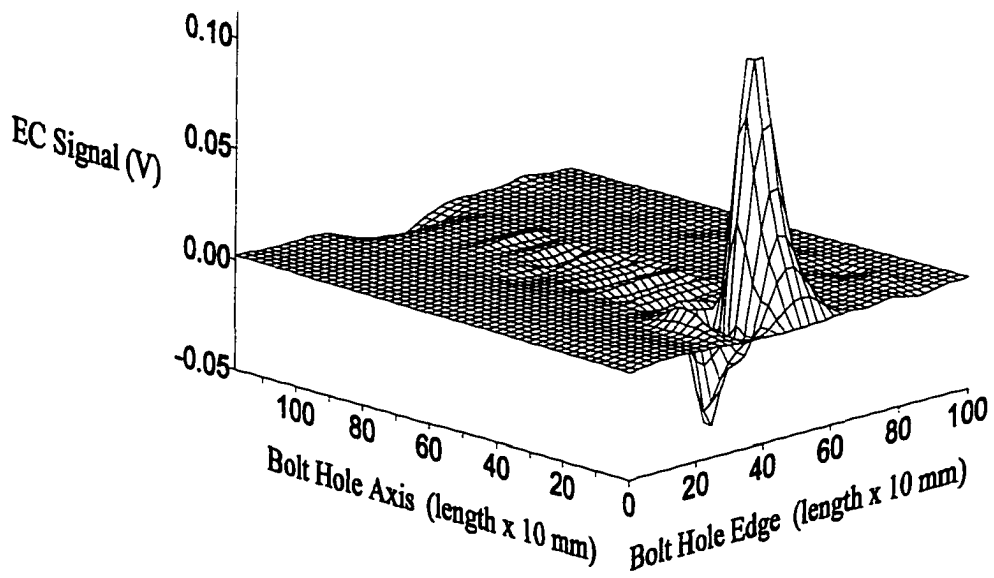


Figure 16. Shows the photoinductive contour and surface maps of another smaller real fatigue crack initiated from the bolt hole edge. (Crack length ≈ 0.5 mm; eddy-current frequency, 500 kHz; laser power, 0.4 W; chopping frequency, 40 Hz.)

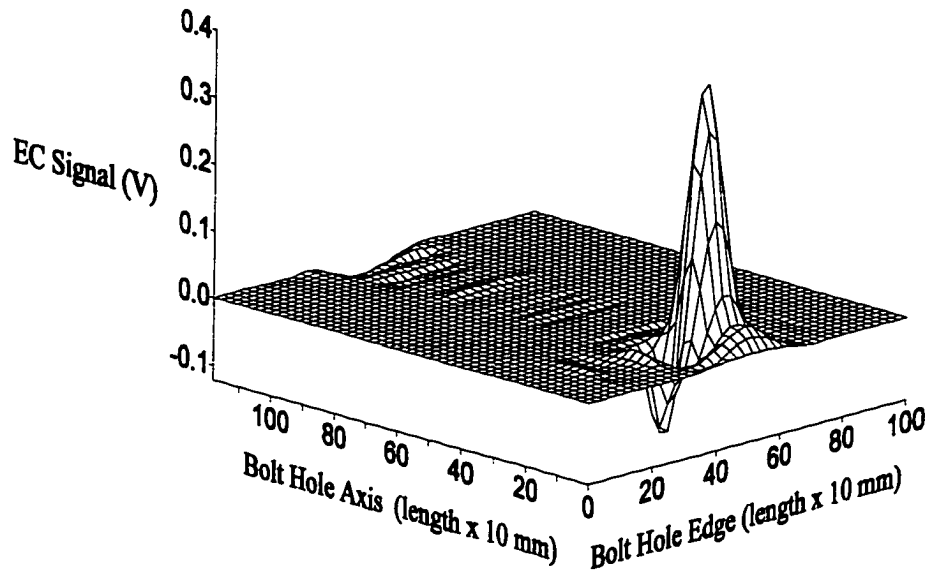


(a)

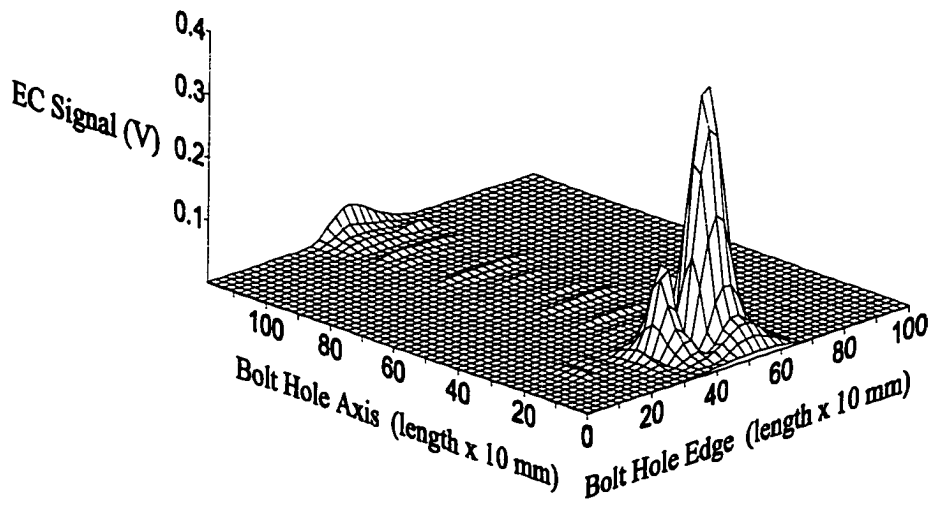


(b)

Figure 17. Eddy current imaging with rotating EC probe: (a) the imaginary component after smoothing; (b) & (c) are the real and imaginary components of the eddy current signals after background removal; (d) shows the magnitude of the impedance. (Rotational speed, 2 rpm; gain, 30 dB; EC frequency, 2 MHz.)



(c)



(d)

Figure 17. (Continued)

CHAPTER 6.

GENERAL CONCLUSIONS

The objectives of this dissertation were to devise and develop advanced eddy-current methods for quantitative NDE. The techniques used in this dissertation include the time-domain method (pulsed eddy current), the frequency-domain method (swept-frequency eddy current), and the photoinductive imaging method that combines eddy-current and laser-based thermal-wave techniques. We showed that the pulsed eddy current technique can be used to characterize metallic coatings on metal. A rapid inversion method was developed to determine the conductivity and thickness of the coating simultaneously. We developed theoretical models and practical measurement methods to characterize the coatings on a magnetic substrate and to characterize the properties of magnetic metals (surface condition). We have shown that the photoinductive imaging technique is a superior method for bolt hole corner crack inspection. We will briefly summarize the contributions of this dissertation and future plans in this chapter.

Based on the eddy-current techniques developed in Center for NDE, Iowa State University, four major objectives were achieved in this dissertation. First, we have successfully applied the pulsed eddy current method to measure the conductivity and thickness of metallic layers. A rapid inversion method that is based on building a lookup table was developed to determine both parameters simultaneously. This is an extension of the previous studies using the swept-frequency eddy current method. Since the pulsed eddy current technique is much quicker than the swept-frequency eddy current method, this

achievement forms a supplement to the application of eddy-current techniques to coating thickness and conductivity determinations.

The future work is to add the rapid inversion method that is developed in this dissertation to the software system of the pulsed eddy current instrument that was developed in the eddy current group. We developed a “Scanned Pulsed Eddy Current Instrument” that has been transferred to industry for commercial development. Since we have shown that the pulsed eddy current technique can be used to characterize metallic layers, the addition of an inversion method will give an instant estimation of the layer’s properties for coating characterization.

The second study concerned the fundamentals of eddy-current interaction with ferromagnetic metals such as nickel, iron, and steel. We have found that for elemental Ni, such measurements depends on a host of environmental factors. We found that mechanical polishing with 400 grit sandpaper causes the apparent permeability to drop by a factor of two or more. If, on the other hand, the surface of the sample is then etched away for 10–20 μm , the permeability increases by a factor of five. The sensitivity of the permeability to environmental factors is indicated by what happens after etching. If the sample is left in the air of the laboratory, the signal drops with time by up to a factor of three or four over a period of several weeks or months. We found that the change in the apparent permeability could be prevented by passivating the surface or by storing the sample in a vacuum. We have hypothesized that the change in permeability could be due to the infiltration of either oxygen or hydrogen into the near surface (10–100 μm) region of the metal.

Our most important result is the following hypothesis. The permeability of magnetically soft metals will depend very sensitively on a variety of extrinsic conditions. In these materials, it makes little sense to think of permeability as a material property. On the other hand, the permeability of hard magnetic metals such as steels will be much more stable and with appropriate care may be used for quantitative analysis. That is, we think that magnetic metals can be divided into two classes with very different behaviors for the apparent permeability. Our best hypothesis is that materials will divide into the two classes depending on whether they are magnetically soft or hard. On the other hand, we expect some differences to also occur due to the composition of the materials. For example, it may be that Ni based metals are much more sensitive to surface changes than iron based metals.

In the third study, we developed a measurement technique using either swept-frequency eddy current or transient eddy current methods for determining the thickness, conductivity, and permeability of metallic coatings on metal substrates for the case when either coating, metal, or both are ferromagnetic. This research extends the previous layer measurement method to the characterization of coatings on magnetic metals. One of the main reasons for undertaking the study of permeability anomalies in nickel was our desire to develop quantitative methods for characterizing surface layers and coatings on magnetic alloys, with a view to establishing methods for characterizing case hardening depth in steel. We have now taken a giant step in this direction by completing development of two methods for quantitatively determining the thickness and conductivity of metal coatings on ferromagnetic metals: swept-frequency and transient eddy current measurements. The coatings may be either ferromagnetic or non-magnetic. We have shown that, as long as the effective magnetic

permeability of coating and substrate are known or measured using the methods developed in studying the anomalous permeability of nickel, it is possible to model quantitatively the impedance of an air core probe placed near the surface in either the frequency or time domain. This gives us the means to determine thickness and conductivity of metals coatings on ferromagnetic metals.

The next step in the second and third studies is to develop practical measurement methods for characterizing the depth and hardness profile of case-hardened ferritic steels. Previous researchers, Uzal and Rose, have developed numerical methods for calculating the impedance of eddy current probes above layered metals whose conductivity and permeability vary continuously. Now, in our works we have a clearer understanding of the interaction between eddy currents and magnetic metals. We discovered unusual anomalies in the permeability of soft magnetic metals that prevented us from applying the same quantitative techniques to ferromagnetic metals. Now we have succeeded in understanding the anomalous behavior sufficiently well to permit us to apply the methods we have developed to magnetic metals. The methods include both swept-frequency eddy current measurements and transient (pulsed) eddy current measurements. We have demonstrated the ability to gauge the thickness of magnetic or nonmagnetic coatings on magnetic or nonmagnetic substrates. With the completion of this effort, we are now in a good position to tackle the more difficult problem of characterizing the depth of case hardening in practical steel alloys. Once we have completed development of quantitative eddy current techniques to characterize case-hardened surface layers on steel, we will be able to bring this long project to a successful conclusion. More work also needs to be done to understand the causes of the anomalous variations in

permeability that we have observed in commercially pure nickel and to determine which materials are susceptible to the observed phenomena.

The fourth study focused on a novel NDE method — the photoinductive imaging technique. This method combines eddy currents and laser-based thermal wave techniques. We have made significant progress in our study of photoinductive mapping of eddy current fields interacting with cracks. The goal of this work is to find new approaches to the difficult problem of detecting and characterizing cracks near or at the edge of bolt holes. Our approach is to insert a right cylindrical eddy current coil into the bolt hole and then to image the eddy currents flowing on the top surface around the hole. If a crack is present, we can visualize the deflected currents flowing around the crack and characterize its length from this pattern of current flow. We hope to make inroads on the problem of determining depth of such cracks as well. A titanium specimen with several bolt holes having corner EDM notches was examined, with very promising results. We have studied the effects of varying laser chopping frequency and eddy current frequency for a 0.75-mm deep triangular EDM slot in the corner of a 6-mm bolt hole in a Ti-6Al-4V plate. Excellent signal-to-noise ratios were obtained, and there are indications that the shape of the slot might be discernible, as well as the surface length. Further studies are continuing with EDM slots of differing depth, length, and shape. We also have examined corner fatigue cracks in similar specimens. The early results have been quite encouraging.

The future plans on this final study are to develop theoretical models and inversion methods and verify these theoretical predictions by developing practical measurement schemes. In the eddy current group, Norio Nakagawa has developed theoretical models to predict electric fields on the surface near surface breaking cracks interrogated with eddy

current probes. James H. Rose and his student, Ananth Sethuraman, have been using this forward model to aid in the development of practical inversion schemes to determine the depth of surface breaking cracks. And Cheng-Chi Tai and John Moulder have been developing practical measurement schemes to implement these proposed methods. The first results of our measurements on corner cracks at bolt holes are now available, and they look quite promising. The next step will be to develop new methods that will permit photoinductive measurements to be carried out on surface breaking cracks in a half-space geometry.

APPENDIX 1: SWEEP-FREQUENCY EDDY CURRENT SIGNAL AND PULSED EDDY CURRENT SIGNAL TRANSFORMATION

The key feature of the pulsed eddy current technique that makes it an attractive method is the wide bandwidth it provides [Fig. A1.1]. Conventional eddy current instruments operate at one or two frequencies at a time. Although the impedance analyzer offers a method to obtain data over a wide frequency range, the equipment is costly and bulky. The pulsed eddy current instrument offers the wide bandwidth of the impedance analyzer with the prospect for achieving this in a fast, portable instrument.

One of the original motives for the development of the PEC system is to find a method that can rapidly determine such properties as coating thickness and conductivity and, at the same time, retain the positive features of the frequency-domain approach. It can be shown that the pulsed eddy current signal contains the same information as the swept-frequency eddy current signal via transformation. We can transform the time-domain pulsed eddy current signal [Fig. A1.2] into the frequency-domain eddy current signal [Fig. A1.3] and vice versa.

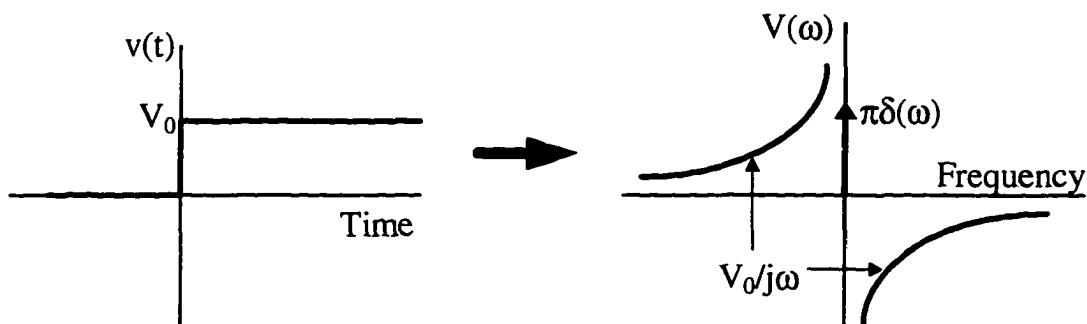


Figure A1.1. Step-function applied voltage and its frequency-domain form.

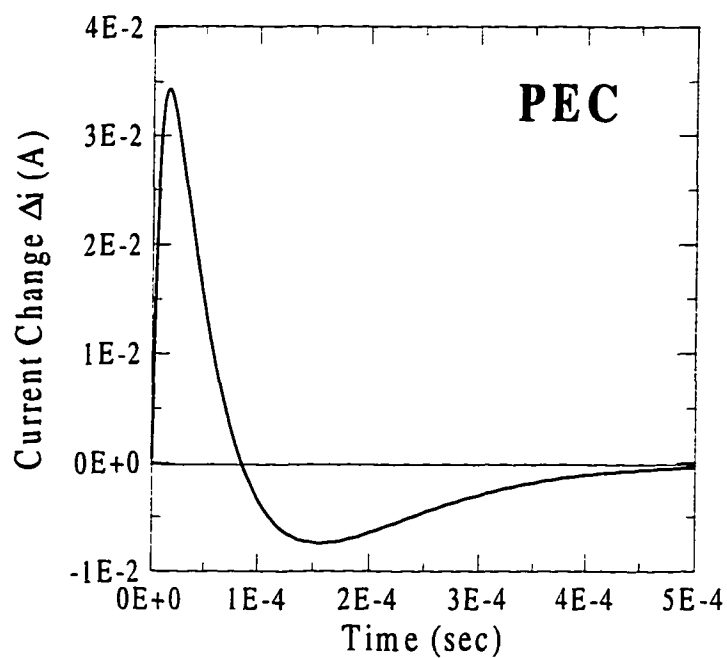


Figure A1.2. Time-domain eddy current signal using the pulsed eddy current instrument.

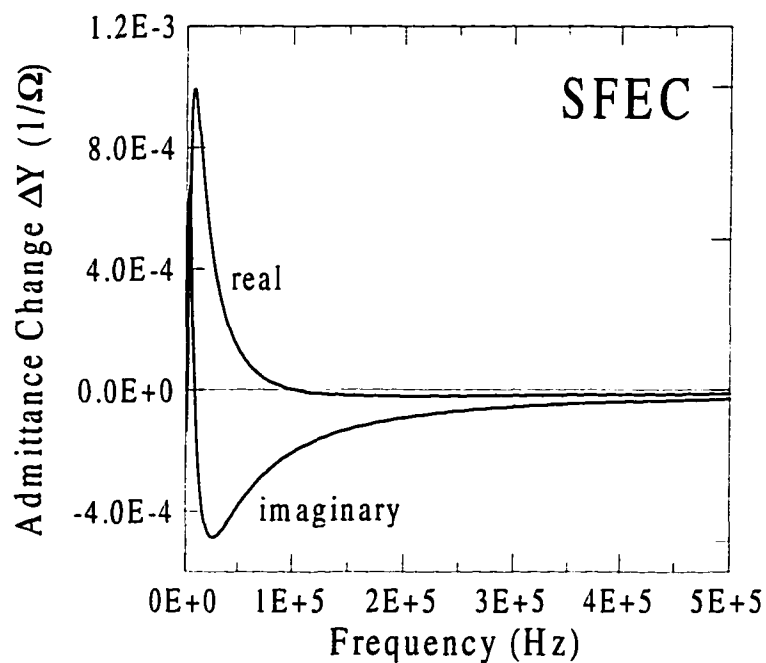


Figure A1.3. Frequency-domain eddy current signal using the HP 4194A impedance analyzer.

In Chapter 3, the transformation from frequency-domain eddy current signal to time-domain PEC signal has been illustrated. We first calculate the admittance difference, $\Delta Y(\omega)$, using the exact solutions of Dodd and Deeds [1]. The transient current, $\Delta i(t)$, due to a step-function applied voltage is obtained from the inverse Fourier transform of $\Delta I(\omega)$

$$\Delta i(t) = IFT(\Delta I(\omega)), \quad (\text{a1.1})$$

where

$$\Delta I(\omega) = \Delta Y(\omega)V(\omega). \quad (\text{a1.2})$$

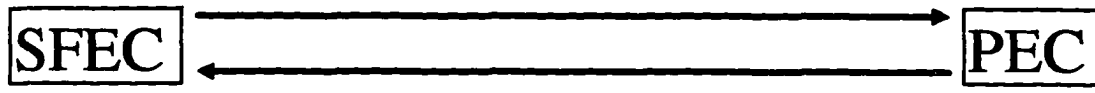
Here, $V(\omega)$ is the Fourier transform of the step-function applied voltage $v(t)$ [Fig. A1.1]. One then obtains

$$\Delta i(t) = \frac{1}{2\pi} \int_{-\infty}^{\infty} \frac{\Delta Y(\omega)}{i\omega} \exp(i\omega t) d\omega. \quad (\text{a1.3})$$

To obtain the swept-frequency eddy current signal from the pulsed eddy current signal, we can reverse the procedure above to get the frequency-domain signal,

$$\Delta Y(\omega) = i\omega \Delta I(\omega), \quad (\text{a1.4})$$

where $\Delta I(\omega)$ is the Fourier transform of the time-domain PEC signal, $\Delta i(t)$. We summarize the cycle of the time-frequency transforms in Fig. A1.4.

$$\Delta i(t) = IFT(\Delta I(\omega)) = \frac{1}{2\pi} \int_{-\infty}^{\infty} \frac{\Delta Y(\omega)}{i\omega} \exp(i\omega t) d\omega$$


$$\Delta Y(\omega) = i\omega \Delta I(\omega) = i\omega FT(\Delta i(t))$$

Figure A1.4. Transformation between swept-frequency eddy current signal (SFEC) and pulsed eddy current (PEC) signal.

Reference

- [1] C.V. Dodd and W. E. Deeds, "Analytical solutions to eddy-current probe-coil problems", *J. Appl. Phys.* 39, p. 2829 (1968).

APPENDIX 2: CORRECTIONS FOR NON-IDEAL COIL BEHAVIOR

The coils we used in this dissertation are specially wound air-cored coils [Table A2.1]. In order to compare the measured data with the theoretical solutions by Dodd and Deeds, only absolute coils were considered. As indicated in reference [1], the probable sources of error in the theoretical calculations are axial symmetry, the current sheet approximation and high-frequency effects. The high-frequency effects are probably the most serious source of error in the calculation technique. As the frequency increases, the current density ceases to be uniformly distributed over the cross section of the wire, but becomes concentrated near the surface. The resistance of the coil increases, and the inductance decreases. At high frequencies, the current is capacitively coupled between the turns in the coil, tending to flow across the loops of the wire, rather than through them. In practice, any real coil exhibits self-capacitance and resistance as well as additional capacitance associated with the leads. These deviations from ideal behavior must be taken into account if good agreement between theory and experiment is to be obtained over a significant frequency range.

Harrison et al.[2] suggested a correction method to correct the deviation from ideal coil behavior at high frequencies. They first correct the experimental data by eliminating the effects of stray capacitance and DC coil resistance. Second, they correct the deviations from ideal coil geometry (outer diameter and lift-off) by fitting the experimental impedance data to the well-established theoretical model of Dodd and Deeds for an air-cored coil above a conducting half-space.

Figure A2.1 shows the equivalent electrical circuit for a practical eddy-current probe coil, where R_0 and L_0 are the DC resistance and inductance of the coil respectively, Z_C is the reflected impedance due to eddy-current induction in any neighboring conductors, R_S and C_S represent the resistance and self-capacitance, and C_L represents the lead capacitance. Any other behavior is represented by the unspecified network RC . All these elements can be lumped together for convenience into a single parallel network Z_P . The presence of the parallel circuit Z_P results in deviations in coil impedance from the ideal value by an amount that increases with frequency and ultimately leads to coil resonance at a resonant frequency f_R . This resonant behavior is illustrated in Fig. A2.2.

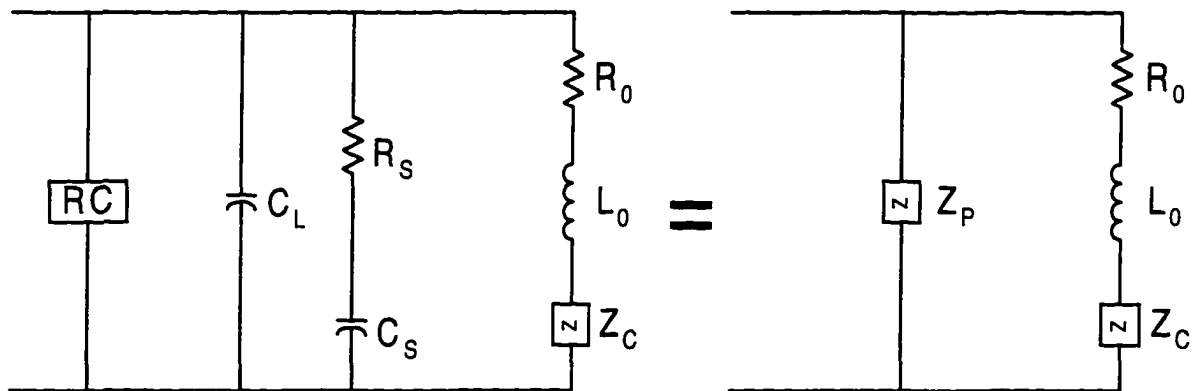


Figure A2.1. Equivalent electrical circuit for a practical eddy-current probe coil.

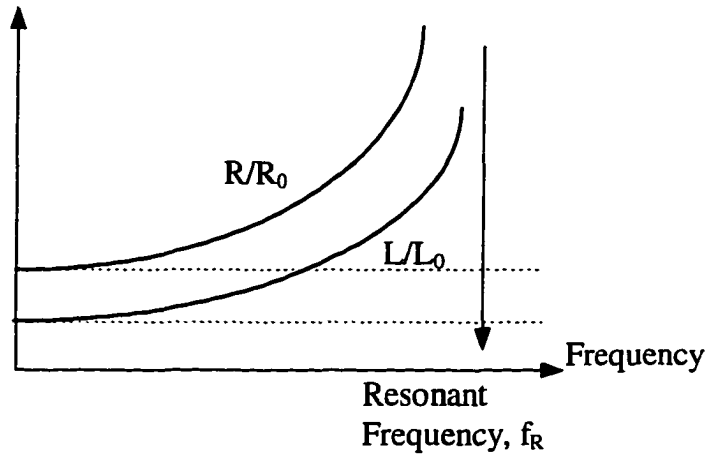


Figure A2.2. Coil inductance and resistance as a function of frequency. The deviations from the DC values at high-frequencies are due to the resonant behavior.

Correction Methods

Method 1:

The correction method used in this dissertation is similar to the method that was suggested by Harrison et al. [2] That is, by adjusting the coil parameters (outer diameter and lift-off) until experimental and theoretical values agree. These corrected coil parameters have been used in most studies in the eddy current group up to now. Usually, the disagreement is less than 3%.

The method that Harrison et al. used is to minimize the RMS error, ϵ , between the experimental impedance and the theoretical calculation of Dodd & Deeds over the frequency range from 200 Hz to 1 MHz (Eq. A2.1).

$$\epsilon^2 = \frac{1}{N} \sum_{i=1}^N \left\{ \frac{[\Delta R_{EXP}(i) - \Delta R_{D\&D}(i)]^2}{[\Delta R_{EXP}(i)]^2} + \frac{[\Delta L_{EXP}(i) - \Delta L_{D\&D}(i)]^2}{[\Delta L_{EXP}(i)]^2} \right\} \quad (A2.1)$$

The disadvantage of this method is that the resonant behavior can not be totally removed in this way. Our practical experience shows that there is a difference of about 0.5Ω between the measured data and theoretical calculations in the swept-frequency eddy current signal for frequencies up to two megahertz. This difference is not very important when our interest is in the lower frequency part. But it is crucial when we want to investigate the relation of coil impedance and frequency-dependent material properties — such as permeability.

Method 2:

The second method suggested by Harrison et al. is to remove the effects of the parallel circuit. They correct the impedance data for the coil above an unflawed region, the coil above a half-space with a defect, and the impedance difference between two areas. We can apply the same scheme to our experiments on coatings characterization and hidden corrosion inspection. The impedance data are corrected in the following way. The coil impedance Z_A is measured in air over the selected frequency range and the DC values of resistance and inductance, R_0 and L_0 , are determined from the low frequency limit and used to calculate the ideal admittance,

$$Y_0(\omega) = 1/Z_0(\omega) = 1/(R_0 + j\omega L_0). \quad (\text{A2.2})$$

This is subtracted from the admittance in air

$$Y_A(\omega) = 1/Z_A(\omega), \quad (\text{A2.3})$$

to give the admittance of the equivalent parallel network

$$Y_P(\omega) = Y_A(\omega) - Y_0(\omega). \quad (\text{A2.4})$$

In order to correct the measured impedance Z_U obtained with the coil on an unflawed region of the test specimen (layer-free half-space or no corrosion area, in our case), the admittance of the parallel circuit is subtracted from the admittance Y_U to give the corrected impedance

$$Z_{corr}^U = \frac{1}{Y_U - Y_P}. \quad (\text{A2.5})$$

Hence, the corrected impedance change due to the unflawed test-specimen is

$$\Delta Z_{corr}^U = Z_{corr}^U - Z_0. \quad (\text{a2.6})$$

The corrected impedance change due to the presence of a defect in the half-space (layered half-space or an area with corrosion, in our case) can then be written in the form

$$\Delta Z_{corr}^D = \frac{1}{Y_D - Y_P} - \frac{1}{Y_U - Y_P}, \quad (\text{A2.6})$$

where Y_D is the admittance measured in the presence of the defect. The effects of the parallel network can be eliminated by this process.

The following are some examples that show the data corrected using the methods described above. Figure A2.3 shows the corrected and uncorrected impedance difference for a coil above a half-space of stainless steel and a coil in air, and the theoretical calculations using the exact solution of Dodd and Deeds [1]. The probe is the L-probe that was used in most of the work. Figure A2.4 shows the corrected and uncorrected impedance differences for a coil above a layered half-space and a coil above a half-space. Usually, the corrected data agree much better with the theoretical calculation. Nevertheless, as shown in Fig. A2.4(a), the impedance difference was over-corrected. This indicates that the previous correction method (method-1) of adjusting the coil parameters may not correctly size the coil. We expect much better results after precisely correcting the coil parameters and eliminating the high-frequency effects. Finally, we show a figure (Fig. A2.5) that compares the corrected and uncorrected measured data for a coil above a magnetic metal (nickel). They have same features as in the nonmagnetic metal cases, the high-frequency effects increase the error with increasing frequency. The error is almost negligible at low frequency, but has a significant effect at high frequency. Our further work [3,4], will account for the high-frequency effects using the correction method described in this appendix.

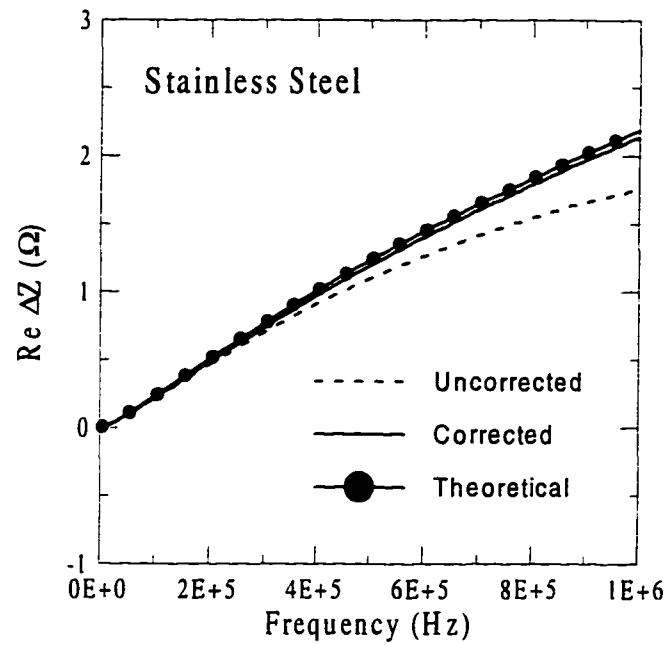


Figure A2.3(a). Real part of the impedance difference for coil above stainless steel half-space.

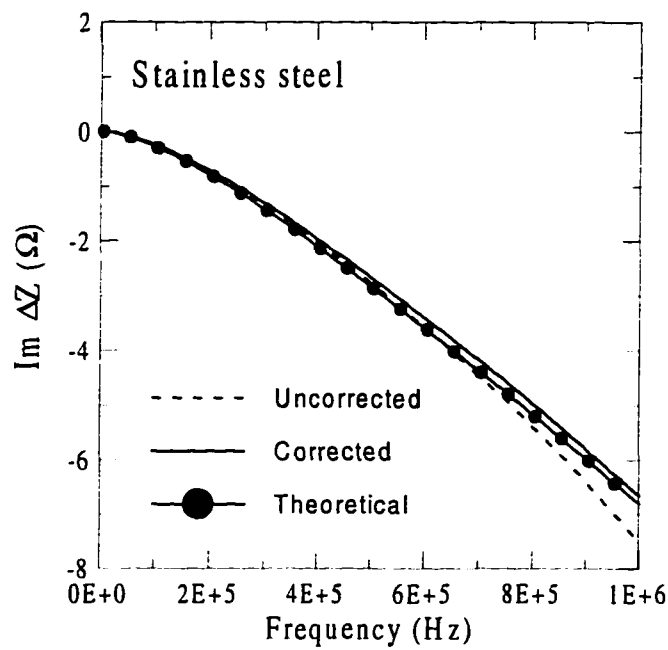


Figure A2.3(b). Imaginary part of the impedance difference for coil above stainless steel half-space.

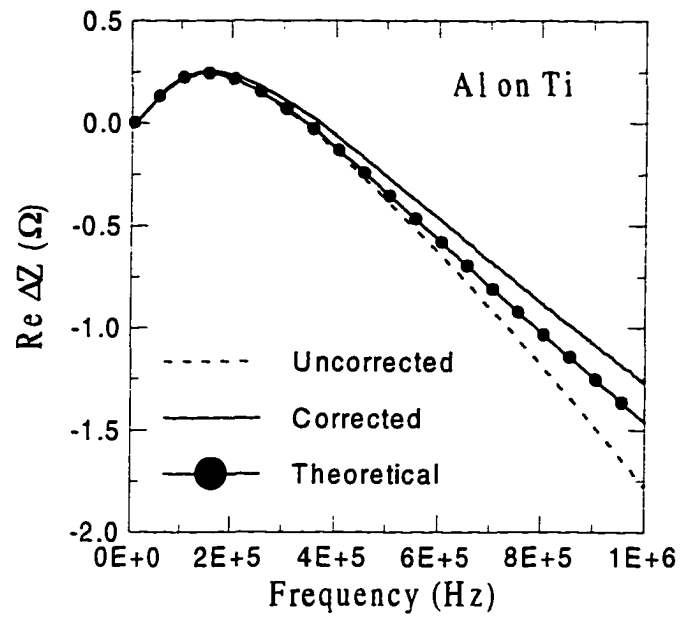


Figure A2.4(a). Real part of the impedance difference for coil above layered half-space (aluminum coated on titanium).

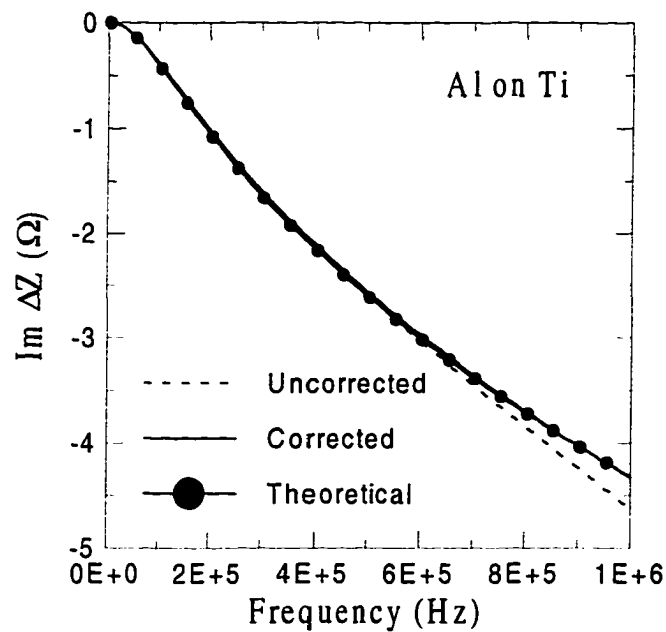


Figure A2.4(b). Imaginary part of the impedance difference for coil above layered half-space (aluminum coated on titanium).

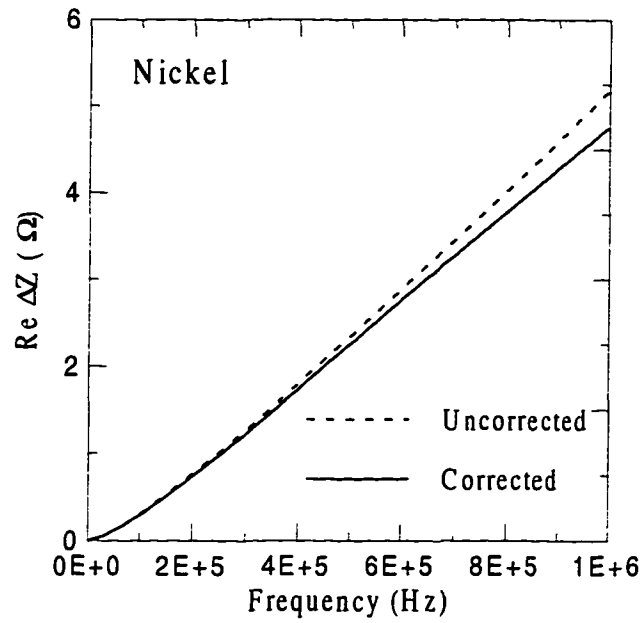


Figure A2.5(a). Real part of the impedance difference for coil above a magnetic metal (nickel).

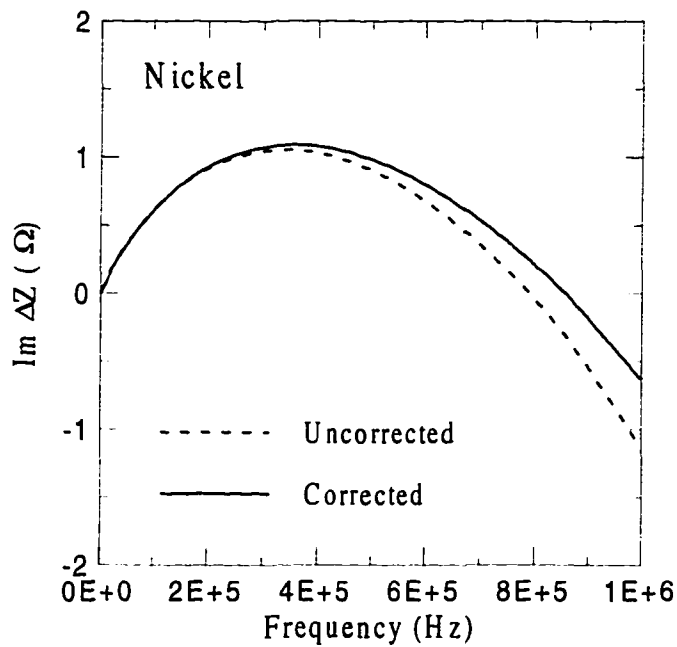


Figure A2.5(b). Imaginary part of the impedance difference for coil above a magnetic metal (nickel).

Table A2.1. The geometry and electrical properties of the coils used in this dissertation.

Probe	A	L	X	PI24
Number of turns, N	504	235	638	50
Inner radius, r_1	3.8 mm	0.535 mm	2.75 mm	1.524 mm
Outer radius, r_2	5.635 mm	1.31 mm	5.64 mm	3.048 mm
Height, $l_2 - l_1$	2.42 mm	2.93 mm	2.65 mm	0.762 mm
Lift-off, l_1	0.125 mm	0.62 mm	0.33 mm	0.485 mm
Resistance @ 1k Hz, R_0	56.7 Ω	5.82 Ω	49.3 Ω	1.94 Ω
Inductance @ 1k Hz, L_0	2.56 mH	38.0 μ H	2.92 mH	13.23 μ H
Resonant frequency, f_R	1.1 MHz	4.26 MHz	640 kHz	13.35 MHz

References

- [1] C.V. Dodd, and W. E. Deeds, "Analytical solutions to eddy-current probe-coil problems", *J. Appl. Phys.* 39, p. 2829 (1968).
- [2] D. J. Harrison, L. D. Jones, and S. K. Burke, "Benchmark Problems for Defect Size and Shape Determination in Eddy-Current Nondestructive Evaluation", in *J. Nondestruct. Eval.* Vol. 15, No. 1, p. 21 (1996).
- [3] J. H. Rose, C.-C. Tai, and J. C. Moulder, "Scaling Relation for the Inductance of a Coil on a Ferromagnetic Half-Space", will be submitted to *J. Appl. Phys.* (1997).
- [4] J. C. Moulder, C.-C. Tai, B. Larson, and J. H. Rose, "Inductance of a Coil on a Thick Ferromagnetic Metal Plate", will be submitted to *IEEE Trans. on Magnetics* (1997).

APPENDIX 3: SOFTWARE DESIGN AND IMPLEMENTATION

The program we used for most of the calculations in this dissertation is listed here. This program uses the solution of Dodd and Deeds, but in an alternative form as shown in Chapter 4. It can be used to calculate the coil impedance for a coil in air, a coil above single-layered half-space or layer-free half-space, as well as the impedance difference between two areas. It also calculate the current difference for pulsed eddy current applications. The materials can be magnetic or nonmagnetic. It was coded using a state-of-the-art computer language — C++. This program must be run by using command-line arguments. A Windows™ version of the same program is under development. We will combine this program with control software for the “Scanned Pulsed Eddy Current Instrument” that is being developed in the eddy current group at the Center for NDE.

```
//=====
//=====
#include <stdio.h>
#include <stdlib.h>
#include <iostream.h>
#include <Complex.h>

#define PI (3.14159265358979)
#define mu (PI*(4e-7)) // Permeability for free space:  $\mu_0$  (H/m)

//===== CLASS: mgmath =====
class mgmath {
public:
    Complex intg(int, Complex *, Complex);
    double bessj1(double);
};

//===== integration =====
Complex mgmath::intg(int n, Complex *f, Complex h)
```

```

{
    Complex sum = f[0]+f[2*n]+4*f[1];
    for(int j=2; j<=n; j++) sum += (4*f[2*j-1] + 2*f[2*j-2]);
    return sum*=(h/3);
}

//===== bessj1.c =====
double mgmath::bessj1(double x)
{
    // Insert the first-order Bessel function here.
}

//===== MAIN PROGRAM =====
int main(int argc, char **argv)
{
    mgmath MATHS;
    int    i, j, pn;
    int    N;           // Number of turns
    int    NOMG;        // Points of frequency / 2

    double r1, r2, rb;  // Inner and outer radii of the coil, rb=(r1+r2)/2
    double l1, L, l2;   // Lift-off, Coil height, l2=l1+L

    double u1, u2;     // Relative permeability of the layer and the Substrate
    double s1, s2;     // Conductivity of the layer and the Substrate
    double c;          // Thickness of the layer

    double w, fstop;   // Omag, stop frequency
    double DOMG;       // Frequency step
    double *OM;        // Radian frequency
    double t, dt, tstop; // Time step, stop time

    double v;          // Amplitude of the step-function voltage
    double amp;        // Amplifier
    double res;        // DC resistance of coil

    Complex a1, a2, b1, b2, b3, A, K, H, xi;

    int    zmax, nz;
    Complex sz, dr;    // For integration, sz=zmax/(2.*nz)

    Complex *a, *I, *x, *g;
    Complex *fz1, *fz2, *fz3;
    Complex Z1, Z2, Z3; // Impedance in Air, on half-space, and on layered HSP
}

```

```

Complex DZ1, DZ2, DZ3;           // ΔZs in frequency domain

Complex *GD1, *G1, *GD2, *G2, *GD3, *G3, *DY, *Y;
Complex di1, di2, di3, dy;      // Δi1(t), Δi2(t), Δi3(t), Δy(t)

FILE *fp1=fopen(argv[1],"w"),    // To save the parameters
    *fp2=fopen(argv[2],"w"),    // Δi1(t)=i2-i1, ex: Ni - Air
    *fp3=fopen(argv[3],"w"),    // Δi2(t)=i3-i2, ex: CuNi - Ni
    *fp4=fopen(argv[4],"w"),    // Δi3(t)=i3-i1, ex: CuNi - Air
    *fp5=fopen(argv[5],"w"),    // Δy(t) : Δy, ex: CuNi - Ni
    *fp6=fopen(argv[6],"w"),    // ΔY(ω) : ΔY, ex: CuNi - Ni
    *fp7=fopen(argv[7],"w"),    // Z1(ω) : coil in air
    *fp8=fopen(argv[8],"w"),    // Z2(ω) : coil above half-space
    *fp9=fopen(argv[9],"w"),    // Z3(ω) : coil above layered half-space
    *fp10=fopen(argv[10],"w"),  // ΔZ1=Z2-Z1 in freq domain, ex: Ni - Air
    *fp11=fopen(argv[11],"w"),  // ΔZ2=Z3-Z2 in freq domain, ex: CuNi - Ni
    *fp12=fopen(argv[12],"w");  // ΔZ3=Z3-Z1 in freq domain, ex: CuNi - Air

if (argc<2)
{
    cout << "\nThis program must be run by using command-line arguments";
    cout << "\n\nPlease see the batch file for the detail (mg7l.bat)\n\n";
    exit(1);
}

pn = 12;                          // No. of arguments before r1
r1 = atof(argv[pn+1]);            // Inner radius of the coil
r2 = atof(argv[pn+2]);            // Outer radius of the coil
l1 = atof(argv[pn+3]);            // Lift-off (mm)
L = atof(argv[pn+4]);             // Coil height
N = atoi(argv[pn+5]);             // No. of turns
res = atof(argv[pn+6]);           // Resistance of coil
v = atof(argv[pn+7]);             // Voltage of the step-function
amp = atof(argv[pn+8]);           // Amplifier

NOMG = atoi(argv[pn+9]);          // Half of frequency points
fstop= atof(argv[pn+10]);         // Stop frequency

dt = atof(argv[pn+11]);           // Time step
tstop= atof(argv[pn+12]);         // Stop time

s1 = atof(argv[pn+13]);           // Conductivity of the layer
s2 = atof(argv[pn+14]);           // Conductivity of the substrate

```

```

c = atof(argv[pn+15]); // Thickness of the layer (mm)
u1 = atof(argv[pn+16]); // Relative permeability of the layer
u2 = atof(argv[pn+17]); // Relative permeability of the substrate

c/=1000;
DOMG=2*PI*fstop/(2*NOMG); // Radian frequency step
r1/=1000; r2/=1000;
rb=(r1+r2)/2; // millimeter ==> meter
l1/=1000; L/=1000; l2=l1+L;

zmax=40; // For integration range : 0 - zmax
nz=400; // Integration points
sz=zmax/(2.*nz);

//*****
r1/=rb; // Normalized inner radius
r2/=rb; // Normalized outer radius
l1/=rb; // Normalized lift-off
l2/=rb; // Normalized coil height+lift-off
L /=rb; // Normalized coil height
c /=rb; // Normalized thickness of layer

a = new Complex[nz*2+1]; // Dynamic array allocation: a keep feature of C++
x = new Complex[zmax+1];
g = new Complex[zmax+1];
I = new Complex[nz*2+1];

fz1 = new Complex[nz*2+1];
fz2 = new Complex[nz*2+1];
fz3 = new Complex[nz*2+1];

OM = new double[2*NOMG+1];

GD1 = new Complex[2*NOMG+1];
G1 = new Complex[2*NOMG+1]; // for di1(t), ex: Ni - Air (HSP - Air)
GD2 = new Complex[2*NOMG+1];
G2 = new Complex[2*NOMG+1]; // for di2(t), ex: CuNi - Ni
GD3 = new Complex[2*NOMG+1];
G3 = new Complex[2*NOMG+1]; // for di3(t), ex: CuNi - Air

DY = new Complex[2*NOMG+1];
Y = new Complex[2*NOMG+1]; // for dy(t), ex: CuNi - Ni

//===== I(a,r1,r2) =====

```

```

for(j=1; j<=2*nz; j++)
{
  a[j] = j*sz;
  dr = (a[j]*(r2-r1))/zmax;
  for(i=0; i<=zmax; i++)
  {
    x[i] = (a[j]*r1)+(i*dr);
    g[i] = x[i] * MATHS.bessj1(real(x[i]));
  }
  I[j] = MATHS.intg(zmax/2,g,dr);
}

```

```

//===== head of the files =====
fprintf(fp2, "\tTime      di1(t)      -di1(t)\n");
fprintf(fp3, "\tTime      di2(t)      -di2(t)\n");
fprintf(fp4, "\tTime      di3(t)\n");
fprintf(fp5, "\tTime      dy(t)\n");
fprintf(fp6, "\tFreq      real      imag\n");
fprintf(fp7, "\tFreq      real      imag\n");
fprintf(fp8, "\tFreq      real      imag\n");
fprintf(fp9, "\tFreq      real      imag\n");
fprintf(fp10, "\tFreq      real      imag\n");
fprintf(fp11, "\tFreq      real      imag\n");
fprintf(fp12, "\tFreq      real      imag\n");

```

```

//=====Z1(ω), Z2(ω), Z3(ω), GD(ω), DY(ω) =====
for(i=1; i<=2*NOMG; I++) // for 2*NOMG different frequencies.
{
  w = OM[i] = i*DOMG; // Radian frequency of the current
  for(j=1; j<=2*nz; j++) // for each frequency
  {
    a[j]=j*sz; // α
    a1=sqrt(Complex( real(a[j]*a[j]), w*mu*u1*s1*rb*rb)); // α1
    a2=sqrt(Complex( real(a[j]*a[j]), w*mu*u2*s2*rb*rb)); // α2
    A=exp(-2*a[j]*l1) + exp(-2*a[j]*l2) - 2*exp(-a[j]*(l1+l2)); // A(α)
    b1=2*a[j]*u1 * ((a2*u1-a1*u2)-(a2*u1+a1*u2)*exp(2*a1*c));
    b2=(a1-a[j]*u1)*(a1*u2-a2*u1)-(a1+a[j]*u1)*(a2*u1+a1*u2)*exp(2*a1*c);

    // Z1 : coil in air
    fz1[j]=(1/pow(a[j],5)) * I[j]*I[j] *(2*L+ (1/a[j])*(2*exp(-a[j]*L) - 2 ));

    // Z2 : coil above half-space
    fz2[j]=(1/pow(a[j],5)) * I[j]*I[j]
      *(2*L+ (1/a[j])*(2*exp(-a[j]*L) - 2 +A*((a[j]*u2-a2)/(a[j]*u2+a2))));
  }
}

```

```

// Z3 : coil above layered half-space
fz3[j]=(1/pow(a[j],5)) * I[j]*I[j]
        *(2*L+ (1/a[j])*(2*exp(-a[j]*L) - 2 +A*(b1/b2-1)));
} //end of loop j

fz1[0] = fz2[0] = fz3[0] = 0;
H=(PI*N*N*w*mu*Complex(0,1)*rb)/(L*L*(r2-r1)*(r2-r1));

Z1 = H * MATHS.intg(nz,fz1,sz); // impedance in air
Z2 = H * MATHS.intg(nz,fz2,sz); // impedance on half-space
Z3 = H * MATHS.intg(nz,fz3,sz); // impedance on layered half-space
Z1 += res; // Note : add DC resistance of the coil
Z2 += res;
Z3 += res;

DY[i]=1/Z3 - 1/Z2; // ΔY(ω): admittance difference
fprintf(fp6,"%14.4Lf %18.8e %18.8e\n",w/(2*PI),real(DY[i]),imag(DY[i]));
fprintf(fp7,"%14.4Lf %18.8e %18.8e\n",w/(2*PI),real(Z1), imag(Z1));
fprintf(fp8,"%14.4Lf %18.8e %18.8e\n",w/(2*PI),real(Z2), imag(Z2) );
fprintf(fp9,"%14.4Lf %18.8e %18.8e\n",w/(2*PI),real(Z3), imag(Z3) );

DZ1=Z2-Z1; // ex: Ni - Air
DZ2=Z3-Z2; // ex: CuNi - Ni
DZ3=Z3-Z1; // ex: CuNi - Air
fprintf(fp10,"%14.4Lf %18.8e %18.8e\n",w/(2*PI),real(DZ1),imag(DZ1) );
fprintf(fp11,"%14.4Lf %18.8e %18.8e\n",w/(2*PI),real(DZ2),imag(DZ2) );
fprintf(fp12,"%14.4Lf %18.8e %18.8e\n",w/(2*PI),real(DZ3),imag(DZ3) );

GD1[i]=((Z1-Z2)/(Z1*Z2))*v; // ΔI1(ω)
GD2[i]=((Z2-Z3)/(Z2*Z3))*v; // ΔI2(ω)
GD3[i]=((Z1-Z3)/(Z1*Z3))*v; // ΔI3(ω)

} // end of loop i

//***** di(t), dy(t) : IFT *****
t=0;
do{
for(i=1; i<=2*NOMG; i++)
{
G1[i] = ( real(GD1[i]) * sin(OM[i]*t)
+ imag(GD1[i]) * cos(OM[i]*t) )/OM[i]; // for di1(t)
G2[i] = ( real(GD2[i]) * sin(OM[i]*t)
+ imag(GD2[i]) * cos(OM[i]*t) )/OM[i]; // for di2(t)
}
}

```

```

G3[i] = ( real(GD3[i]) * sin(OM[i]*t)
        + imag(GD3[i]) * cos(OM[i]*t) )/OM[i];    // for di3(t)
Y[i]   = ( real(DY[i]) * sin(OM[i]*t)
        + imag(DY[i]) * cos(OM[i]*t) )/OM[i];    // for dy(t)
}

G1[0] = G2[0] = G3[0] = Y[0] = 0;

di1= -amp * MATHS.intg(NOMG, G1, DOMG) / PI;      // di1(t)
di2= -amp * MATHS.intg(NOMG, G2, DOMG) / PI;      // di2(t)
di3= -amp * MATHS.intg(NOMG, G3, DOMG) / PI;      // di3(t)
dy = -amp * MATHS.intg(NOMG, Y,  DOMG) / PI;      // dy(t)

fprintf(fp2,"%14.4E %18.8E %18.8E\n",t,real(di1),-real(di1));
fprintf(fp3,"%14.4E %18.8E %18.8E\n",t,real(di2),-real(di2));
fprintf(fp4,"%14.4E %18.8E\n",t,real(di3));
fprintf(fp5,"%14.4E %18.8E\n",t,real(dy));

} while ((t+=dt)<tstop);

fclose(fp2);   fclose(fp3);   fclose(fp4);   fclose(fp5);
fclose(fp6);   fclose(fp7);   fclose(fp8);   fclose(fp9);   fclose(fp10);
fclose(fp11);  fclose(fp12);

delete [] a, x, g, l, fz1, fz2, fz3, Z1, OM, GD1,GD2,GD3, DY, G1,G2,G3,Y;
}

```

ACKNOWLEDGEMENTS

I would like to thank my research advisor, Mr. John C. Moulder, for his guidance and encouragement throughout my graduate program. I would also like to thank the NSF Industry/University Center for NDE at Iowa State University for the funding they provided throughout my program.

I would like to thank Dr. James H. Rose for many helpful instructions and discussions concerning this work.

I also wish to thank my major professor, Dr. Hsiu C. Han, for his help and advice throughout this program. I would also like to thank my committee members, Dr. Lalita Udpa, Dr. Vasant G. Honavar, and Dr. John P. Basart for their valuable time.

Finally, I would sincerely like to thank my family. My wife, Tsui-Ling Lu, has always supported and encouraged me to continue my education. My parents, parent in-laws, sister, sister in law, brother, and brother in-law have seen us through the hard times, helping us when we needed help. I owe all of these people a great deal.